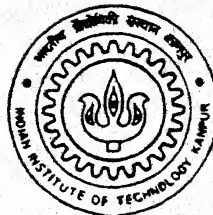


9520610

INFLUENCE OF GROWTH RATE CHANGES ON PRIMARY DENDRITE SPACING AND SOLUTE REDISTRIBUTION IN Sn-Bi ALLOYS

By
P. Syamala



DEPARTMENT OF MATERIALS AND METALLURGICAL ENGINEERING
INDIAN INSTITUTE OF TECHNOLOGY, KANPUR

DECEMBER, 1998

TH
MME/1998/M
Sj/3.2

INFLUENCE OF GROWTH RATE CHANGES ON PRIMARY DENDRITE SPACING AND SOLUTE REDISTRIBUTION IN Sn-Bi ALLOYS

**A Thesis Submitted
in Partial Fulfillment of the Requirements
for the Degree of**

MASTER OF TECHNOLOGY

by

P. Syamala



to the

**DEPARTMENT OF MATERIALS AND METALLURGICAL
ENGINEERING**

**INDIAN INSTITUTE OF TECHNOLOGY
KANPUR**

December, 1998

26 MAR 1999/MME

CENTRAL LIBRARY
I. I. T., KANPUR

~~Acc. No.~~ **A 127799**

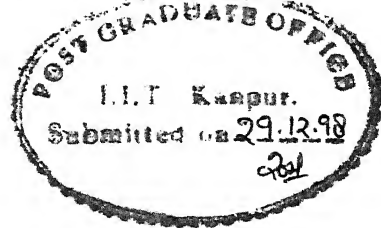
TH

MME/1998/M

Sy 13 i



A127799



CERTIFICATE

It is certified that the work contained in the thesis entitled "Influence of Growth Rate Changes on Primary Dendrite Spacing and Solute Redistribution in Sn-Bi Alloys" by "P. Syamala" has been carried out under my supervision and that it has not been submitted elsewhere for a degree.

A handwritten signature in black ink, appearing to read "V. Bansal".

(Dr. V. Bansal)

Professor

Department of Metallurgical Engineering

Indian Institute of Technology

Kanpur 208016

Date: December, 1998

TO

MY PARENTS

&

MY HUSBAND

Abstract

This work deals with directional solidification of Sn-Bi alloys for the dendrite arm spacing measurements and solute redistribution. The alloy compositions have been chosen as 2 and 4wt% Bi. Directional solidification was carried out by moving the furnace upwards relative to the quartz/pyrex crucible containing the alloy which is held stationary. The furnace was made to move at four different freezing rates ranging from 31 to 284 $\mu\text{m/s}$. The temperature gradient was maintained at 7.8°C/mm for 4wt% Bi and 8.4 °C/mm for 2wt% Bi alloy. Temperatures at different points below the equilibrium solid/liquid interface was measured. The primary dendrite spacing (λ) is found to vary with freezing rate (R), as $\lambda \propto R^{-0.314}$ in case of 2wt% Bi alloy and $\lambda \propto R^{-0.33}$ in case of 4wt% Bi alloy. The heat transfer coefficient for water being sprayed over a vycor tube containing the hot alloy is experimentally found as 0.1314×10^4 watts/m²/k. The solute redistribution measured in a direction approximately normal to the direction of dendrite growth is found to match with the theoretically predicted values.

Acknowledgement

I feel pleasure in expressing my most sincere gratitude to Dr. V. Bansal for his valuable guidance and constant encouragement throughout the course of this work. His ever helping attitude and encouraging remarks made me feel at home at IIT Kanpur. The memories working with him will be cherished all along my life.

I also express my hearty gratitude to Mr. V.P. Gupta, Draftsman and Mr. Saini, Typist. It is indeed a matter of great pleasure to acknowledge Jaswant, Giridhar, Madhu and Meymol who helped.

P. Syamala

Table of Contents

Certificate	i
Abstract	ii
Acknowledgement	iii
Table of Contents	iv
List of Tables	vi
List of Figures	vii
Chapter 1 Introduction	1
Chapter 2 Literature Survey	4
2.1 Thermal Analysis of Bridgman Apparatus	5
2.2 Movement of Solid/Liquid Interface	6
2.3 Free and Constrained Dendritic Growth	7
2.4 Primary Dendrite Arm Spacing	8
2.5 Solute Redistribution	12
2.6 Empirical Relation for Heat Transfer Coefficient	13
Chapter 3 Experimental Procedure	15
3.1 Master Alloy Preparation	15
3.1.1 Gas Purification Train	17
3.1.2 Vacuum Pump	19
3.1.3 Rocking Furnace	19
3.2 Specimen Capsule	19
3.3 Master Alloy Making	21
3.4 Directional Solidification Apparatus	22
3.4.1 Drive Mechanism	24
3.4.2 Furnace and its Motion	24
3.4.3 The Crucible Stand	25
3.4.4 Chill Assembly and Chill Cap	25
3.5 Steps for Making a Directional Solidification Run	26
3.5.1 Assembling the Apparatus for a Run	27
3.5.2 Measuring Steady State Temperature along the Length of the Furnace	28
3.5.3 Measuring Temperature Profiles inside and outside the Crucible	28
3.5.4 Determination of Position of Solid/Liquid Interface	34
3.5.5 Determination of Temperature at Different Points below the Equilibrium Solid/Liquid Interface	34
3.5.6 Directional Solidification Runs	38
3.6 Specimen Preparation and Observations	40
3.6.1 Slicing of the Ingot	40
3.6.2 Mounting	42
3.6.3 Specimen Preparation for Optical Microscopy	42
3.6.4 Measurement of Primary Dendrite Spacing	44
3.6.5 Specimen Preparation for Electron Probe Micro analyzer (EPMA)	45
3.6.6 Measurements on Electron Probe Micro Analyzer	46

Chapter 4 Results and Discussion	54
4.1 Primary Dendrite Spacing (PDS)	54
4.2 Mechanism of Adjustment of Primary Dendrite Spacing to Freezing Rate Change	66
4.3 Solute Redistribution	66
4.4 Effect of Abrupt Change in Freezing Rate on Solute Concentration in the Liquid Ahead of the Dendrite Tip	72
4.5 Calculation of Heat Transfer Coefficient	77
Chapter 5 Conclusions	79
References	81
Appendix A Temperature Measurements	A1
Appendix B Determination of Position of Solid/Liquid Interface	A14
Appendix C Procedure to Determine True Lammellar Dendrite Spacing	A18
Appendix D PDS Measurement Data	A20
Appendix E Measurement on Electron Probe Micro Analyzer	A25
Appendix F Theoretical Expression for Solute Redistribution	A30
Appendix G Determination of Excess Solute in Enriched Layer	A34
Appendix H Determination of Heat Transfer Coefficient	A36

List of Tables

Table	Title	Page
3.1	Determination of actual freezing rates for 2 wt% Bi alloy.	39
3.2	Determination of actual freezing rates for 4 wt% Bi alloy.	39
3.3	Composition of the alloy obtained from area analysis	46
4.1	Steady state PDS values.	63
A.1	Variac Setting 92V	A1
A.2	Variac Setting 100V	A3
A.3	Variac Setting 110V	A5
A.4	Temperature distribution inside the crucible for 2 wt% Bi alloy	A7
A.5	Temperature distribution outside the crucible for 2 wt% Bi alloy	A8
A.6	Temperature distribution inside the crucible for 4 wt% Bi alloy	A9
A.7	Temperature distribution outside the crucible for 4 wt% Bi alloy	A10
A.8	Temperature distribution inside the solid	A11
A.9	Cooling Curve 1	A12
A.10	Cooling Curve 2	A13
C.1	Angle Measurement Data	A19
D.1	PDS measurement data on 2 wt% Bi alloy	A20
D.2	PDS measurement data for 4 wt% Bi	A23
E.1	Bi concentration data taken along the length of a dendrite for sample a3 (2 wt% Bi alloy)	A25
E.2	Bi concentration data taken along the length of an interdendrite for sample a2 (2 wt% Bi alloy)	A26
E.3	Bi concentration data taken across two dendrites for sample a2 (2 wt% Bi alloy)	A27
E.4	Bi Concentration Data taken across two dendrites for sample b2 (4 wt% Bi alloy)	A28
E.5	Bi concentration data taken near the interdendritic region for sample a4 (2 wt% Bi alloy)	A29
F.1	Concentration of Bi across the dendrite for sample a2 (2 wt% Bi alloy)	A32
F.2	Concentration of Bi across the dendrite for sample b2 (4 wt% Bi alloy)	A33

List of Figures

<i>Figure</i>	<i>Title</i>	<i>Page</i>
2.1	Schematic arrangement of a Bridgman apparatus (after Fu et.al. [5]).	5
2.2	Formation of new primary arms by branching from secondaries (after Flemmings [14]).	8
2.3	Basic solidification model for dendritic growth (after Laxmanan [15]).	9
2.4	Primary arm spacing with growth speed during constrained growth of binary alloys (after Chopra et.al. [18]).	11
2.5	Primary arm spacing with growth speed in directionally solidified Pb-10 weight pct. Sn (after Chopra et.al. [18]).	11
3.1	Sn-Bi equilibrium diagram [22].	16
3.2	Gas purification train.	18
3.3	Specimen Capsule.	20
3.4	Schematic of Directional Solidification Apparatus.	23
3.5	Temperature Profile in the furnace at different variac settings.	30
3.6	Temperature Profile inside and outside the Crucible for 4 wt% Bi alloy.	31
3.7	Temperature Profile inside and outside the Crucible for 2 wt% Bi alloy.	32
3.8	Temperature Profile inside the melt for 2 wt% Bi alloy.	33
3.9	Temperature profile in the solid and liquid regions for 4 wt% Bi alloy.	36
3.10	Variation of temperature with time for 4 wt% Bi alloy.	37
3.11	Slicing holder.	41
3.12	Area analysis for sample a3 (2 wt% Bi) at the top end of the sample.	47
3.13	Area analysis for sample a3 (2 wt% Bi) at the bottom end of the sample.	47
3.14	Area analysis for sample b2 (4 wt% Bi).	48
3.15	Variation of Bi concentration with distance for sample a3 (2 wt% Bi alloy).	49
3.16	Line scan taken over interdendritic band for sample a2 (2 wt% Bi).	50
3.17	Variation of Bi concentration with distance for sample a2 (2 wt% Bi alloy).	52
3.18a	Point scan taken across two dendrites for sample a2 (2 wt% Bi).	53
3.18b	Point scan taken across two dendrites for sample b2 (4 wt% Bi).	53
4.1	Longitudinal section of Sn-2 wt% Bi alloy.	55
4.2	Corresponding Transverse section of Sn-2 wt% Bi alloy.	55
4.3	Starting position of solid/liquid interface for a Sn-2 wt% Bi alloy	56
4.4	Primary dendrite spacing with freezing rate for Sn- 2 wt% Bi alloy.	58
4.5	4.5: Primary dendrite spacing with freezing rate for Sn- 4 wt% Bi alloy.	59
4.6	Immediate increase in PDS with increase in Freezing rate.	62
4.7a	Steady state PDS values with Freezing rates 2 wt% Bi alloy.	64
4.7b	Steady state PDS values with Freezing rates for 4 wt% Bi alloy.	65
4.8	Photograph showing the Primary→Tertiary→Primary change.	67
4.9	Photograph showing the Primary→Tertiary.	67

4.10	Photograph showing the Primary→Tertiary at high magnification.	68
4.11	Point scan across two dendrites on sample a2 (2 wt% Bi).	69
4.12	Point scan across two dendrites on sample b2 (4 wt% Bi).	70
4.13	Transient solute distribution in solid resulting from an instantaneous change in growth velocity from R_1 to R_2 at location x_1 (after Smith et.al. [27]).	74
4.14	Bi concentration variation with distance near the interdendritic region.	75
4.15	Point analysis near the interdendritic region for sample a4 (2 wt% Bi alloy).	77
C.1	The transverse (A) and longitudinal (B) sections in a right-handed Cartesian co-ordinate system.	A18
G.1	Determination of excess solute in the enriched layer	A34
H.1	Temperature at different points below the equilibrium solid/liquid interface	A37

Chapter 1

Introduction

The control of morphology and characteristic microstructural spacing by directional solidification of alloys is a very powerful tool in solidification processing. Theoretical models and extensive experimental studies have now well established the morphology transition from planar-to-cellular-to-dendritic microstructure as function of growth velocity. However the response of the primary dendrite spacing, a very important microstructural feature in directional solidification, to sudden changes of growth rate is not adequately understood.

Experimental studies of dendrite structures in directionally solidified binary alloys show that dendritic structures develop certain steady characteristics at the advancing front, whereas at the interface regions further behind the advancing front, a non-steady-state evolution of side branches occurs.

The movement of stable and planar solid/liquid interface through directional solidification produced single crystals for computer chips and solar cells. Perfectly aligned, laminated composite structures have been possible through directional solidification in order to impart superior properties in superalloys such as high strength, durability and reliable performance in high temperature applications. Turbine blades with vastly improved properties have been made with directional solidification techniques.

The purpose of this research was to study the growth rate dependence of the primary arm spacing in well-characterised dilute binary alloys (Sn-Bi) with a

relatively high partitioning coefficient and solute redistribution. The samples were solidified under a wide range of freezing rates by directional solidification. The solute redistribution was determined with the help of an Electron Probe Micro Analyzer. From the experimental measurement of temperatures and cooling rate, heat transfer coefficient has been calculated. This was then compared with the values calculated using an empirical relation proposed in literature for a system comparable to the present system.

The alloy compositions have been chosen so as to be considerably lower than the maximum solid solubility in order to primarily have a single-phase dendritic growth. Directional solidification was carried out by traversing the furnace upwards with different freezing rates. The furnace was made to move at four different freezing rates ranging approximately from 30-300 $\mu\text{m/s}$. Unidirectional solidification was achieved by maintaining a fairly constant, pre-set temperature gradient. Microstructural study has revealed that the alloys adopt a planar arrayed dendritic morphology. Higher rates of growth observed to result in finer dendrite spacing. Experiments were carried out with two different alloy compositions.

In these experiments a cylindrical pyrex/quartz crucible containing the alloy was kept stationary surrounded by a furnace. A water spray was used to withdraw heat and bring about solidification. This spray-cooling device was attached to the furnace so that it moved with the furnace. To bring about directional solidification, furnace with the water spray chill was made to move up at a predetermined rate. Thus the thermal fields around the alloy in the crucible remained nearly constant throughout the directional solidification.

When the furnace was moved abruptly from a slower speed to a higher speed, the solid/liquid interface lagged behind. But when the furnace was moved from a faster speed to a slower speed, the solid/liquid interface leads, i.e. it moved ahead of the position where a change in the furnace traverse rate was imposed. Primary dendrite spacing was measured along with the length of the whole ingot after it properly sectioned and microstructure developed. The dendrite spacing exhibits the expected variation with freezing rate. It exhibits a linear relationship with growth rates on a log-log plot. Results obtained are compared with those cited in literature.

Chapter 2

Literature Survey

It is understood from past works, that directional solidification techniques where growth velocity and the thermal gradient at the solid-liquid interface are controlled, is important in fields concerned with solidification. A lot of research work has been done on directional solidification of alloys. Work on heat transfer in directional solidification has been done

- Experimentally,
- Computer modeling of heat flow problem associated with unidirectional solidification solved by numerical techniques,
- Computerised thermal analysis of cooling curves to quickly and accurately obtain solidification parameters such as growth rate, thermal gradient etc.

Significant experimental work [1-5] and theoretical work [6-10] has been reported for the Bridgman-type of crystal growth configurally providing the thermal conditions which are more amenable to meaningful thermal analysis. The results of heat transfer analysis have in principle been confirmed in corresponding experimental investigations.

In the present chapter a theoretical analysis of solidification in Bridgman apparatus, movement of solid liquid interface, free and constrained dendritic growth, primary dendrite spacing, solute redistribution and heat transfer coefficient as reported in the literature have been summarised.

2.1 Thermal Analysis of Bridgman Apparatus

A number of variations to the construction of Directional Solidification equipment have been described. Heat is fed into the specimen from the hot region, it flows through an insulated region in which there is less radial exchange of heat and is extracted in the colder region via a cooling device. Figure 2.1 shows the schematic arrangement of Bridgman apparatus. Growth is promoted by traversing the furnace or the sample. The thermal profile along the furnace axis is obtained in a prior experiment with the help of a thermocouple to give information on the thermal environment. The thermal profile in the metal during growth will differ from that of its environment, and it has thus been common to insert a thermocouple in the specimen in order to monitor thermal gradients in the melt. The thermal profile within the sample is independent of growth speed. It is determined by the imposed thermal profile i.e. the hotzone and cold zone temperatures and length of the insulated zone. The temperature gradient in the vicinity of solid-liquid interface is an important factor. The avoidance of constitutional supercooling for single-phase growth and achievement of cooperative growth of off-eutectics often requires that the temperature gradient be high.

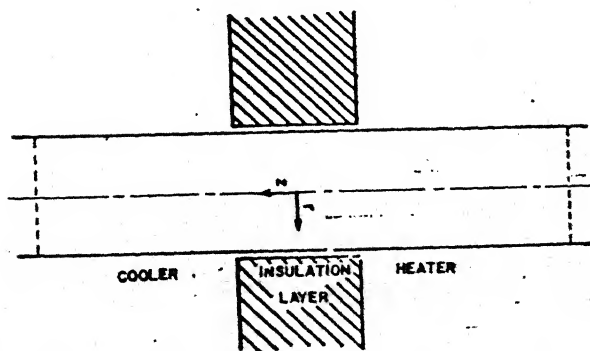


Figure 2.1: Schematic arrangement of a Bridgman apparatus (after Fu et.al. [5]).

2.2 Movement of Solid/Liquid Interface

The macroscopic solid/liquid interface shape is determined by heat transfer and by the direction of heat flux near the interface. It was suggested that one way of decreasing the dependence of interface shape on thermal conditions is to insert a layer of insulation between the heater and the cooler forcing the heat transfer to be axial [5]. It was observed both experimentally and mathematically [1,6] that during growth, the velocity of the advancing interface may be greater or lesser than the furnace traverse speed and that the steady state can never be set-up. It was also observed [6] that departure from ideal behaviour is low for metals with low thermal diffusivity. Cast iron, Pb which are low melting point metals, solidify at almost the traverse speed of the furnace over most of the length. The thermal diffusivity of Sn is also low so, the interface is expected to move with the same velocity as the furnace for the directional solidification of Sn.

Fu et.al. [11] observed that when the furnace movement rate is increased, the solid/liquid interface moves lesser distance than the distance travelled by the furnace. The time taken by the interface to reach a new equilibrium position is computed.

The equation is ,

$$\frac{\delta_2 - \delta}{\delta_2 - \delta_1} = \frac{V_2 - V_s}{V_2 - V_1} = e^{-B^* \theta} = e^{-\eta t} \quad (2.1)$$

where δ = interface position measured downward,

δ_2 = equilibrium interface position at the new drive rate V_2 ,

δ_1 = equilibrium interface position at the original drive rate V_1 ,

V_s = freezing rate at any time t ,

θ = dimensionless time and

t = time taken to reach a new equilibrium position.

2.3 Free and Constrained Dendritic Growth

With directional solidification various microstructural manipulations are possible by changing the experimentally controllable parameters. The development of microstructure depends on the manner in which the latent heat of fusion is carried away from the advancing solid/liquid interface [12]. Two distinctly different heat flow conditions may give rise to either the free growth or the constrained growth behaviour. In free growth, where the solidification occurs in an undercooled melt, the latent heat is dissipated through the liquid. In the constrained growth, the latent heat is carried away through the solid and the temperature gradient in the liquid ahead of the interface is positive. This constrained growth condition gives rise to directional solidification. Free dendritic growth arises when a crystal nucleus grows in a supercooled melt.

Dendritic solidification [13] is characterised by a morphology resulting into spikes in specific crystallographic directions, with regular branches in other equivalent directions. In face-centered and body-centered cubic structures dendritic growth is observed to take place in the cube directions, of which there are three that are mutually perpendicular. The main experimental observations are:

- Dendritic growth takes place only when the melt is supercooled.
- The directions of growth are always strictly crystallographic.
- Branching occurs at regular spacing.

2.4 Primary Dendrite Arm Spacing

A convenient and widely used measure of solidification conditions on dendritic structure is dendrite arm spacing. Columnar dendrites adjust their primary spacing during growth in accordance with the imposed thermal conditions. If the spacing is too close one or the other primary arm falls and is subsequently engulfed. If the spacing is too large a tertiary arm growing from a secondary arm catches up to the growing primary tips and becomes one of them as shown in Figure 2.2. The driving force is the constitutional supercooling between the two primary dendrite arms.

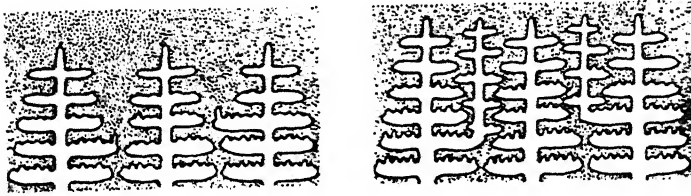


Figure 2.2: Formation of new primary arms by branching from secondaries (after Flemmings [14]).

Basic solidification model [15] for dendritic growth under an imposed positive thermal gradient in the liquid is shown in the Figure 2.3. Many theoretical and experimental studies have been reported on primary dendrite arm spacing, λ . Hunt [16] derived an expression

$$\lambda_1 = A_1 G_1^{-0.5} V^{-0.25} \quad (2.2)$$

where λ_1 = Primary dendrite spacing,

G_1 = Temperature gradient and

V = Growth velocity.

Flemmings presented an expression for high values of heat transfer coefficient,

$$\lambda_1 = A(G_1 V)^{-3/8} \quad (2.3)$$

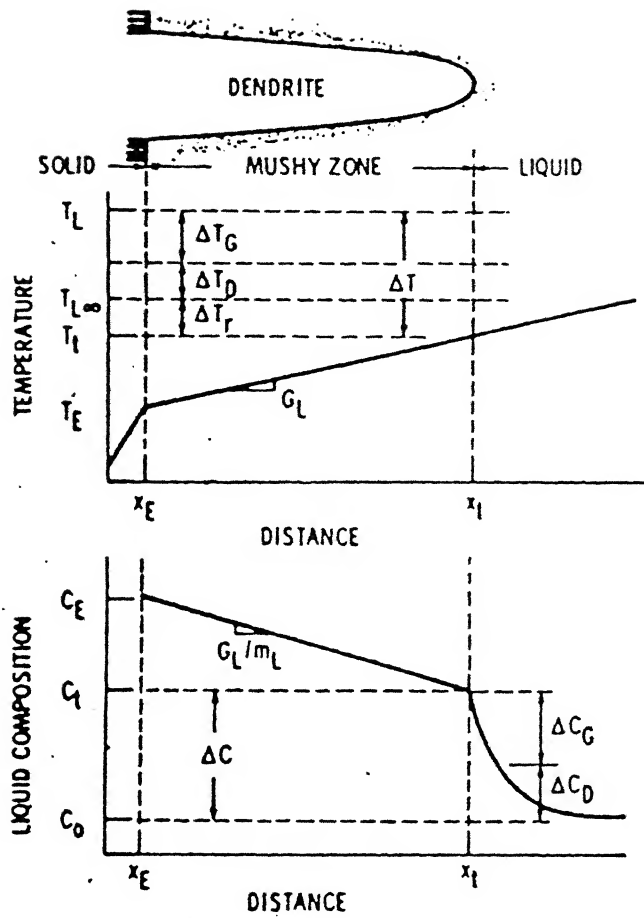


Figure 2.3: Basic solidification model for dendritic growth (after Laxmanan [15]).

Dominique et.al. [17] have derived a formula for the primary dendrite arm spacing in steady state heat flow. The primary dendrite arm spacing λ_1 , is given as

$$\lambda_1 = 120 \left(\frac{160 X_0^{1/2} G_0 (\varepsilon \sigma) T_m D}{(1-K)m \Delta H G R} \right)^{1/2} \quad (2.4)$$

where X_0 = solute mole fraction at bulk composition,

G/G_0 = normalised temperature gradient,

- G = temperature gradient at the tip ($K\ cm^{-1}$),
 ε = scaling factor for the surface tension,
 σ = liquid-solid surface energy ($erg\ cm^{-2}$),
 T_m = melting temperature of the pure solvent (K),
 Δ = chemical diffusivity of solute in the liquid ($cm^2\ s^{-1}$),
 m = liquidus slope (K),
 ΔH = heat of fusion ($J\ cm^{-3}$) and
 R = tip velocity ($cm\ s^{-1}$).

They also suggest that a relation like

$$\lambda_1 = K(GR)^{-1/3} \quad (2.5)$$

also adequately explains experimental data for steady state growth.

Experimental studies on the growth speed dependence of primary spacing ' λ ' have been carried out in various alloy systems [18]. Figure 2.4 schematically represents the literature reported dependence of the primary arm spacing (λ_1) on growth speed. Region A starts from R_p , the growth speed for the initial break down of a planar liquid/solid interface. ' λ_1 ', primary arm spacing initially decreases with increasing R , growth speed. A minimum in ' λ_1 ' occurs at R_{min} . The spacing increase with increasing ' R ' in region B, until a maximum is reached at R_{max} beyond which it decreases in region C. As shown in Figure 2.5 the primary arm spacing increases at first, with decreasing growth speed (or decreasing gradient of constitutional supercooling), reaches a maximum, and then decreases with further decrease in growth speed as shown in Figure 2.5. A majority of the primary dendrite spacing measurements reported in the literature as well as the present work has been done in

the region 'C' (Figure 2.4) where primary dendrite spacing decreases with increasing

R.

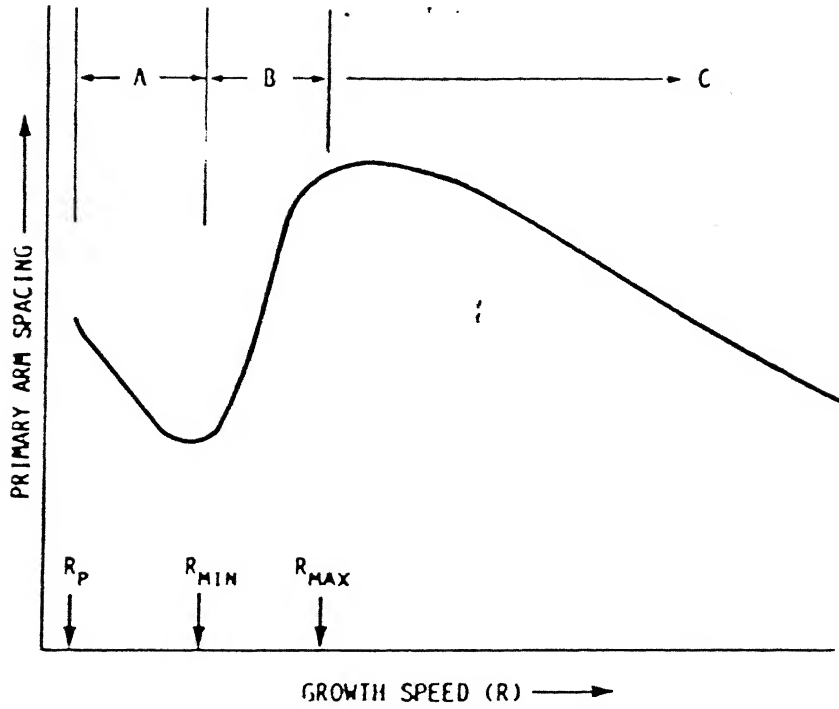


Figure 2.4: Primary arm spacing with growth speed during constrained growth of binary alloys (after Chopra et.al. [18]).

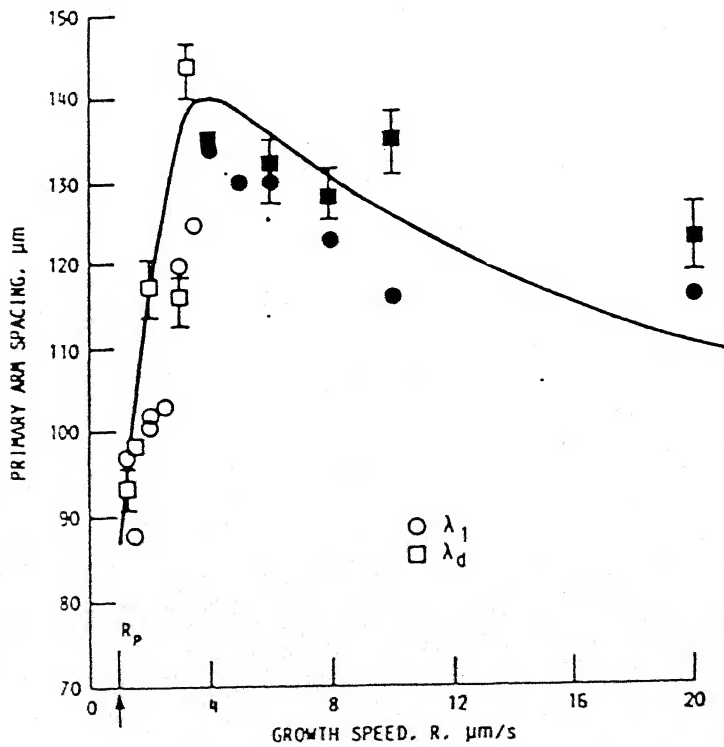


Figure 2.5: Primary arm spacing with growth speed in directionally solidified Pb-10 weight pct. Sn (after Chopra et.al. [18]).

2.5 Solute Redistribution

If an alloy of uniform composition is solidified under non-equilibrium conditions a redistribution of the impurity occurs, so that the resulting solid is not of uniform composition, that is, segregation occurs during solidification. The problem of calculating solute distributions for steady state conditions and for the transient changes in solute concentrations were first reported by Rutter et.al. [19].

Solute redistribution during dendritic solidification with diffusion in the solid was reported by Ganesan et.al. [19]. The composition of the interdendritic liquid during solidification is calculated from the average diffusion parameter. The equation is given as,

$$\frac{C_L}{C_0} = (1 - (1 - 2\bar{\alpha}K)f_s)^{(K-1)/(1-2\bar{\alpha}K)} \quad (2.6)$$

where $\bar{\alpha}$ = average diffusion parameter,

C_L = concentration in the liquid,

C_0 = alloy composition,

f_s = weight fraction solid and

K = partitioning coefficient.

The solute redistribution equation for the undercooled dendrites is given by

Sarreal et.al. [20]

$$C_s^* = KC_t \left\{ \frac{a}{K-1} + \left(1 - \frac{aK}{K-1} \right) \left(\frac{1-f_s}{1-f_{s0}} \right)^{K-1} \right\} \quad (2.7)$$

where C_s^* = concentration of solute in the solid,

f_s = solid weight fraction,

f_s = 0 at the centre of the dendrite,

f_s = 1 at the centre of the interdendritic region,

K = equilibrium partition ratio,

C_t = composition of the liquid ahead of the dendrite tip,

f_s^o = fraction solid with a constant concentration of $K C_t$

$$a = \frac{-D_L G}{m_L \cdot R \cdot C_o} \quad (2.8)$$

where D_L = diffusion coefficient of solute in the liquid,

G = temperature gradient in the liquid,

R = growth rate,

C_o = initial average composition,

m_L = slope of the liquidus,

C_t = composition of the liquid ahead of the dendrite tip given as

$$C_t = (1-a) C_o.$$

Fraction eutectic is calculated as,

$$f_E = (1-f_s^o) [C_s^{\max}/KC_t]^{1/(K-1)} \quad (2.9)$$

The above equations have been used in the present work for the calculation of concentration of solute in the solid.

2.6 Empirical Relation for Heat Transfer Coefficient

An empirical relation for computing the heat transfer coefficient given by Kern [21] on the inner wall of an annulus for laminar flow of water for Reynolds number in the range of 200 to 2000. The equation is

$$h_i = 0.67 \left[\frac{K^3 \rho^2 g}{\mu_f^2} \left(\frac{C \mu_f^{5/3}}{KL \rho^{2/3} g^{1/3}} \right) \right]^{1/3} \left(\frac{4G'}{\mu_f} \right)^{1/9} \quad (2.10)$$

where K = thermal conductivity of water,

ρ = density of water,

g = acceleration due to gravity,

L = total length over which the heat transfer is taking place,

μ_f = average film temperature,

C = specific heat of water,

$4G/\mu_f$ = Reynolds number.

Heat transfer coefficient calculated with this equation is compared with experimentally determined heat transfer coefficient.

Chapter 3

Experimental Procedure

The thermal profiles and freezing rate in the specimen are determined in the directional solidification apparatus. The position of the solid-liquid interface and the axial thermal gradients on each side of the interface can be controlled. The rate of freezing can be changed instantaneously. The present work was carried out in an existing directional solidification apparatus. The alloys used for this study are dilute alloys of Bi in Sn. Figure 3.1 shows the Sn-Bi equilibrium diagram. Sn-Bi is a classical binary eutectic system with a eutectic temperature of just 139°C which gives rise to the current and increasing application of alloys around eutectic composition as low temperature soft soldering alloys. The two and four weight percent Bi alloys were chosen for the present work to study the response of primary dendrite to changes in the freezing rate with respect to their spacing and solute redistribution. The various units and accessories used to carry out the master alloys preparation and Directional solidification, are briefly described below.

3.1 Master Alloy Preparation

In the present work Sn-Bi alloys were prepared in an inert atmosphere in an existing experimental set-up. The experimental set-up consisted of:

1. Gas Purification Train,
2. Vacuum Pump and
3. Rocking furnace.

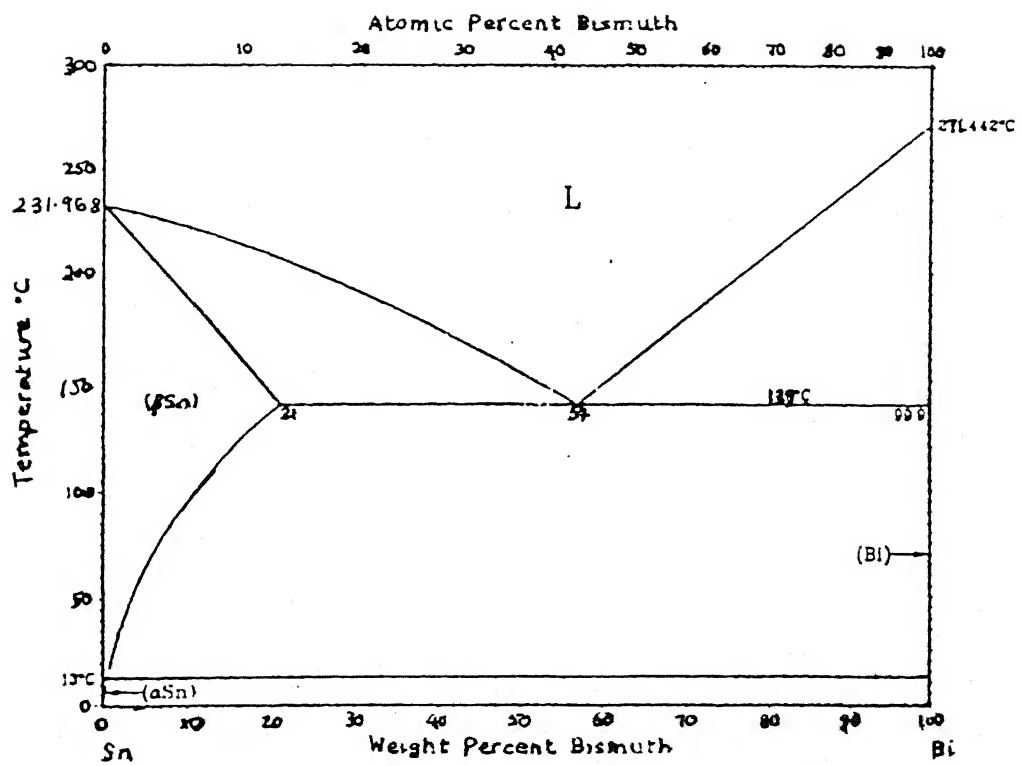


Figure 3.1: Sn-Bi equilibrium diagram [22].

Sn and Bi of 99.99% or better purity were used. The melting points of Sn and Bi are 231.967 °C and 271.442 °C [22] and their densities at room temperature are 7.3 and 9.8 g/cm³.

3.1.1 Gas Purification Train

The argon to be supplied to maintain inert atmosphere around the melt must be free of carbondioxide, oxygen, moisture and other gaseous impurities. Removal of these impurities was accomplished in a gas purification train. Figure 3.2 shows the gas purification train.

The gas train consisted of separate glass containers with soda lime, silica gel, anhydrous CaCl₂, molecular sieve of 4Å size at liquid N₂ temperature and copper turnings kept at 500 °C, as shown in Figure 3.2. The soda lime was prepared by mixing in dry powder from.

Silica gel and anhydrous CaCl₂ were to remove moisture, soda lime to remove CO₂ and molecular sieve at liquid N₂ temperature to remove traces of CO₂, O₂, moisture and other gaseous impurities. The copper turnings were meant to remove any oxygen that may still be remaining in the gas. The hot and purified gas coming from the copper turnings tube is then made to pass through a condenser for cooling and then through the bubbler containing the dibutylphthalate, with methyl orange for colouring. The purified argon gas coming out from the bubbler is directed through a two-way valve to the Directional Solidification Apparatus or to the specimen capsule placed in the Rocking furnace, through another two way valve which permits evacuation of the specimen tube, if desired.

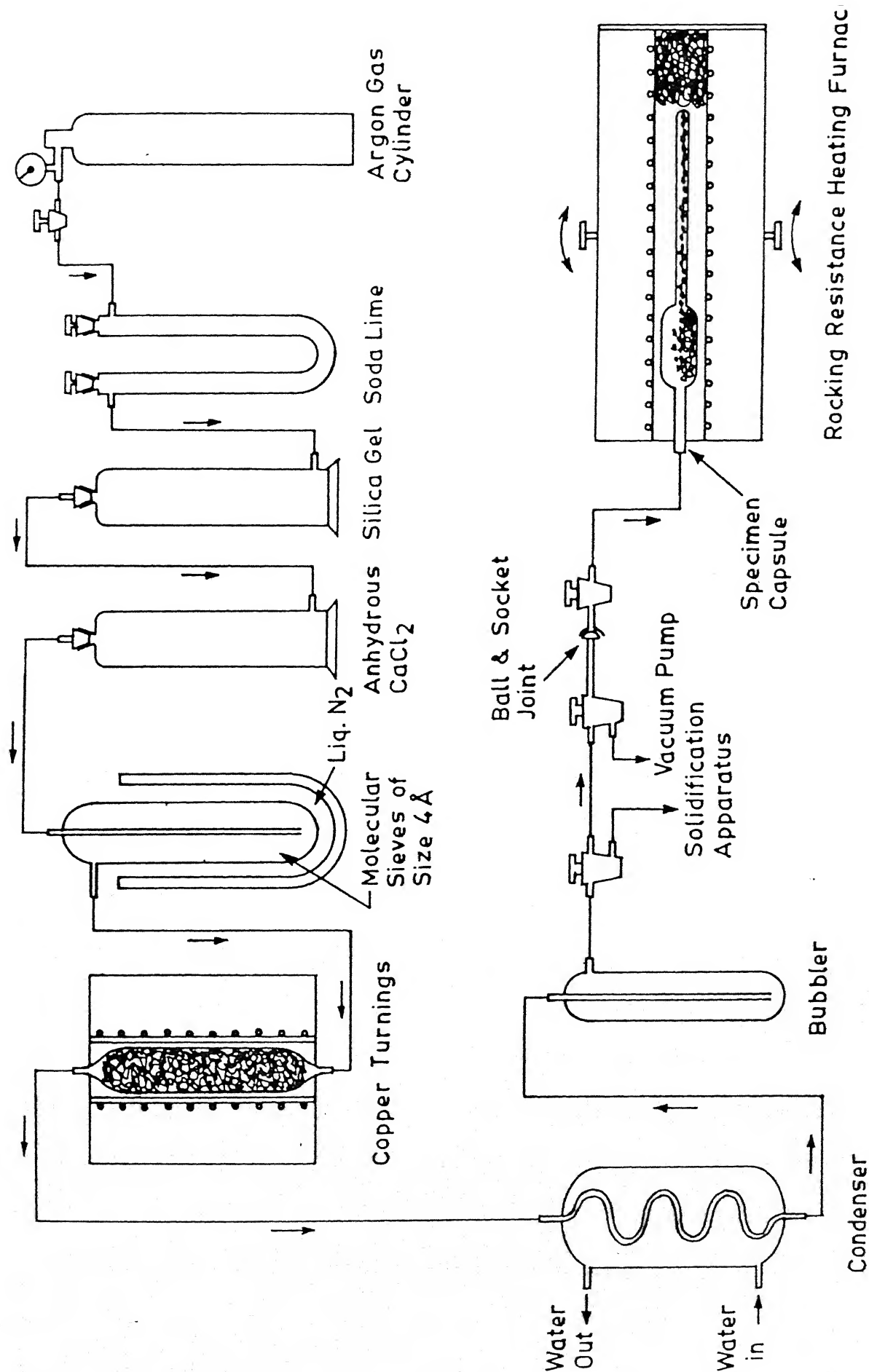


Figure 3.2: Gas Purification Train.

3.1.2 Vacuum Pump

A mechanical vacuum pump (Hind Hi-Vac) was used to permit evacuation of the specimen tube for repeated flushing with purified argon gas.

3.1.3 Rocking Furnace

The length of the rocking furnace was about sixty centimetre and it was resistance heating type. The internal diameter of the furnace tube was three centimeters. The furnace is held at the centre of its length by two diametrically opposite horizontal pivots. It can be rocked from a vertical position to about 30° below the horizontal line, through an angle of 120° . The furnace can be damped at any convenient position within an angle of approximately 30° on either side of the horizontal position. The far end of the furnace was closed with insulating material to support the end of the specimen tube. A chromel-alumel thermocouple sheathed in a two-hole ceramic sheathed, with both ends open, was used to control the operating temperature of the furnace. The furnace temperature was maintained at 350°C , to make the alloy.

3.2 Specimen Capsule

In the present work, melting, mixing, ingot casting and directional solidification was carried out in a pyrex/quartz capsule. The capsule shape is shown in Figure 3.3. It consisted of two parts: a bulb portion for holding alloys in solid state and for proper mixing after melting and a cylindrical tube like portion for casting and subsequent used for directional solidification. After the alloy was allowed to solidify in the cylindrical portion, the bulb portion of the capsule was cut and saved for use again.

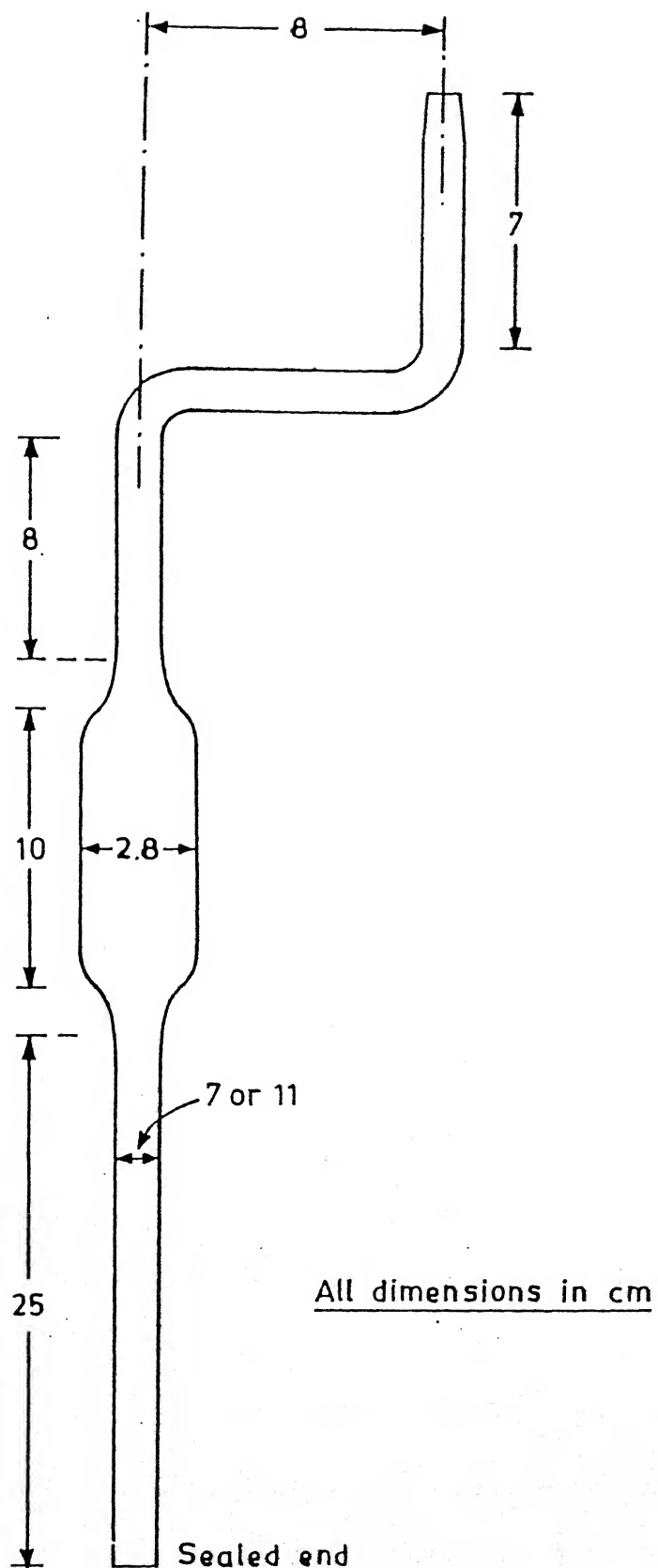


Figure 3.3: Specimen Capsule.

3.3 Master Alloy making

Two master alloys were made one with 2 wt% Bi and other with 4 wt% Bi. The 2 wt% alloy was prepared in a pyrex capsule while 4 wt% alloy was prepared in a quartz capsule. The cylindrical tube like portions were of 7.5 mm and 10.5 mm inner diameter for the pyrex and quartz capsules, respectively. The reason for using quartz capsule was that quartz has much better thermal shock resistance. The 4 wt% Bi alloy in the quartz capsule was to be subjected to several cycles of starting and stopping of the water spray on the outer spray of the tube during the run. The reason for using two different diameters were,

1. To see if diameter of the ingot changes the solidification behaviour of the ingot in anyway. For example the shape of the solid-liquid interface.
2. In an earlier similar study [23] approximately 10.5 mm inner diameter specimen tube was used. It was thought that using the same diameter would permit a better comparison between the results of the two investigations.

Tin and Bismuth were weighed in required amounts to form a Sn-Bi alloy and then filled in the pyrex/quartz capsule. The specimen capsule was then kept in the rocking furnace and its open end was connected to the vacuum pump and purified argon gas supply through a two-way stop-cock. Initially, the capsule was evacuated and back filled with purified argon gas a few times to remove all traces of air. Then the alloy was heated first to 100°C. At 100°C, again the process of evacuation and backfilling was carried out three times. The process of evacuation and backfilling was repeated after heating the specimen tube to 200°C, 300°C and 350°C. The charge was kept at 350°C under argon atmosphere for two hours to ensure complete melting. The furnace then was gently rocked about 20 times, first slowly moving upwards and then

downwards from the horizontal position through an angle of about 40° . After rocking is over, the capsule was again evacuated and backfilled with argon three times. The furnace was rocked as above again for another 20 times to ensure proper mixing of the melt. The rocking furnace with the capsule was then allowed to cool down to 250°C in the furnace, before the capsule was taken out for further cooling first in the air to allow it to solidify and subsequently quenching in room temperature water. The lower cylindrical portion carrying the solidified ingot was chopped off from the bulb portion. The cylindrical portion containing the alloy was subsequently used for directional solidification.

3.4 Directional Solidification Apparatus

A schematic of the Directional Solidification system used in the present study is shown in Figure 3.4. It consisted of three zones; a heated zone, an insulated zone of high thermal gradient, and a cooling zone. The system consists of an electric motor, a resistance heating furnace, a copper crucible holder and a water spray type chill assembly.

The furnace is connected to a motor through a guide-way pulleys via rope and counter weights. A brief description of these sub-systems follows. Heat enters the specimen from the hot region, flows through the insulated region exchange, and is extracted below via a cooling device. The furnace and the chill assembly were moved with respect to a stationary crucible. The moving furnace and chill assembly maintained a constant thermal gradient in front of the solid-liquid interface throughout the run. The molten alloy in the crucible is made to solidify starting from its bottom towards the top.

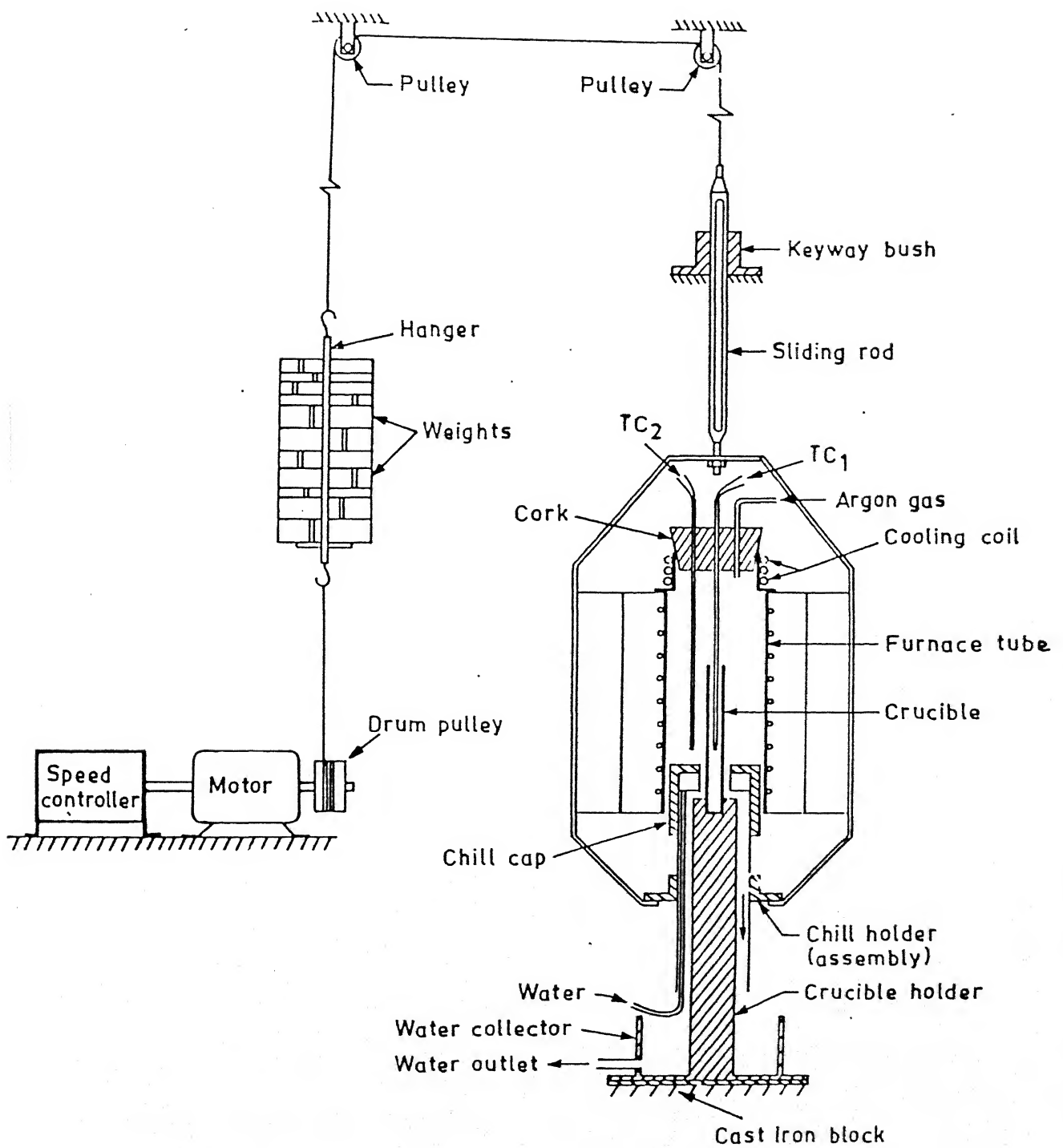


Figure 3.4: Schematic of Directional Solidification Apparatus.

3.4.1 Drive Mechanism

The furnace motion was controlled by a motor operating over two pulleys to the furnace support assembly. The electric motor Hans Heynau was a Germany make 14-volt dc, 3000 rpm, motor model F9M2 with gear number G2V5M5 and a tachometer number F9T and a four quadrant transistor controller number SV031 a. It is capable of giving $0.004 - \pm 11.6$ rpm with continuous and instantaneous variation. The speed of the motor was controlled by a controller in which there is a ten turn potentiometer head. By rotating the head of speed of the motor was changed. Calibration of this ten turn potentiometer head for different speeds was done.

3.4.2 Furnace and its Motion

The furnace tube is 17 inches long and 2 inches internal diameter. The heating is provided by the Kanthal wire of 19 gauge wound around in tube. It was ensured that the furnace moved only in a vertical line without any axial rotation, because the furnace movement is the sole cause of the solidification to proceed unidirectionally.

The furnace was provided with a frame which was bolted to a slotted steel rod which hangs from a flexible wire rope. The other end of the rope was attached to the drum pulley of the drive motor via a counter-weight to counter balance the weight of the furnace.

An arrangement was made at the top of the furnace (Figure 3.4) to insert two thermocouples, one for controlling the temperature inside the furnace and the other for measurement of temperature inside the melt in the crucible. A tube is provided for flushing the furnace tube with purified argon.

3.4.3 The Crucible Stand

The crucible stand was a brass rod of length 42.47 cm and mounted on a metallic plate. The bottom end of the cylindrical pyrex/quartz crucible containing the solidified ingot was kept in the blind hole of the crucible stand at the top. The crucible was held along the furnace axis. The blind hole is of depth 1.4 cm. Three screws are provided to hold the crucible firmly and vertically along the furnace axis. An aluminum foil was wrapped inside the blind hole. This helped in preventing the danger of cracking of the crucible bottom when the screws are tightened. The crucible stand on the base plate was provided with a metallic receptacle with a drain pipe. The water impinging on to the crucible from chill, drips down the brass rod to this receptacle, where it gets collected and drained out. The base plate was fixed rigidly to a cast-iron block. The cast iron block damped vibration which may come from the floor.

3.4.4 Chill Assembly and Chill Cap

Main objectives of chill for the system are:

- To extract heat effectively from the crucible, to bring about solidification.
- To allow relatively high thermal gradients in the liquid at the solid/liquid interface.
- Capability to place the chill at a desired position in the furnace.

The chill system provided water jets to impinge over crucible in an annular shape and the water then dripped down the crucible stand. The water jets were arranged through a hollow stainless steel ring surrounding the crucible. There were 14 jets each of 1 mm diameter arranged in two circles. The water was fed to the cooling ring through a copper tube of 4.7 mm internal diameter. The chill assembly was made with stainless

steel to avoid rust and corrosion. Water is fed to chill from a water reservoir maintained at a constant height. The chill assembly was fixed to the frame of the furnace so that the chill moved with the furnace, past the stationary specimen.

•

A *Chill Cap* was provided with the following objectives.

- To provide insulation between the heated portion and the chilled (cooled) portion of the specimen.
- To seal off the chill from the furnace atmosphere, thereby minimising the local disturbance of temperature due to proximity of chill.

The chill cap was cup shaped with 3-4 mm wall thickness and about 2 cms ID. Its length was about 8 cm.

The material for chill cap was alumina. It was chosen because of its refractoriness and insulating properties. The hole in the cap, also helped in keeping the crucible in vertical position. A thermocouple was fixed, with Plaster of Paris mixed with Hypophosphoric acid, at the top of the chill cap to monitor temperatures at the top of the chill cap.

3.5 Steps for Making a Directional Solidification Run

Experiments were conducted with the equipment described in the previous sections to accomplish Directional Solidification of various Sn-Bi alloys with different freezing rates. The steps involved were:

1. Assembling the Apparatus for a Run
2. Measuring steady state temperature along the length of the furnace for different power inputs to the furnace.
3. Measuring temperature profile inside and outside the crucible along its length.

4. Determination of the position of the solid-liquid interface w.r.t. the chill ring and bottom of the crucible.
5. Determination of temperature at different points below the solid-liquid interface (in the solid portion of the specimen).

3.5.1 Assembling the Apparatus for a Run

The pyrex/quartz crucible with the solidified ingot in it was placed in the blind hole of the crucible stand and tightened with the help of three screws provided for this purpose. The crucible stand was then fixed to the cast iron block with the help of allen screws. Care was taken to align the crucible with the axis of the crucible holder. The chill assembly tube was fixed at the required position. Slowly the furnace was lowered to the point when the chill ring was a few mm above the top of the crucible stand. A cork was affixed at the top end of the furnace which has a cooling arrangement by water circulation through a spiral copper tube around it. There were provisions in the cork for passing purified argon gas for continuous flushing of the melt surroundings and for introducing three Chromel-Alumel thermocouples. One thermocouple used for maintaining the desired temperature inside the furnace, another thermocouple was used for measuring the temperature outside the specimen tube. The central thermocouple used to monitor the temperature profile within the specimen (liquid as well as solid portions) was sealed in 3mm ID vycor tube. The thermocouple emf's were measured by a DC Potentiometer, Mahindra & Mahindra, Model LA-10. Two of the thermocouples (meant for measuring temperature outside and inside the crucible) are connected to the potentiometer through a toggle switch. By operating the toggle switch the emf's one of the thermocouples was measured at a time. For controlling the temperature inside the furnace, the thermocouple was connected to an

indicating temperature controller (Indotherm 401). The temperature controller was capable of maintaining the temperature of the furnace to within $\pm 2^{\circ}\text{C}$ of the set temperature. Purified argon was made to flow into the furnace before the alloy starts melting. The flow was maintained at around 200 bubbles per minute to prevent the alloy from oxidation. The chill water was also turned on. The chill water flow rate was maintained at 280 cc per minute. The temperatures of the water entering and leaving the chill assembly was measured. The water inlet to the chill assembly is from a reservoir kept in a fixed position. A steady water level was maintained in the reservoir.

3.5.2 Measuring Steady State Temperature along the Length of the Furnace

The temperature along the length of the furnace was measured for three different variac sittings. This was performed as a guide to the behaviour expected during a run. This was carried out by slowly moving a thermocouple sheathed in ceramic sheath along the length of the furnace in the absence of crucible and chill assembly, i.e. furnace tube with both ends open. The Plot of temperature profiles in the furnace for different power inputs is shown in the Figure 3.5. The measurement data is given in Appendix A (Tables A.1, A.2 and A.3).

3.5.3. Measuring Temperature Profiles inside and outside the Crucible

For the measurement of temperature profile outside the crucible under experimental conditions, a thermocouple protected with a ceramic sheath was used. The thermocouple was slowly moved along the length of the furnace until the thermocouple tip touched the chill cap. Another thermocouple sheathed in 3mm ID vycor tube closed at one end was used for the measurement of temperatures inside the

melt. The glass tube with the thermocouple is made to touch the solid/liquid interface. In this position, the tip of the thermocouple was at 2mm distance from the solid/liquid interface. The temperature gradient in the liquid along the axis, at the solid/liquid interface has calculated from the recorded temperatures inside the melt. The temperature distributions in the liquid ahead of the interface and the temperature distribution just outside the crucible were simultaneously measured, using a DC potentiometer. The plots of the temperature profile in the liquid ahead of the solid-liquid interface and outside the crucible are shown in the Figure 3.6 for 4wt% Bi alloy. Temperature profiles for 2wt% Bi alloy are shown in Figure 3.7. The temperature measurement data are given in Appendix A (Tables A.4, A.5, A.6 and A.7). The temperature gradients existing in front of the solid/liquid interface was determined from the plot of the temperatures in the melt for 2 wt% Bi alloy as shown in Figure 3.8. The temperature gradient obtained for 2 wt% Bi alloy was $8.4^{\circ}\text{C}/\text{mm}$.

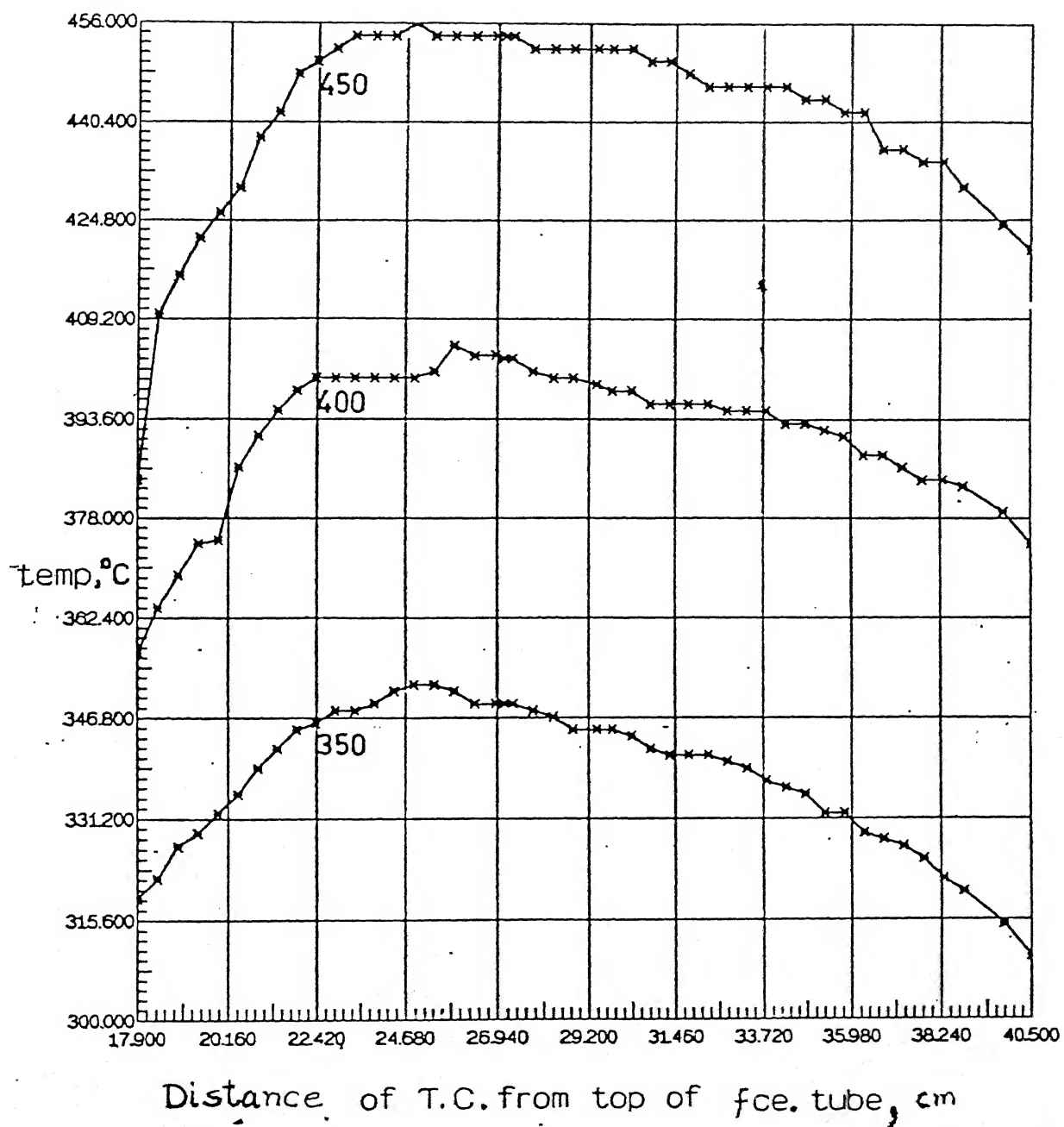


Figure 3.5: Temperature Profile in the furnace at different variac settings.

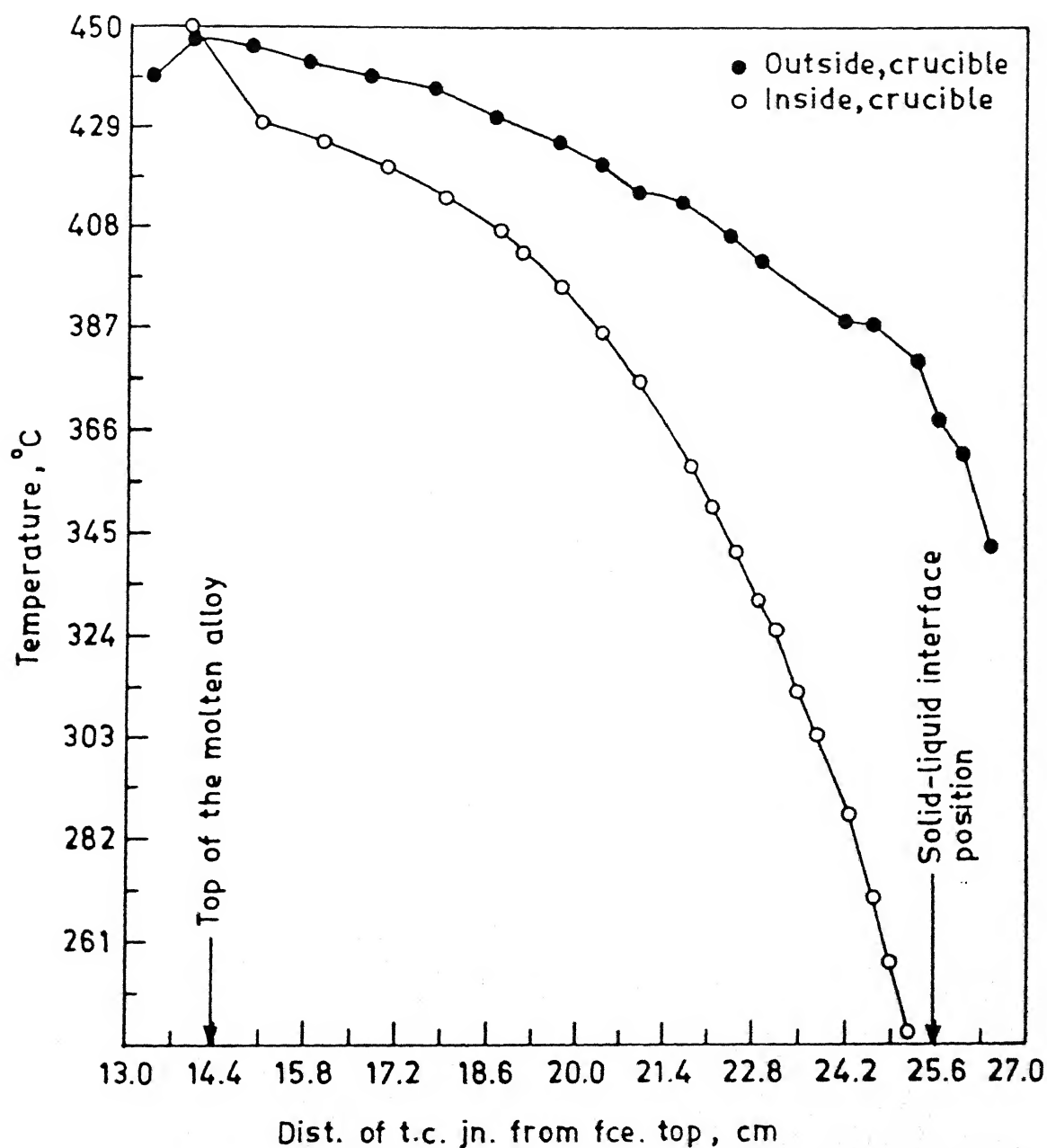


Figure 3.6: Temperature Profile inside and outside the Crucible for 4 wt% Bi alloy.

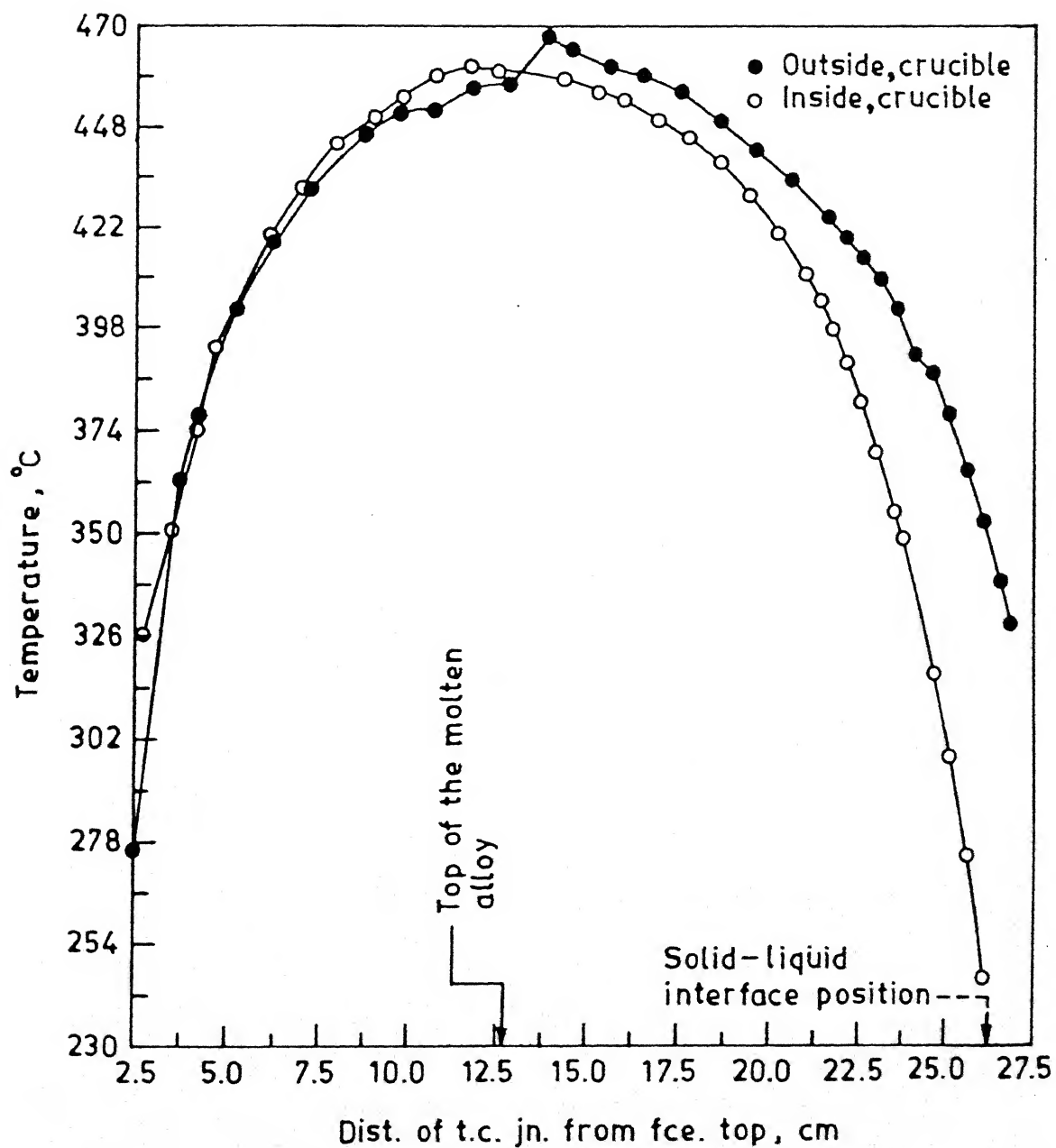


Figure 3.7: Temperature Profile inside and outside the Crucible for 2 wt% Bi alloy.

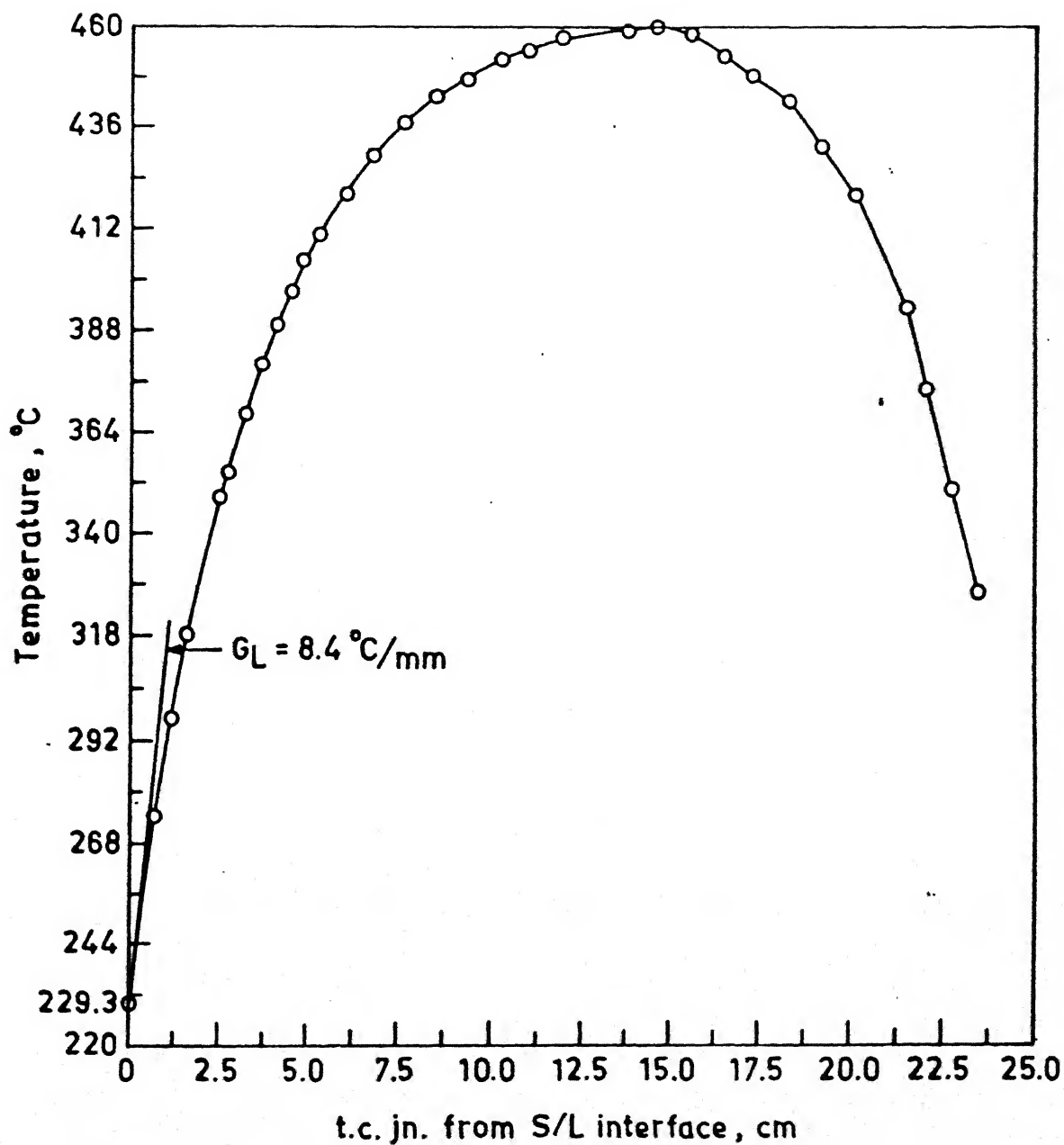


Figure 3.8: Temperature Profile inside the melt for 2 wt% Bi alloy.

3.5.4 Determination of Position of Solid/Liquid Interface

The position of solid/liquid interface is determined with respect to top of the chill ring and the bottom of the specimen tube. The power switch was turned on for the furnace to heat up. Gradually the furnace picks up the temperature and the ingot starts melting from top, towards the chilled portion. A steady state is achieved when the rate of heat input to the melt became equal to the rate of extraction of heat by the chill water and the ingot stand. This ensured that the solid-liquid interface was stationary and in dynamic equilibrium. The location of the freezing interface was monitored by periodically lowering the central thermocouple which is sealed in glass until it encountered the solid alloy. This was repeated quite a few times until the interface position stabilized. The position of the top of the thermocouple sheath was recorded by a cathetometer. The unchanged reading of the thermocouple top in the cathetometer and the unaltered emf of the thermocouple tip in the potentiometer ensured that the equilibrium has been attained. Initially, the furnace and the interface are stationary. From the fixed lengths and variable distances (measuring after equilibrium is attained) the initial interface position with respect to the chill, and the bottom of the crucible were determined. This is explained in detailed in Appendix B.

3.5.5 Determination of Temperature at Different Points below the Equilibrium Solid/Liquid Interface

Temperature at several points below the equilibrium solid/liquid position were determined in the 4 wt% Bi alloy. The following procedure was adopted for this purpose. The thermocouple sheathed in 3 mm ID vycor is lowered until it touches the solid/liquid interface corresponding temperature reading was noted. Then the chill water impinging onto the crucible was turned off. As a result of stopping the cooling

water-spray on the specimen, the solid/liquid interface recedes to a lower position, i.e. close to the crucible bottom. After 5 minutes the thermocouple is lowered to a desired point above the new solid/liquid interface position. Then the chill water is turned on again so that the solid/liquid interface moves up to the previous position in the specimen in a few minutes of time. The corresponding temperature reading in the potentiometer was noted at that position of thermocouple tip below the solid-liquid interface. The chill water is again put off, the thermocouple is positioned at a different depth. Now the chill water was put on again. The temperature corresponding to that position of the thermocouple was noted after steady state has been reached. The above procedure is repeated at different positions of the thermocouple tip below the equilibrium solid/liquid interface in the solid with chill water on. The corresponding data is shown in Appendix A (Table A.8). The temperature profile in the solid and the liquid regions for 4 wt% Bi alloy is shown in Figure 3.9. The temperature gradient in the liquid for 4wt% Bi alloy is measured from the plot in Figure 3.9 is $7.8^{\circ}\text{C}/\text{mm}$. These measurements were made to calculate the heat transfer coefficient.

Variation of temperature with time was measured at two positions below the equilibrium solid/liquid interface starting from the time when the water flow is the chill ring was restarted. The temperature was noted down every 30-40 secs till the temperature reached a steady state value. Figure 3.10 shows the variation of temperature with time for the two positions, 0.89 cm and 2.85 cm below the solid/liquid interface respectively. The data for the temperatures recorded is shown in Appendix A (Table A.9 and A.10).

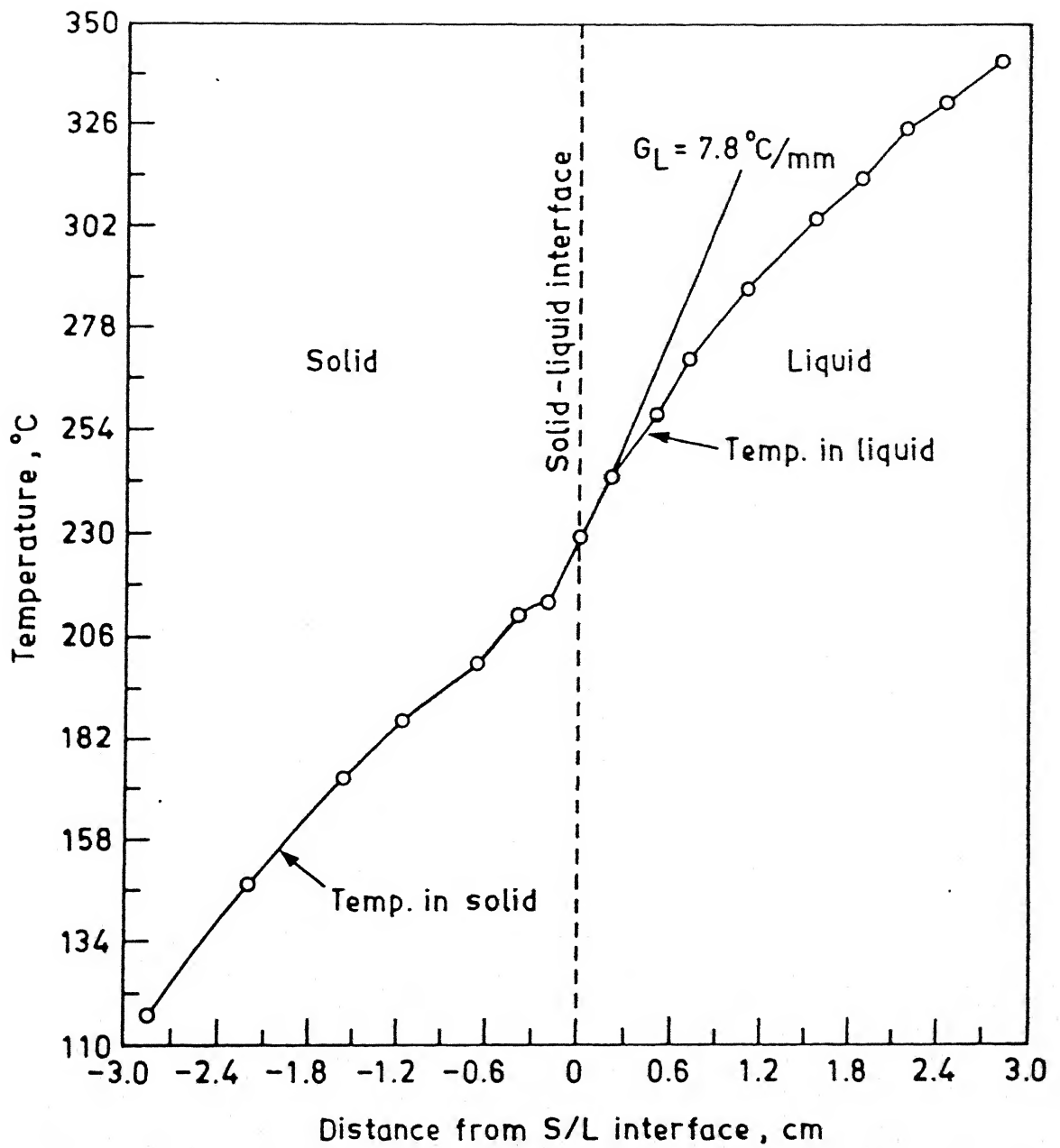


Figure 3.9: Temperature profile in the solid and liquid regions for 4 wt% Bi alloy.

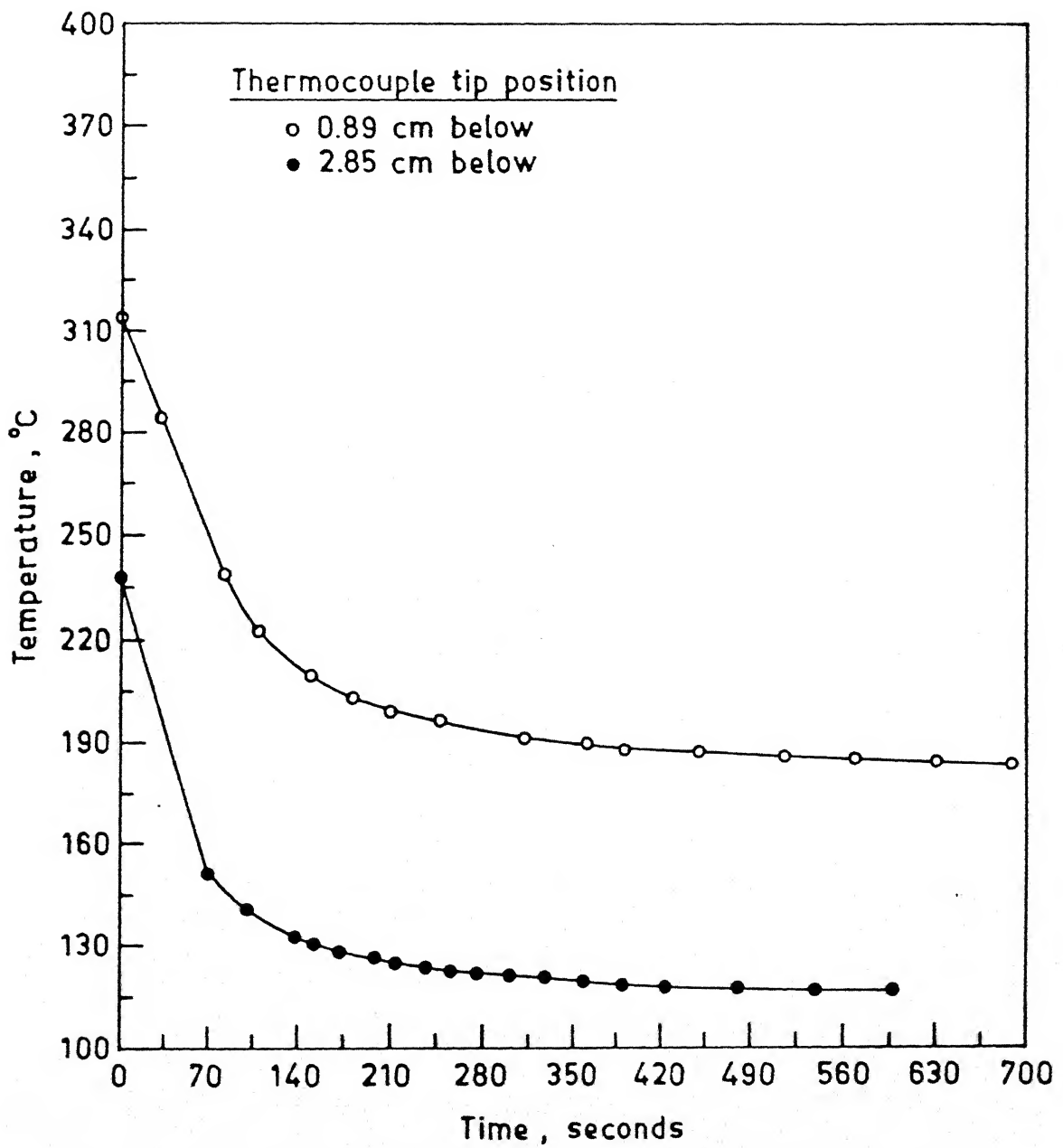


Figure 3.10: Variation of temperature with time for 4 wt% Bi alloy.

3.5.6 Directional Solidification Runs

The rate at which the crystalline solid is formed in a cooling melt is determined by the rate at which heat is removed. If the latent heat is not removed by conduction processes, it eliminates the supercooling and suppresses the solidification process. The directional solidification of the alloy is achieved by moving the furnace with the chill assembly at different rates with a predetermined flow rate of water in the chill, so that the thermal environment was always the same. Four approximate growth rates were pre-selected for different lengths of each run. The thermocouple sheathed pyrex tube was used to locate the position of the Solid/Liquid interface at the beginning of the run. Then this thermocouple was pulled up several centimeters and left there. A mark was made on the furnace before the run. The initial position of the mark was noted in the cathetometer. The speed of the electric motor was controlled with a ten turn potentiometer. Desired speeds of the furnace were set using the speed control potentiometer. Finally the motor switch was turned on for the directional solidification to start. The stop watch was also turned on immediately. After a desired length had solidified at the preset growth rate, the speed of the motor was changed suddenly to a new value by changing the potentiometer setting of the controller, the time of this speed change was noted and the stopwatch was again turned on. Thus the change in growth velocity from one value to another was instantaneous. The cathetometer readings are also noted at the beginning and the end of different rates of freezing. The actual speed with which the furnace was moving was calculated from the cathetometer readings taken during different rates of freezing (by tracking the index mark on the furnace through the telescopic sight of the cathetometer) and the time taken by the furnace to travel that distance, with the help of a stopwatch. During the run, the inlet water temperature and the outlet water temperature was measured .

After the solidification run is completed, the power supply and the chill water was turned off. The argon gas supply was stopped after the furnace temperature came down to 100 °C. The crucible with the directionally solidified ingot was carefully withdrawn from the furnace. It was then broken in order to recover the directionally solidified ingot. One ingot each for 2wt% and 4wt% Bi was directionally solidified in this manner. The corresponding data for the runs are given in Table 3.1, Table 3.2.

Table 3.1: Determination of actual freezing rates for 2 wt% Bi alloy.

Sr. No	Potentiometer setting	Time interval in sec	Cathetometer readings in cms	Diff. bet. Cathetometer in cms	Actual freezing rate in $\mu\text{m/sec}$
1.	3.902	573.5	Initial 16.69 Final 18.69	2	34.87
2.	3.990	123.0	Initial 18.69 Final 22.19	3.5	284.45
3.	3.902	685.0	Initial 22.19 Final 25.34	3.15	43.79
4.	3.970	261.2	Initial 25.34 Final 29.379	4.039	154.63

Table 3.2: Determination of actual freezing rates for 4 wt% Bi alloy.

Sr. No	Potentiometer setting	Time interval in sec	Cathetometer readings in cms	Diff. bet. Cathetometer in cms	Actual freezing rate in $\mu\text{m/sec}$
1.	3.898	708.5	Initial 16.57 Final 18.77	2.2	31.05
2.	3.984	126.2	Initial 18.77 Final 22.07	3.3	261.49
3.	3.917	287	Initial 22.07 Final 25.37	3.3	114.98
4.	3.898	340.5	Initial 25.37 Final 27.57	2.2	64.61

While trying to measure the temperature profile in the solid at various points below the solid liquid interface, pyrex for 2wt% Bi-Run 1, the Pyrex crucible with the molten alloy in it, was exploded and about 40% of the molten alloy fell into the cast-iron block. The crucible material used was pyrex. Another attempt to find the temperature profile in the solid, was made for 2wt% Bi- Run 2 with the molten alloy

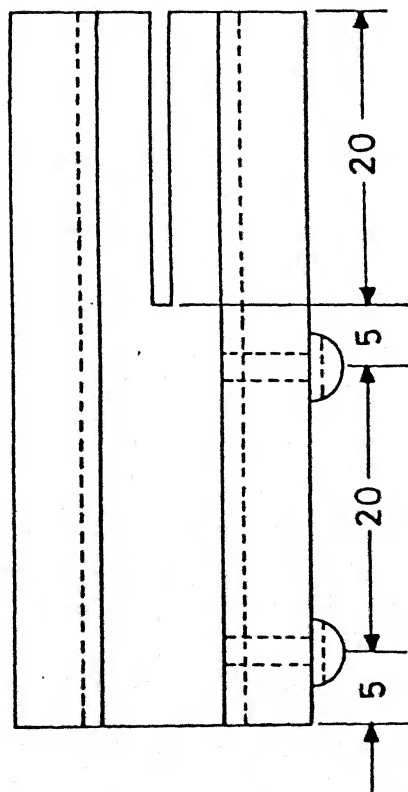
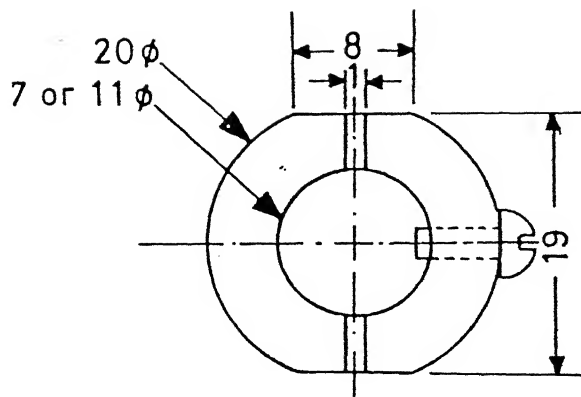
in pyrex crucible. The crucible got cracked at the bottom. The experiment was stopped. The solidified ingot was taken out of the cracked crucible and kept in another pyrex crucible, and run 3 was carried out. Because of this, a Quartz crucible was used for 4wt% Bi alloy directional solidification run.

3.6 Specimen Preparation and Observations

The Directionally solidified ingot was cut into pieces using a slicing holder and mounted using cold mounting material. The longitudinal and transverse sections of ingot prepared by grinding, polishing and etching for metallographic examination. PDS measurements were done on longitudinal sections. A few of the samples were further prepared for solute redistribution studies using an Electron Probe Micro Analyzer.

3.6.1 Slicing of the Ingot

Microstructural studies were carried out on both longitudinal and transverse sections of the directionally solidified ingot. The change in the primary dendrite arm spacing at different rates of freezing were measured. Therefore, it was necessary to part the cylindrical ingot longitudinally into two halves. Then, one of the halves was cut at different lengths, to observe the transverse section. For cutting the ingot a slicing holder was used. The schematic of the slicing holder is shown in Figure 3.11. Two different holders were used as the diameter of the two ingots were different. It consists of a slot of one millimetre width at the center which acted as a guide for a manually operated jeweler's saw while slicing through the specimen. The slicing holder was held in a bench-vice.



Scale = 2:1
All dimensions in mm

Figure 3.11: Slicing holder.

Ample care was taken to include the initial solid/liquid interface position in the first piece of the ingot. Small notches are made on the two longitudinal sections cut, at various distances from the bottom of the ingot, at the points where a change in freezing rate had been effected. While cutting the ingot half into smaller lengths, care was taken to cut it sufficiently away from the points where a change in freezing rate had been made.

3.6.2 Mounting

For microstructural observations each of these pieces are mounted on a cold setting mounting material. Powdered resin was mixed with hardener in a 1:1 ratio and a thin paste was made. Before mounting the sample, the longitudinal section of the sample was ground to a flat face. A thin double sided adhesive tape was placed in the mold and then the sample was made to stick to the tape. This is to prevent the sample from any movement when the resin was poured over the sample to fill the cavity. After nearly twenty minutes the resin paste had polymerised into a hard mass and there by holding the sample in place. Before mounting, the mold cavity was greased for easy removal of the mounted samples. The specimen number and the direction of growth were marked on each mounted sample for identification. In a majority for cases two specimens were mounted in each mold of $1\frac{1}{4}$ " or $1\frac{1}{2}$ " dia. The specimen lengths varied approximately between 2-3 cms.

3.6.3 Specimen Preparation for Optical Microscopy

The mounted samples were given rough grinding on a belt grinder for revealing the transverse and longitudinal sections. Care was taken to see that the transverse and longitudinal sections are fairly orthogonal to each other. Any sharp

edge or extension of the mounting material was smoothed out during belt grinding. Then the samples were subjected to emery paper polishing. Application of pressure was avoided in order to preserve the solidification structure which would otherwise be lost by surface recrystallisation due to heat of friction. Polishing on emery papers was done only along one stroke in a sequential order from coarse to finer i.e. 1/0 to 4/0 size. The direction of polish was changed through 90 degrees while going for next finer emery paper. Final polishing was carried out on a polishing wheel using the fine MgO suspension (OP-S suspension of struers) on a polishing cloth. The scratch free polished samples were cleaned thoroughly first with tap water followed by distilled water. The clean specimens were then subjected to etching. The etchant used was of the following composition :

Potassium dichromate : 1 gram

Concentrated hydrochloric acid : 6 to 8 cc

Distilled water : 86 cc.

Etching was found to be more efficient if the etchant was poured on to the specimen so as to gently flow over the polished surfaces instead of just dipping the specimen into the etchant. A batch of etchant was used for etching 3-4 samples before being discarded. The etched specimens were cleaned off of the etchant first with tap water and then with distilled water. A little methanol was squirted on the specimen and then it was dried by the blower.

The technique of alternate polishing and etching helped in obtaining a satisfactory microstructure.

The etched sample was taken for measurement of primary dendrite spacing. The sample prepared was mounted on a glass slide with plasticene with the help of a specimen mounting press so that the surface under observation remained parallel to

the total plane of the microscope. The microstructure of the etched sample was first observed in a Nikon Stereoscopic zoom microscope, at low magnifications. Both the longitudinal as well as transverse sections were observed. The observations carried out in a longitudinal section was to note the number of grains present through out the sample and their orientation with respect to the longitudinal edge. The grains are so selected that they can be clearly followed from the bottom of the specimen to its top for further observation of PDS in an optical microscope. Photographs were taken on both the longitudinal and transverse sections near the common edge for the measurement of angles made by the plate-like dendrites with the edges. The angles are required in determining the true primary dendrite spacing.

3.6.4 Measurement of Primary Dendrite Spacing

A convenient and widely used measure of the effects of solidification conditions on dendrite structure is dendrite arm spacing. In the present work primary dendrite arm spacing measurements were carried out. The primary dendrite arm spacing were plate-like and sufficiently distinct to make reasonably accurate measurements.

Apparent primary dendrite arm spacing measurements were carried out with the help of a micrometer eyepiece fitted to one of the eyepiece tubes of a binocular microscope ('CENSICO' make). The specimen was aligned parallel to the edge of the glass slide prior to pressing. The binocular microscope is fitted with a mechanical stage, with verniers for movement in x & y directions. The edge of the specimen was aligned parallel with one of the stage verniers. The position of one end of each sample was noted on the vernier which is taken as the reference point for distances on that sample. PDS measurements were made approx. at every 2 mm intervals. The

micrometric eyepiece measurements were recorded and the number of dendrites for each observation were noted which gave the average dendrite spacing at that point. 3 to 4 observations of PDS were made at each interval of 2 mm. The readings are presented in Appendix D (Tables D.1 and D.2) and an average PDS for that location.

True dendrite arm spacing measurement

The grains selected for measurement on the longitudinal section should be visible on the transverse section also. These were photographed at the common edge on both longitudinal and transverse sections. A line is drawn parallel to the plate like dendrites and another line is drawn along the common edge on the photographs of transverse and longitudinal sections. The angles by the plate like dendrites on the longitudinal and the transverse sections are measured directly on the photographs for the calculation of 'K' the multiplication factor to get true lamellar spacing [24]. The calculation of K are given in Appendix C (Table C.1)

3.6.5 Specimen Preparation for Electron Probe Micro analyzer (EPMA)

2 wt% and 4wt% Bi samples are prepared for qualitative analysis in EPMA. For standards, Sn and Bi pellets of 99.99% or better purity were taken and remounted in 1.25 inch diameter molds with some of the already mounted Sn-2wt% Bi and Sn-4wt% Bi samples selected for investigation on EPMA (JEOL 8600). The samples were prepared again by polishing and etching as was done for samples for optical microscopy. For analysis on EPMA, the etching was much lighter. Care was taken not to etch the standard Sn and Bi pallets. 6 samples were prepared for analysis in EPMA. The position of changes in freezing rate were marked on the samples by a light scratch mark using a sharp pin.

3.6.6 Measurements on Electron Probe Micro Analyzer

The samples so prepared were used for quantitative analysis in the EPMA. Pure (99.99% or better) Sn and Bi pellets were used to get the X-ray count for standards, before making observations on the respective samples. All measurement were done on the longitudinal sections of the specimens. Photographs were also taken of the areas where measurements were made.

Area analysis was done for different samples at different points to get the average composition. Three area scans were taken one each on sample numbers a2 and a3 (both were 2 wt% Bi alloys) and b2 (4wt% Bi). Figure 3.12 and 3.13 show the photographs of the area where area analysis was carried out on a 2 wt% Bi alloy (sample a3) about 11.5 cms from the bottom of the ingot. The areas were so chosen as to include atleast 4-5 dendrite plates so that an average composition at that point in the ingot is obtained. the compositions of the alloy as obtained from area analyses is shown in Table 3.3. Figure 3.14 shows the area where area scan has been taken for sample b2 (4wt% Bi) and the corresponding composition is given in Table 3.3. A large difference between the nominal composition (according to the weights of the two components taken for making the alloy) and the composition's determined by EPMA for observation numbers 1 and 3, could be due to a possible error in obtaining correct count on the standards.

Table 3.3: Composition of the alloy obtained from area analysis

S.No	Sample identification	Position of scanned area w.r.t. the ingot bottom, cms	Nominal wt% Bi in the alloy	Wt% Bi
1.	Sample a3	11.5	2	2.517
2.	Sample a3	8.97	2	0.787
3.	Sample a2	7.03	2	7.769
4.	Sample b2	5.60	4	3.391

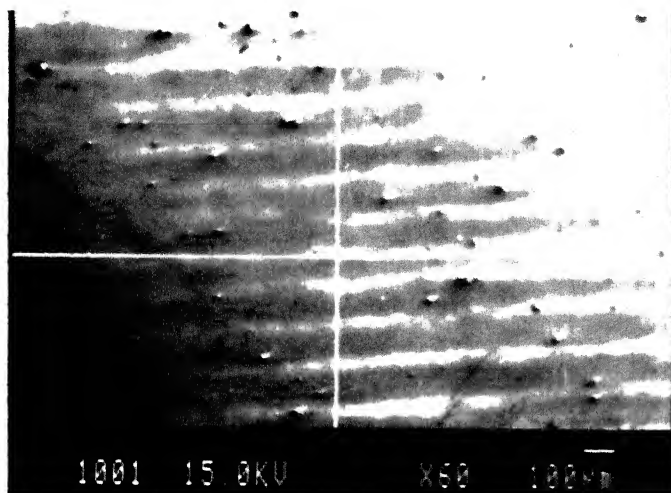


Figure 3.12: Area analysis for sample a3 (2 wt% Bi) at the top end of the sample.

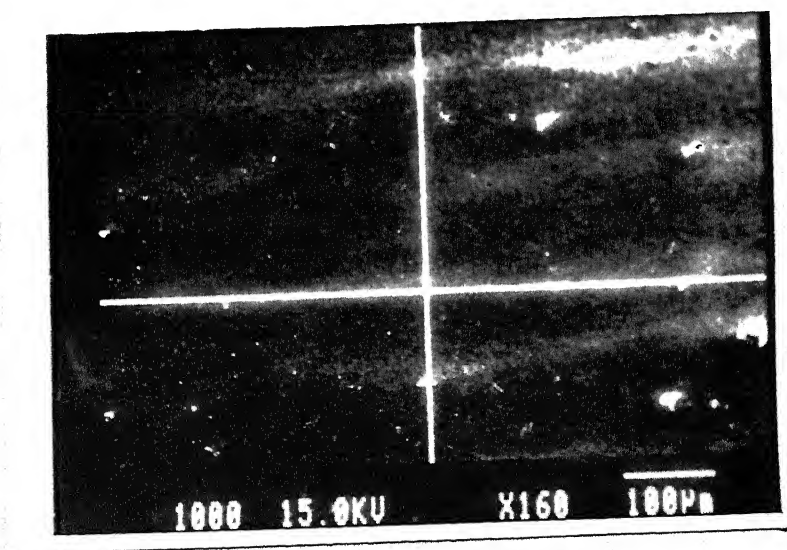


Figure 3.13: Area analysis for sample a3 (2 wt% Bi) at the bottom end of the sample.

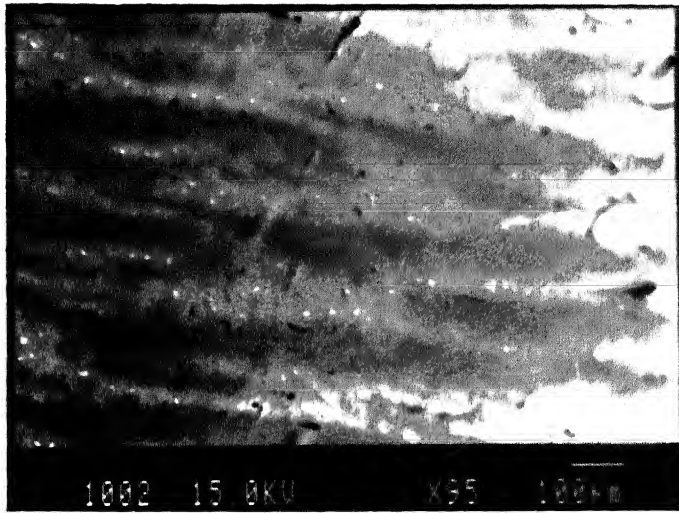


Figure 3.14: Area analysis for sample b2 (4 wt% Bi).

Point analysis was done along the length of a dendrite of interdendritic region for the samples of 2 wt% and 4 wt% Bi alloys. This point analysis was carried out on both sides of the point of expected change in freezing rate. Bismuth concentration was determined by EPMA at intervals of about 100 μ over a total length of about 2000 μ . The scan was taken along the center of the plate-like dendrite on the longitudinal section of sample a3(2 wt% Bi) of about 10.26 cms from the bottom of the ingot. The Bi concentration data is presented in Appendix E (Table E.1). The dendrite plates were approximately aligned along the X-axis at the time of placing the specimen in the sample holder of the EPMA. Since the specimen holder cannot be rotated, so a small adjustment was necessary on the y-axis so as to remain close to the centre of the dendrite plate (seen as a white band in the microstructure). Figure 3.15 shows the variation of Bi concentration with distance for sample a3. The freezing rate to the left of the arrow mark is 284 μ m/sec and to its right is 45.9 μ m/sec.

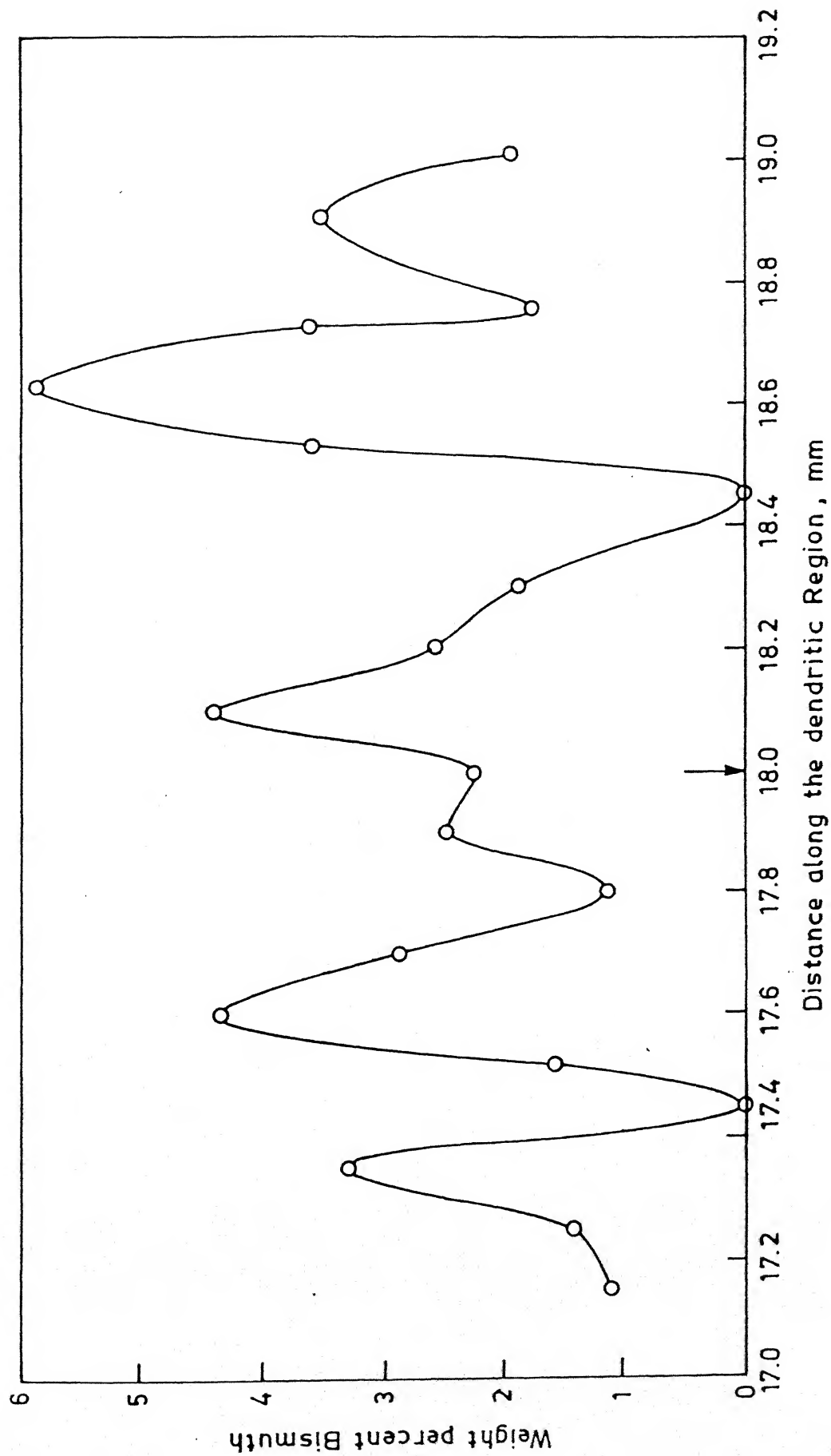


Figure 3.15: Variation of Bi concentration with distance for sample a3 (2 wt% Bi alloy).

A similar point scan was taken on the sample a2 (2 wt% Bi) over an interdendritic region (seen as a dark band separating two 'white' bands in the microstructure) about 6.9 cms from the bottom of the ingot. A small adjustment was necessary on the y-axis, to scan along the center of the interdendritic band. Figure 3.16 shows the dark interdendritic band (just above the horizontal marker line) over which the scan was taken.

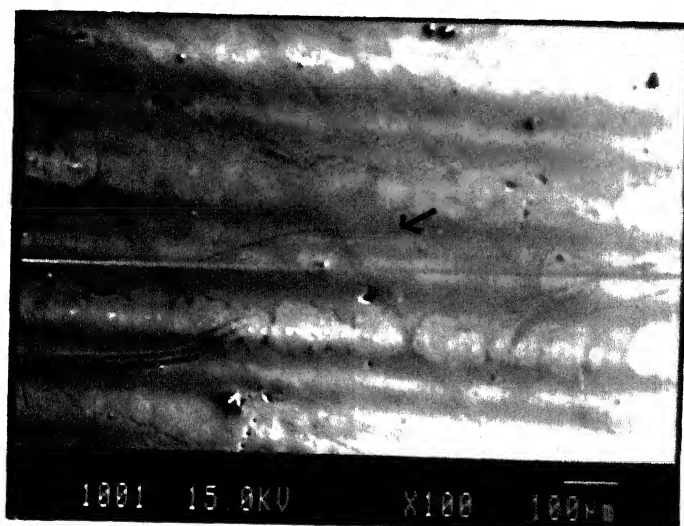


Figure 3.16: Line scan taken over interdendritic band for sample a2 (2 wt% Bi).

Table E.2 of Appendix E shows the Bi concentration data for this sample. Figure 3.17 shows the variation of the Bi concentration along the length of the interdendritic band. The freezing rate to the left of the arrow mark is $34.87 \mu\text{m/s}$ and to its right is $284 \mu\text{m/s}$.

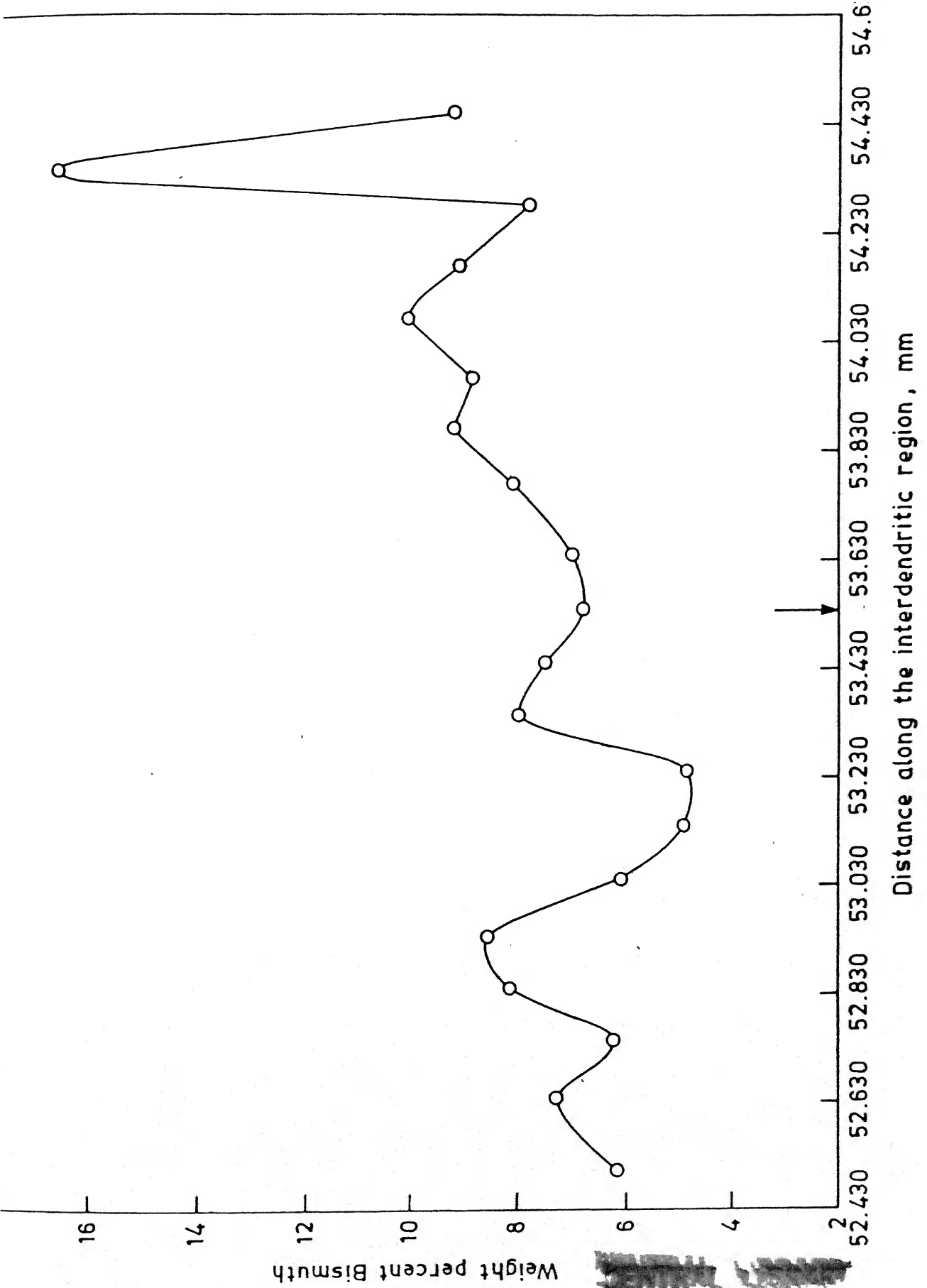


Figure 3.17: Variation of Bi concentration with distance for sample a2 (2 wt% Bi alloy).

127799

Point scans were taken approximately perpendicular to the dendrite growth direction across two dendrites on sample a2 (2 wt% Bi) and b2 (4 wt% Bi). The scans were taken on the longitudinal sections at 10-15 μ intervals covering approximately two dendritic plates. Figure 3.18a and 3.18b show the photographs of the region where the scans were taken. The end point of the scans are denoted by markers on the photographs. The tables of concentration vs. distance data of these two samples are given in Tables E.3 and E.4 of Appendix E. The concentration vs. distance plots are given in Figures 4.11 and 4.12 under the chapter 'Results and Discussion'.

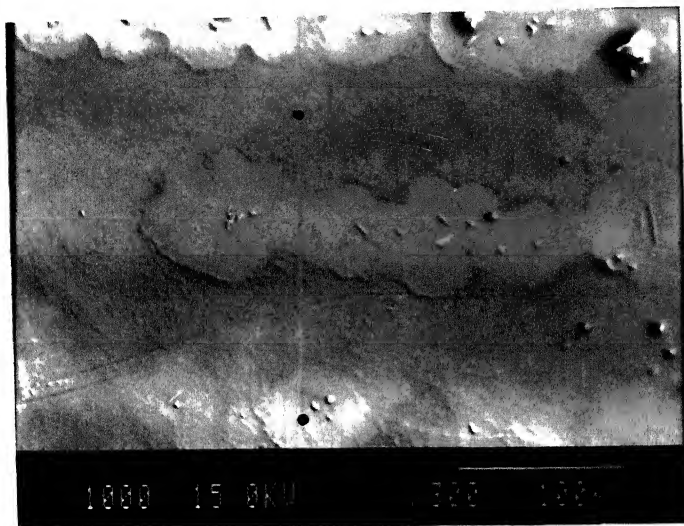


Figure 3.18a: Point scan taken across two dendrites for sample a2 (2 wt% Bi).

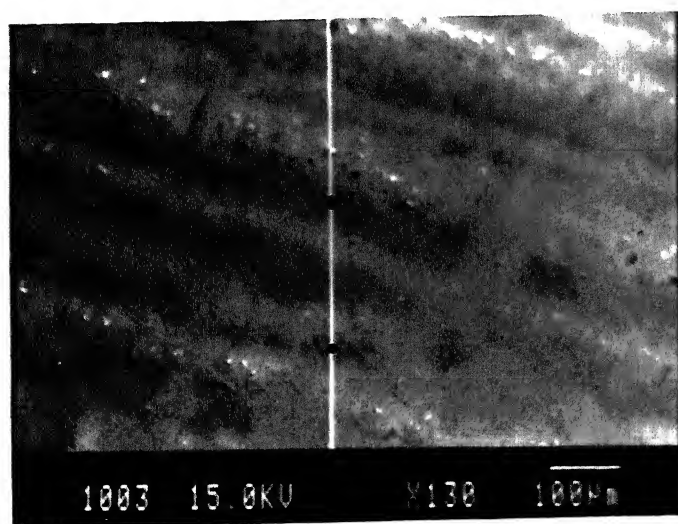


Figure 3.18b: Point scan taken across two dendrites for sample b2 (4 wt% Bi).

Chapter 4

Results and Discussion

The 2 and 4 wt% Bi alloys, which were directionally solidified, were subjected to microstructural examination and other measurements. The microstructural observations basically involved apparent Primary Dendrite Spacing (PDS) measurements. The discussion in this chapter is divided into primary dendrite spacing, mechanism of adjustment of primary dendrite spacing to freezing rate changes, solute redistribution during dendritic solidification and calculation of heat transfer coefficient.

4.1 Primary Dendrite Spacing (PDS)

There is a direct correlation between primary dendrite spacing and freezing rate. Thus, the fineness of dendrites can be controlled by controlling the freezing rate. In the present work, the spacing between primary platelets are measured. The primary dendrite spacing were measured perpendicular to their traces in the longitudinal section. Primary dendrites grow approximately parallel but opposite to the heat flow direction. Figure 4.1 and 4.2 show the longitudinal and transverse sections respectively, of a Sn-2wt% Bi alloy. From the appearance of the transverse and longitudinal section it is obvious to say that the dendrites are plate like and not rod-like in appearance. From the Figure 4.1 at the straight edge the grains are shown as number 1, 2 and 3. The orientation of platelets in different grains is different.

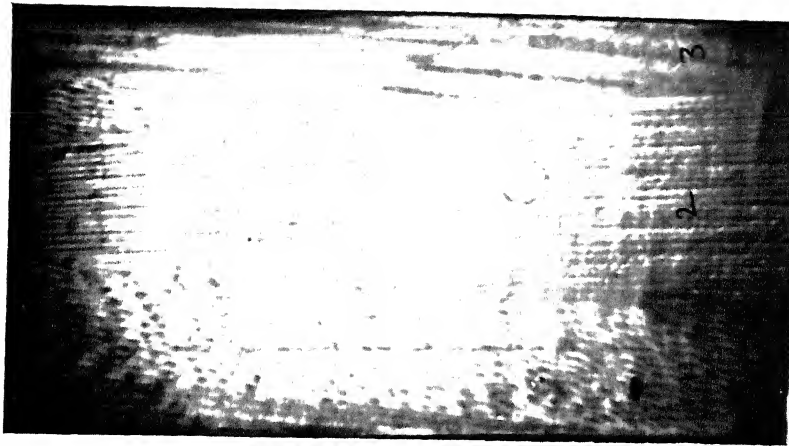


Figure 4.1: Longitudinal section of Sn-2 wt% Bi alloy.
Magnification 4.5x

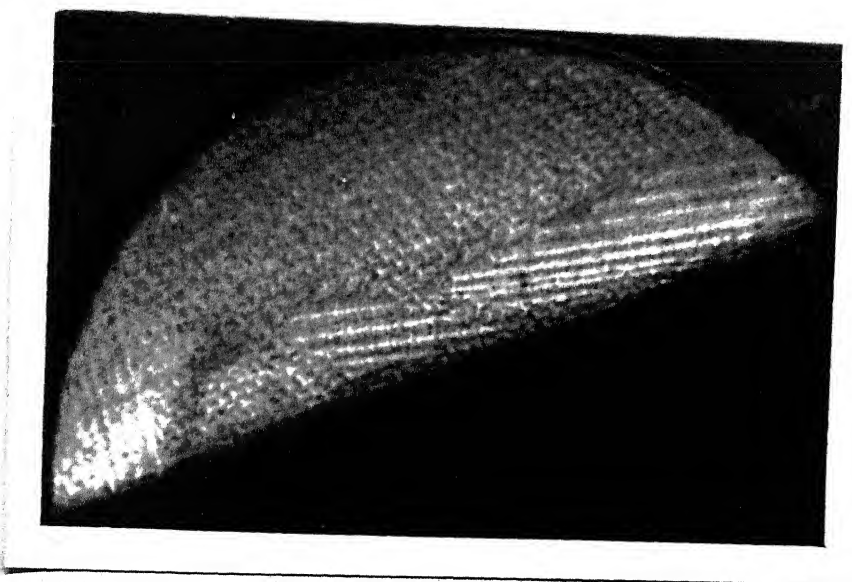


Figure 4.2: Corresponding Transverse section of Sn-2 wt% Bi alloy.
Magnification 9.5x.

The primary dendrite plates appear as relatively white bands separated by dark etching interdendritic regions. The apparent primary dendrite spacing is the distance between the centers of two consecutive white bands. From the apparent primary dendrite spacing, the true primary dendrite spacing is calculated. The true dendrite spacing is calculated using the angles that the traces of dendrites make in longitudinal and transverse section as explained in Appendix C.

The true primary dendrite spacing (PDS) has been plotted against distance from the starting position of the solid/liquid interface. The starting position of the solid/liquid interface is the position where the solid/liquid interface was in dynamic equilibrium in the ingot before the directional solidification was started. Typically, the starting position of solid/liquid interface was 4-5 cm above the bottom of the ingot. The starting position of solid/liquid interface is shown in Figure 4.3 for a Sn-2 wt% Bi alloy.

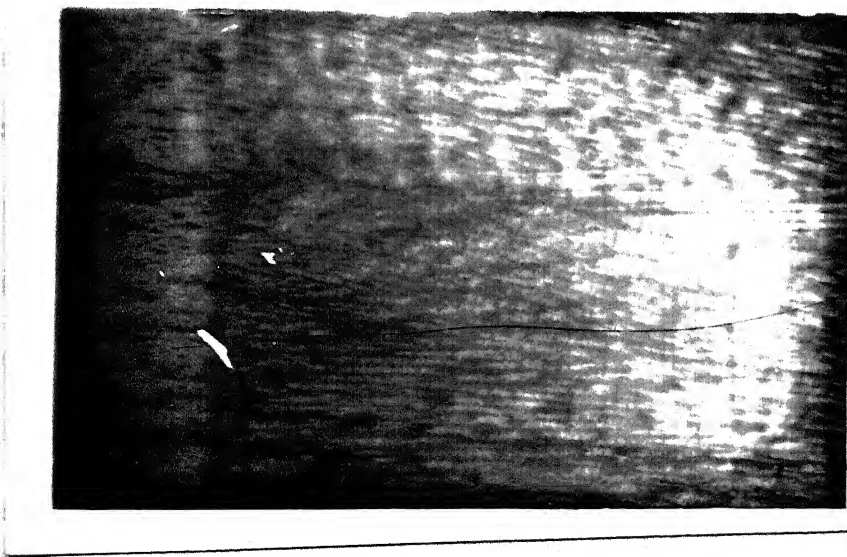


Figure 4.3: Starting position of solid/liquid interface for a Sn-2 wt% Bi alloy

Magnification 6x

The PDS for the two ingots Sn-2 wt% and Sn-4 wt% Bi are given in Figure 4.4 and Figure 4.5, respectively. The sketch of each ingot has also been drawn on the plots. The hashed portions on the sketch of the ingot indicate the loss of ingot during cutting, grinding and polishing. The downward arrow marks on the x-axis indicate the changes in freezing rates as calculated from the cathetometer readings of the movement of the furnace. Thus the arrows indicate points where a change in the rate of furnace movement was effected by changing the setting in the controller of the driving motor. The vertical solid lines on the graph have been drawn at the points where the PDS begins to respond to the changed freezing rate (the rate at which the solid/liquid interface moves) as a result of a change in the rate of furnace movement. The fact that the arrow marks and the vertical lines are at different locations indicates that the solid/liquid interface takes sometime to respond to a change in the furnace movement rate.

As seen from the Figures 4.4 and 4.5 there is always a mismatch between the imposed change in freezing rate (by changing the rate of movement of the furnace relative to the specimen) and the actual change in the freezing i.e. the rate of movement of the solid/liquid interface. The solid/liquid interface is assumed to be nominally planar for the two runs. The photograph in Figure 4.3 shows the microstructure around the solid/liquid interface. The solid/liquid interface appears planar and normal to the growth direction. From the plots in Figures 4.4 and 4.5 it is seen that the solid/liquid interface during the period of directional solidification differs markedly from the furnace speed.

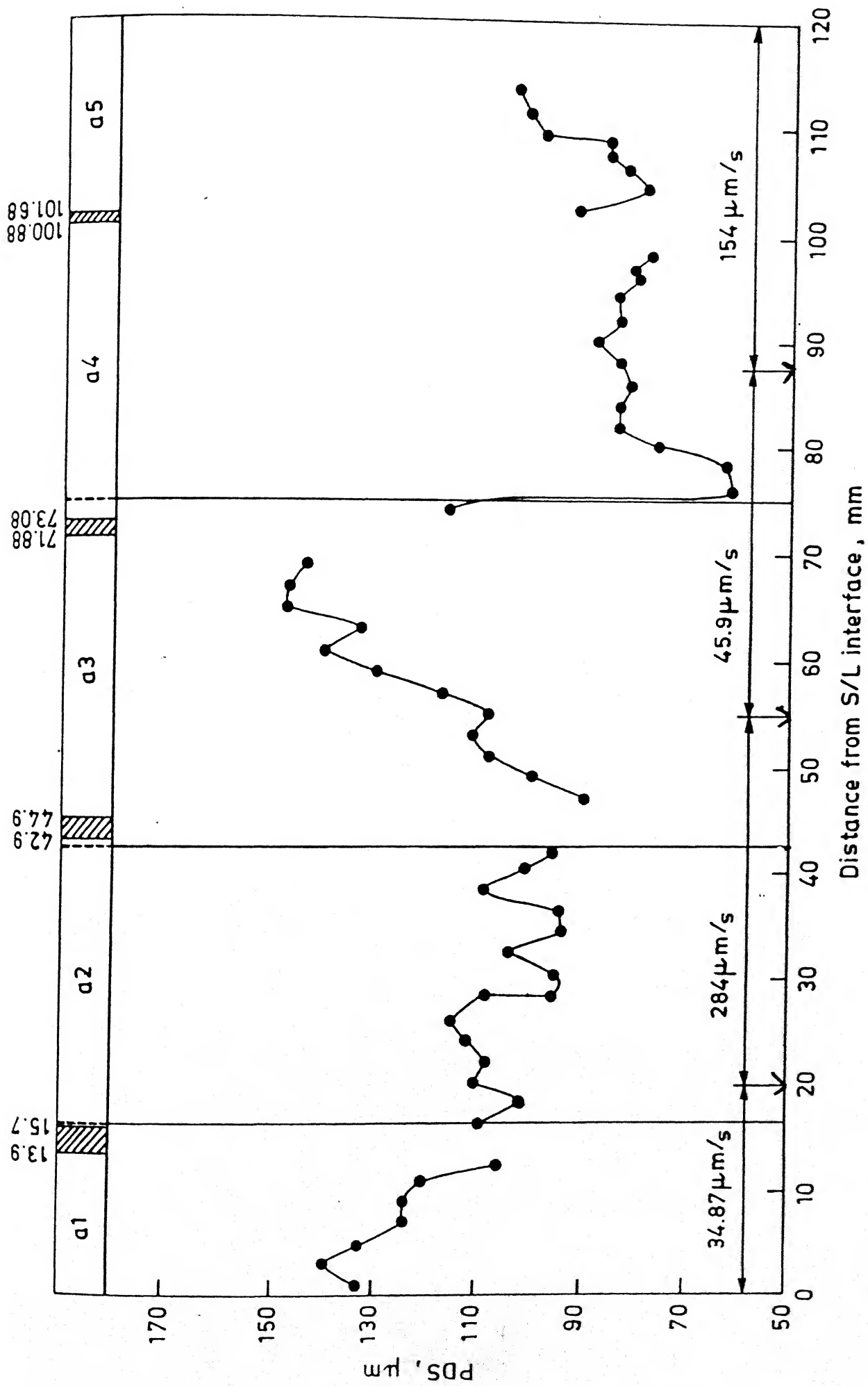


Figure 4.4: Primary dendrite spacing with freezing rate for Sn-2 wt% Bi alloy.

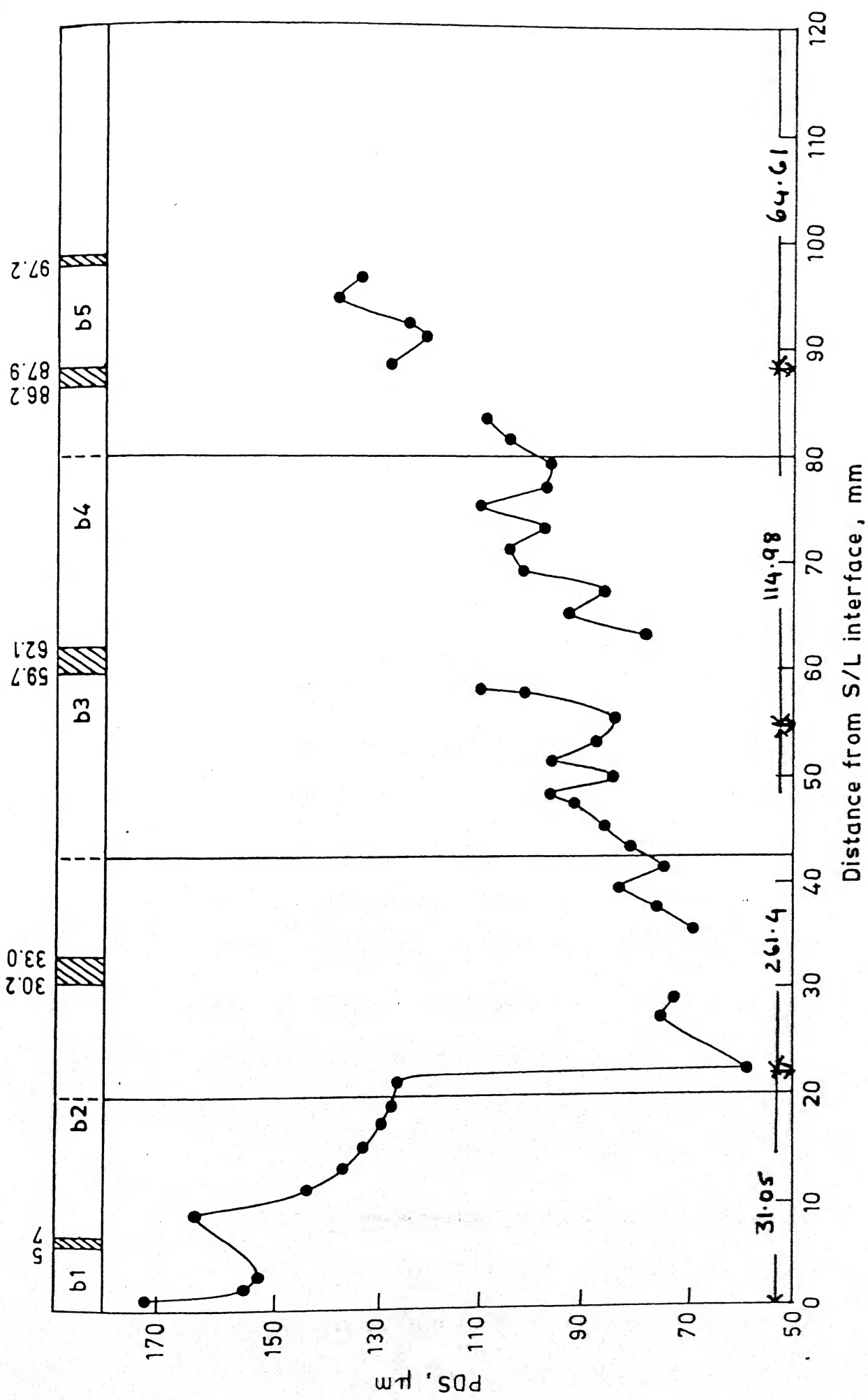


Figure 4.5: Primary dendrite spacing with freezing rate for Sn-4 wt% Bi alloy.

Initially it is assumed that the solid/liquid interface moved with the same speed as that of the furnace speed by comparing the present set-up with that of the other set-up [23]. But this is during steady state solidification only.

Figure 4.4 for 2 wt% Bi alloy shows that the distance travelled by the solid/liquid interface when there was an increase in freezing rate, is smaller than that travelled by the furnace. When the furnace speed is increased from 43 $\mu\text{m/s}$ to 284 $\mu\text{m/s}$, the distance travelled by the interface is only 25.5 mm while the distance travelled by the furnace is 35 mm (a difference of 27 percent). The actual freezing rate change of solid/liquid interface always occurs after the change of speed imposed on the furnace. On the other hand, when the furnace speed is suddenly decreased to a slower speed, the distance travelled by the interface will be larger than that travelled by the furnace. This is, because the solid/liquid interface gradually attains the newly imposed slower speed. When the furnace speed is decreased from 284 $\mu\text{m/s}$ to 45.9 $\mu\text{m/s}$, the distance travelled by the solid/liquid interface is 32.5 mm, whereas the furnace travelled only 31.5 mm (a difference of about 3 percent only). Thus, when the furnace speed is reduced, the solid/liquid interface travels larger a distance than that travelled by furnace at this reduced speed. Conversely, when the furnace speed is increased, the solid/liquid interface travels lesser distance than that travelled by the furnace at this increased speed.

Figure 4.5 for 4 wt% Bi alloy shows that when the furnace speed is increased from 31.05 $\mu\text{m/s}$ to 261.4 $\mu\text{m/s}$, the distance travelled by the interface is only 22 mm, while the furnace actually travelled 33 mm (a difference of 33%). The interface lags

by 10 mm. When the furnace speed was suddenly decreased to 114.98 $\mu\text{m/s}$ from 261.4 $\mu\text{m/s}$ the distance travelled by the interface is 37.5 mm while the furnace moved only 33 mm (a difference of about 14%). Thus it is seen that the distance travelled by the solid/liquid interface during a slower speed (when reduced from a faster speed) is larger than that travelled by the furnace. Conversely, if the furnace speed is increased from a slower speed, the distance travelled by solid/liquid interface is smaller than that travelled by the furnace.

A similar behaviour of the solid/liquid interface movement w.r.t. the movement of the furnace has also been reported by Clyne [1] in a similar experiment. Commercial purity Aluminum was used for directional solidification by Clyne. They have reported that the steady state growth rate of the solid/liquid interface differed from that of the furnace by upto 30%. It was observed that the divergence between the velocities of growth front and furnace tends to become smaller for higher traverse speeds. They have employed same furnace speed through out a run and have reported that the length solidified was smaller than the distance traversed by the furnace at higher velocities, while the length solidified was greater than the distance covered by the furnace at slower velocities.

On the other hand Sarreal et.al. [20] have reported that the variation in the velocities of interface and crucible differed by upto $\pm 10\%$ for crucible velocities of 0.001 to 1 cm/s for Al-Cu alloys.

The response of solid/liquid interface with the movement of the furnace was also reported by Fu et.al. [11]. It was found that when the furnace movement rate was increased, the solid/liquid interface travels smaller distance than the distance travelled by the furnace. They have presented a numerical solutions and have found that with a step function increase in furnace movement rate it takes some time for the interface to reach a new equilibrium position.

It is seen from Figures 4.4 and 4.5 that the primary dendrite. Spacing is larger with a lower freezing rate and is smaller at higher freezing rates. While, when the furnace traverse rate is changed abruptly to a new rate, the PDS appears to change gradually. The freezing rate was either made to decrease or increase abruptly after the ingot had solidified for a certain length. Figure 4.6 shows the immediate change in PDS when the freezing rate was suddenly increased from $45.9 \mu\text{m/s}$ to $154 \mu\text{m/s}$ for a 2wt% Bi alloy.

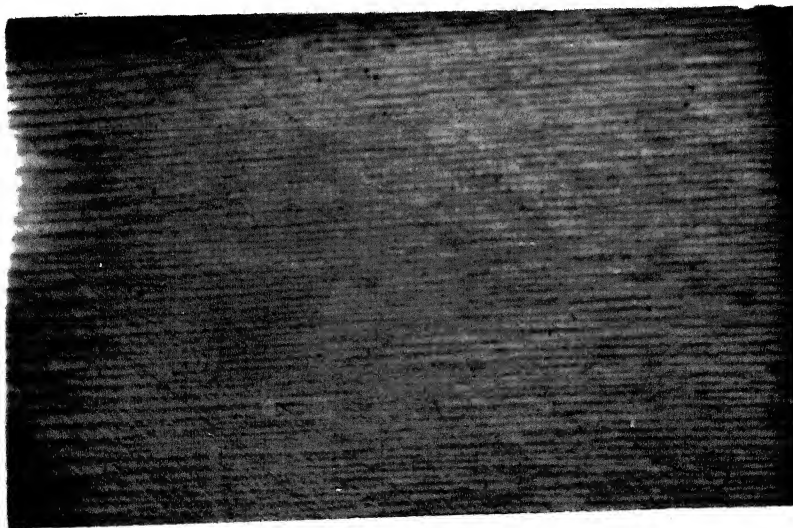


Figure 4.6: Immediate increase in PDS with increase in Freezing rate.

Magnification 6x

The primary dendrite spacing is seen to decrease with an increase in freezing rate and then reaches a new steady state value. Similarly if the freezing rate is decreased, the primary dendrite spacing increases, and then reaches a new steady state value. Figures 4.4 and 4.5 do not show a regular and continuous change in PDS with freezing rate because of the nature of measurements involved and normal local fluctuations involved. But the overall trend of the curve shows an increasing or decreasing PDS with change in freezing rates. It is assumed that PDS reaches a steady state value as it continues to solidify at the same freezing rate.

The steady state primary dendrite spacing value for each freezing rate is given in tabular form in Table 4.1. The values are then plotted in Figure 4.7a and 4.7b on log-log graph. The Figure 4.7 shows the results of two earlier references also. The data points exhibited a linear fit with a negative slope of 0.314 in case of 2 wt% Bi and 0.33 in case of 4 wt% Bi for the present work. The negative slopes obtained earlier by ref. [23] was 0.395 for 2 wt% Bi and 0.448 for 4 wt% Bi. The negative slope obtained by ref.[25] was 0.366 for 2 wt% Bi. The experimentally determined values of the exponent 'm' compare well with those of other workers on the Sn-Bi system and also with the theoretically proposed value of -1/3 to -1/2 by different workers.

Table 4.1: Steady state PDS values.

Composition (wt% Bi)	Freezing rate ($\mu\text{m/s}$)	PDS (μm)
2	34.87	109.3
2	284	94.63
2	45.9	145.38
2	154	101.59
4	31.05	127.79
4	261.4	75.73
4	114.98	96.74
4	64.61	134.651

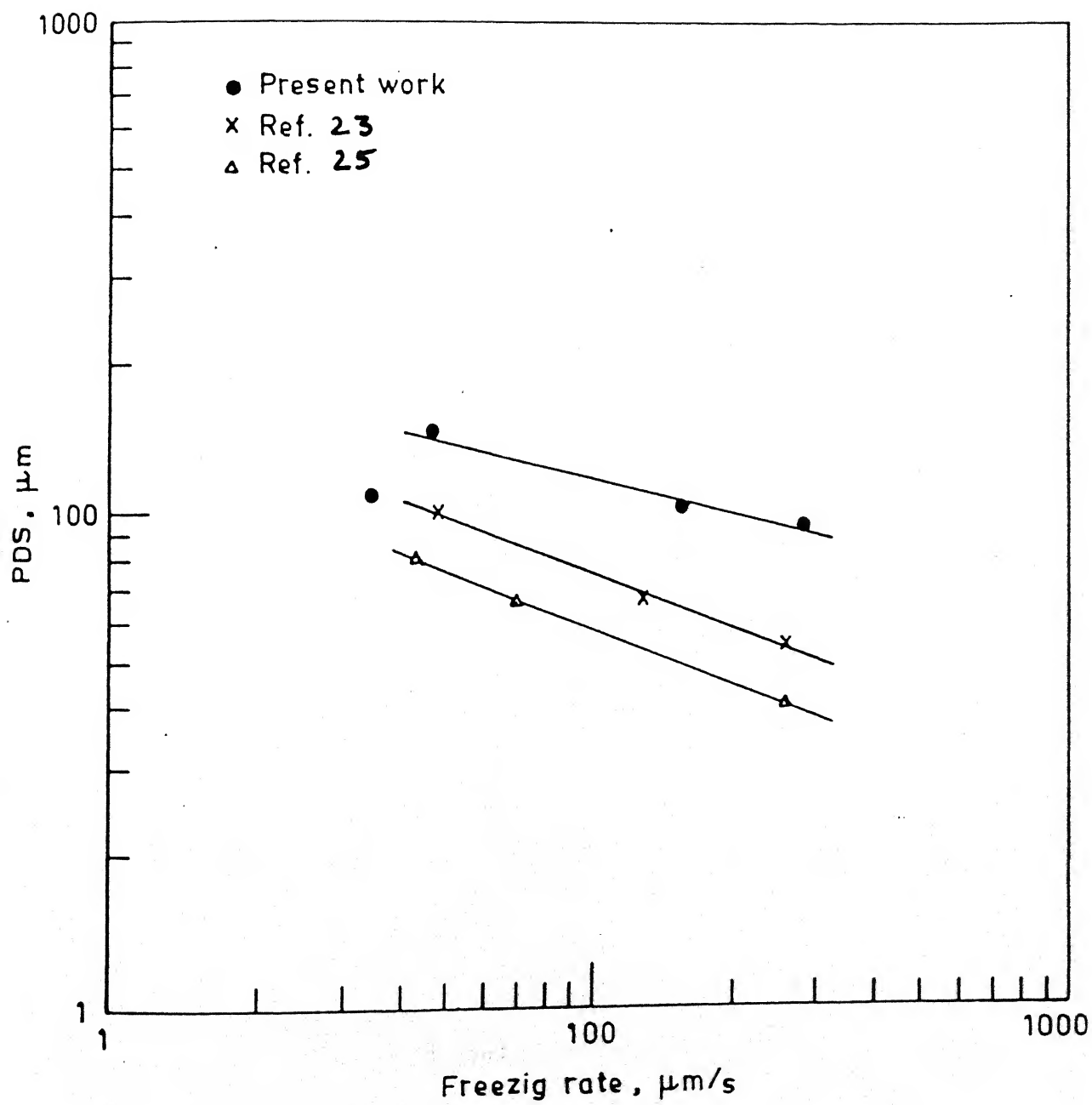


Figure 4.7a: Steady state PDS values with Freezing rates 2 wt% Bi alloy.

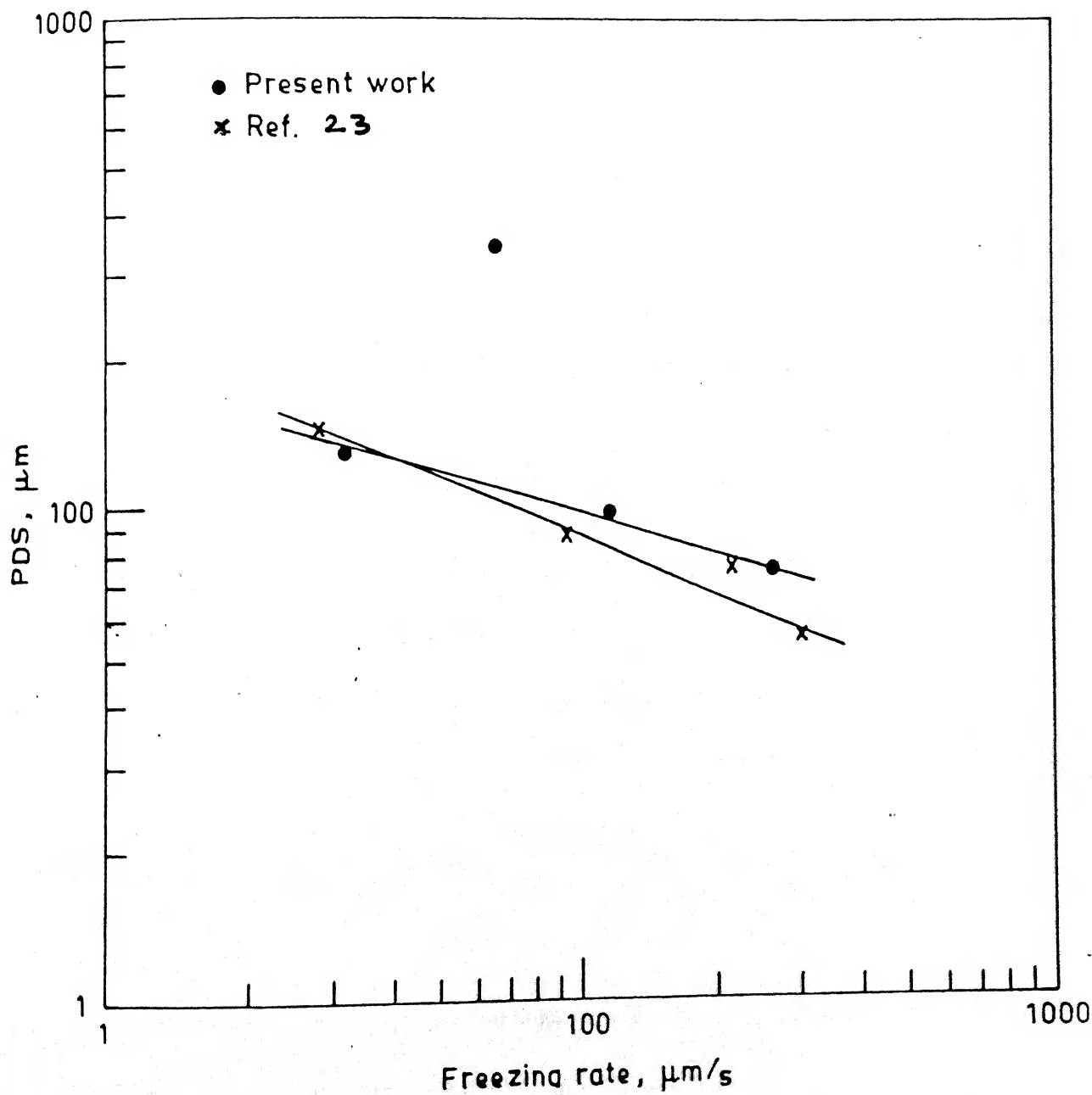


Figure 4.7b: Steady state PDS values with Freezing rates for 4 wt% Bi alloy.

4.2 Mechanism of Adjustment of Primary Dendrite Spacing to Freezing Rate Change

As suggested by Flemmings [14] one of the mechanism for spacing adjustment is a tertiary becoming primary as shown in Figure 2.2. In the present investigation it is found that this mechanism is operating as seen in Figures 4.8, 4.9, 4.10. Figure 4.8 shows the primary arm becoming a tertiary arm (marked as '1' in Figure 4.8) and the tertiary arm again becoming a primary arm (marked as '2' in Figure 4.8). Figure 4.9 shows the primary arm becoming a tertiary arm (marked by arrows in Figure 4.9). Figure 4.10 shows a primary arm becoming a tertiary arm at higher magnification (marked by arrow). In these figures, the coarser (thicker) dendrites on the left were growing at a freezing rate of $45.9 \mu\text{m/s}$ in the 2 wt% Bi alloy. The new freezing rate imposed abruptly was $154 \mu\text{m/s}$. The dendrite spacing must decrease since the local solidification times decrease and so the diffusion distances for the solute also decrease. This decrease in primary dendrite spacing occurs by new primary dendrites growing from the tertiary arms of the existing primary dendrites. It was also observed that once a tertiary becomes a primary it behaves as a new primary to the extent that new primaries grow from its tertiary arms as shown in Figure 4.8.

4.3 Solute Redistribution

Electron Probe Micro Analyzer was used to determine the variation of Bi concentration from the centre of a primary dendrite to the interdendritic region. The plots of point scans taken approximately perpendicular to the dendrite growth direction across two dendrites on sample a2 (2 wt% Bi) and sample b2 (4 wt% Bi) is shown in Figure 4.11 and 4.12 respectively.

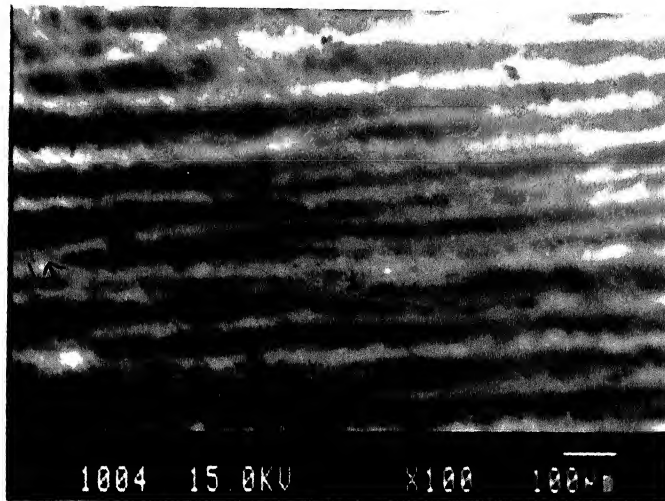


Figure 4.8: Photograph showing the Tertiary→Primary change.

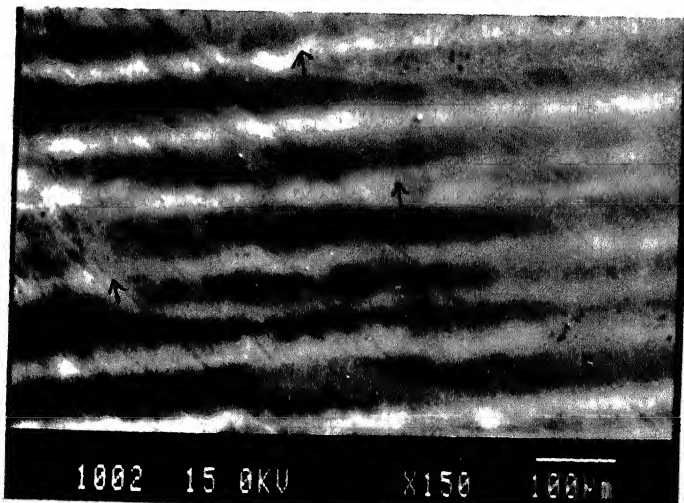


Figure 4.9: Photograph showing the Tertiary becoming Primary

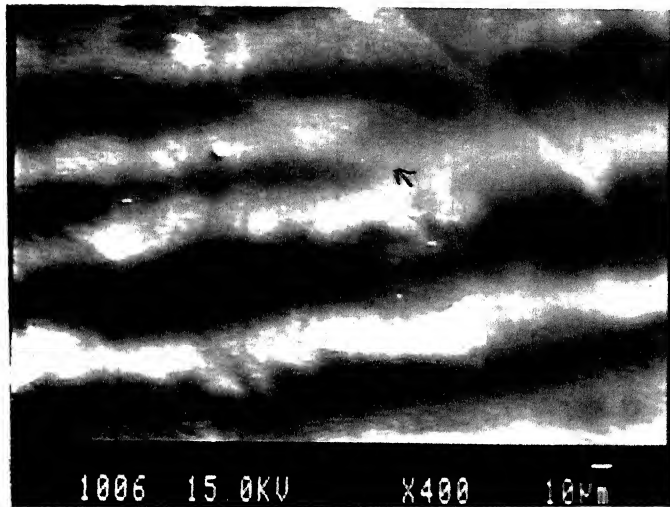


Figure 4.10: Photograph showing the ^{Tertiary → Primary} at high magnification.

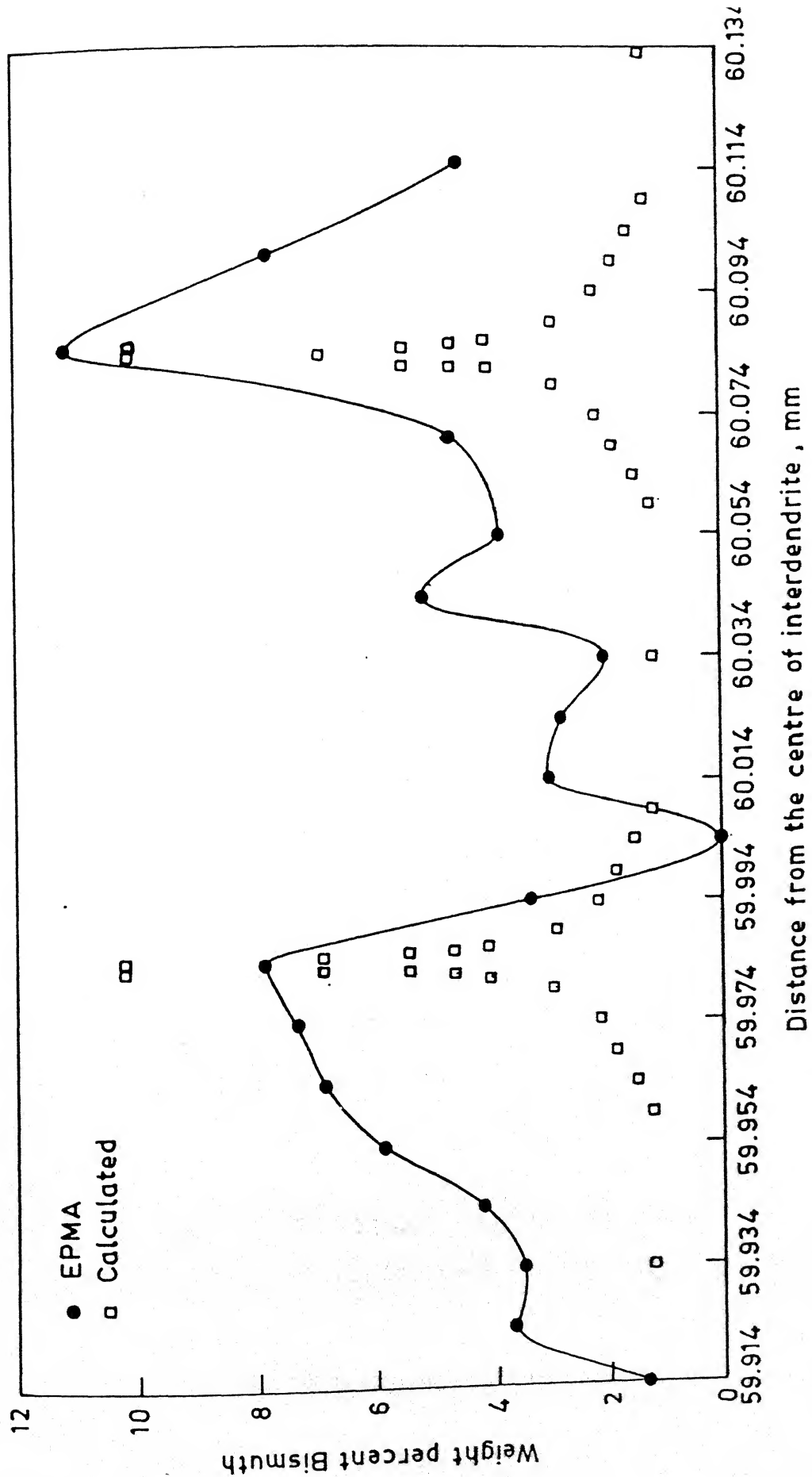


Figure 4.11: Point scan across two dendrites on sample a2 (2 wt% Bi).

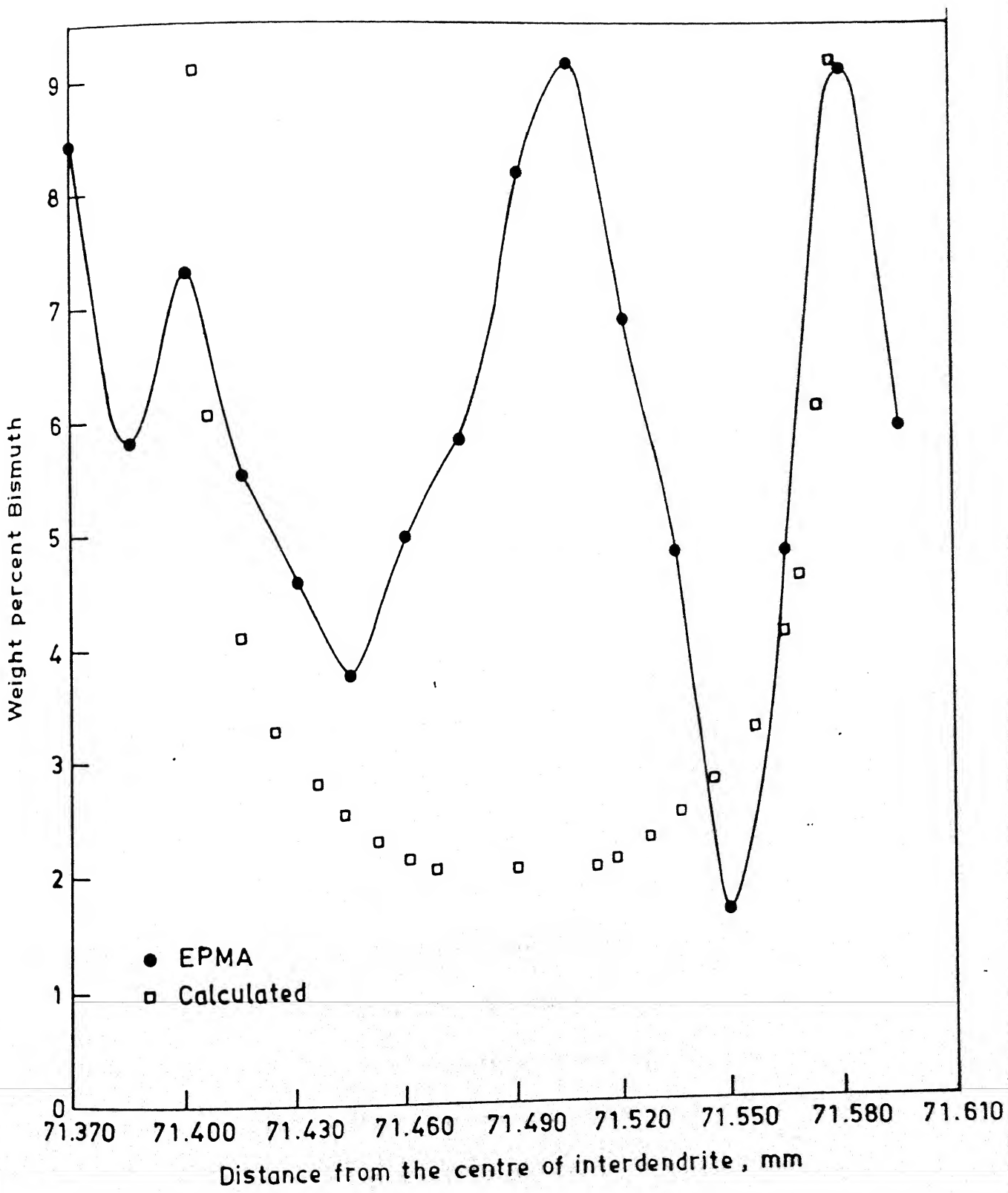


Figure 4.12: Point scan across two dendrites on sample b2 (4 wt% Bi).

The two peaks in Figure 4.11 corresponds to the two interdendritic regions which appear as regions which appear as dark bands in the photograph taken in the EPMA of this area. Figure 3.18a and 3.18b shows the points between which the Bi concentration was determined at intervals of 10-15 μ m for 2 wt% and 4 wt% Bi. From Figure 4.11 it is seen that there is a considerable change in concentration of Bi from dendritic centers to interdendritic regions. The maximum concentration of Bi in the interdendritic region goes upto 11.1 wt% as determined in the EPMA. At the center of the dendrite, the concentration of Bi is expected to be 1.28 wt%, from theoretical considerations (see Appendix F). However, a low of 0 wt% Bi has been obtained at the center of the dendrite by the EPMA. The EPMA determination appears to be in error since the concentration of Bi is quite low. The distance between the two peaks corresponds to the primary dendrite spacing at that point, which is 6.9 cm from the bottom of the ingot. The PDS as measured directly with the micrometer eyepiece was 98.6 μ m at this point. The distance between the two peaks, which corresponds to the primary dendrite spacing obtained from Bi concentration plots, is approximately 100 μ m. Thus, there is excellent match between the direct measurement and the width of PDS obtained from Bi Concentration distribution. A theoretical expression for solute redistribution for dendritic solidification has been proposed by Sarreal et.al. [20]. Solute concentrations have been calculated using this expression for the present system. These calculated concentrations have been superimposed on the plots based on EPMA determination in Figure 4.11. The two match very well given the fact that the theoretically calculated plots are based on several idealizations of the system. The equation and data for the calculation of concentration for solute in the solid (C^*) at various fractions solidified are given in Appendix F (Table F.1). The calculated C^* , vs

f_s curves represents one half of the dendrite spacing (from the centre of the dendrite ($f_s = 0$) to the centre of interdendritic region ($f_s \approx 1$)).

Similar analysis was performed on sample b2 (4 wt% Bi) as shown in Figure 4.12. The point where the Bismuth redistribution was measured in the EPMA was 5.85 cm from the bottom of the ingot. The points marked on Figure 3.18b are those between which the Bi concentration was measured at 10-15 μm intervals. The PDS spacing as measured using the micrometer eyepiece is 139 μm . The distance between the two peaks in Figure 4.12 is approximately 120 μm based on EPMA determination. This difference between the PDS determined directly with the micrometer and that from EPMA may be due to local variation in dendrite spacing in the microstructure. Figure 4.12 shows the similarity between the Bi concentration from EPMA and that calculated on theoretical basis. Concentration of Bi at the center of the dendrite was 2.05 wt% . This compares well with the minimum concentration of 1.7 wt% Bi determined by EPMA. The equation and data for the calculation of concentration of solute in the solid (C_s^*) and the fraction solidified (f_s) is given in Appendix F (Table F.2).

4.4 Effect of Abrupt Change in Freezing Rate on Solute Concentration in the Liquid Ahead of the Dendrite Tips

Based on theoretical considerations, the solute concentration variation in the mushy zone and in the liquid in front of the growing dendrites is expected to be as shown in Figure 2.3. Thus there is a boundary layer of liquid, which is enriched with respect to the solute, and the concentration of the solute varies from C_i at the growing dendrite tips to C_0 (the average alloy composition) far away into the liquid. Kurz et.al.

[26] have proposed a simple method to compute the excess solute contained in this enriched layer (see Appendix G). It turns out that the solute concentration in the liquid at the dendrite tip (C_l) is a function of freezing rate besides other parameters. Thus for the same alloy composition C_0 expected to be different at different freezing rates. And therefore the amount of excess solute in the boundary layer will also be different. An interesting result of an abrupt increase in freezing rate is that C_l as well as excess amount of solute decrease, compared to what they were at slower freezing rates. This means that the difference between the two amounts of solute will be rejected out of the solute enriched layer as this boundary layer adjusts to the new increased freezing rate. Appendix G shows the calculated values of C_l and the excess solute in the boundary layer for the 2 wt% Bi alloy for 45.9 $\mu\text{m/s}$ and 154 $\mu\text{m/s}$ freezing rates. The calculations show that about 75 percent of solute contained in the enriched boundary layer at a freezing rate of 45.9 $\mu\text{m/s}$ must be rejected when the freezing rate is abruptly increased to 154 $\mu\text{m/s}$.

Smith et.al. [27] have carried out a theoretical analysis for the rejection of solute due to abrupt change in freezing rate for the case of plane front directional solidification. Assuming that the same analysis holds in the present case, the rejected amount of excess solute is expected to increase the solute concentration of the solid as shown in Figure 4.13. This curve is reproduced from Smith et.al. for an increase in freezing rate by 5 times and for a system with solute partitioning coefficient (K) as 0.5. For the present system case under consideration the increase in freezing rate was 3.3 times and the value of K for Sn-Bi alloy is 0.37. In order to check whether such a solute enriched 'band' exists in the solid at the point of abrupt change in freezing rate

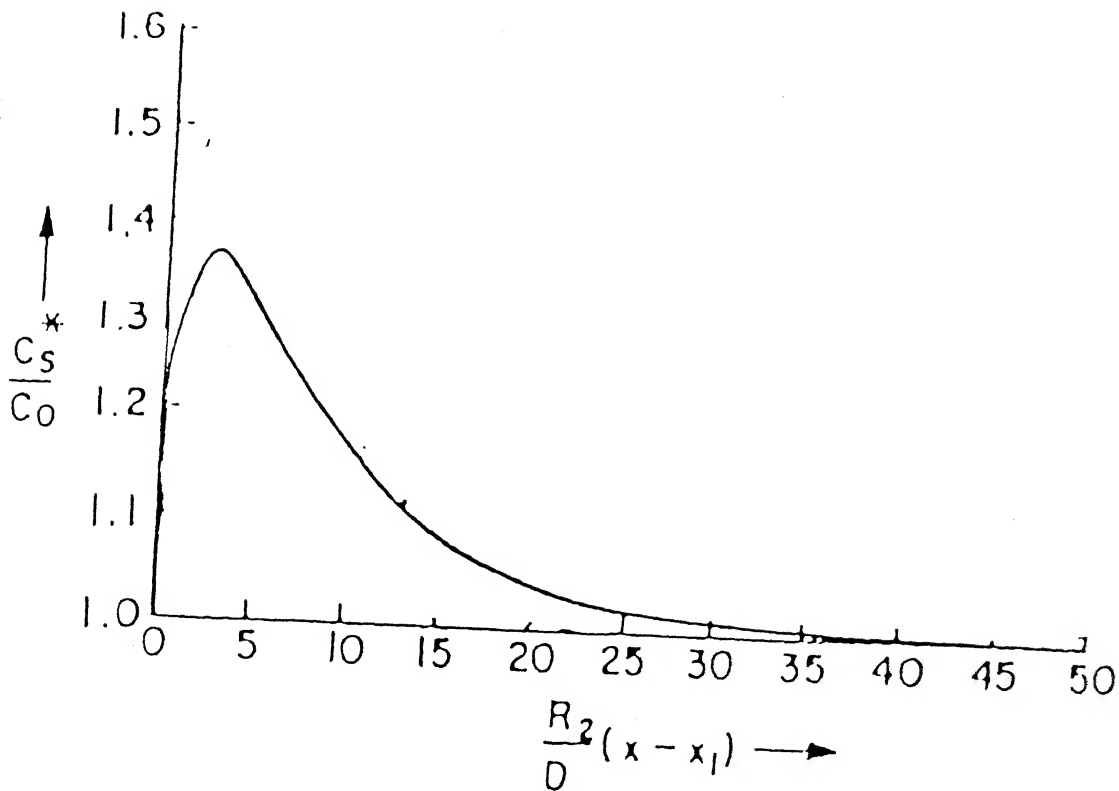


Figure 4.13: Transient solute distribution in solid resulting from an instantaneous change in growth velocity from R_1 to R_2 at location x_1 (after Smith et.al. [27]).

an EPMA scan was taken along the interdendritic region on both sides of the point of change in freezing rate. The dendrite was chosen which was growing continuously in both regions of the freezing rate. Figure 4.14 shows the Bi concentration variation with distance near the interdendritic region over a total length of 1700 μm (400 μm on the slower freezing rate side and 1300 μm on the faster freezing rate side. The arrow indicates approximate position of the point where the rate of movement of solid/liquid interface changed abruptly. The theoretical calculations based on Smith's analysis indicates that this width of the solute enriched 'band' will be approximately 500 μm from the point of abrupt change in freezing rate. The EPMA determination of Bi concentrations were made at 50 μ intervals as seen in Figure 4.14.

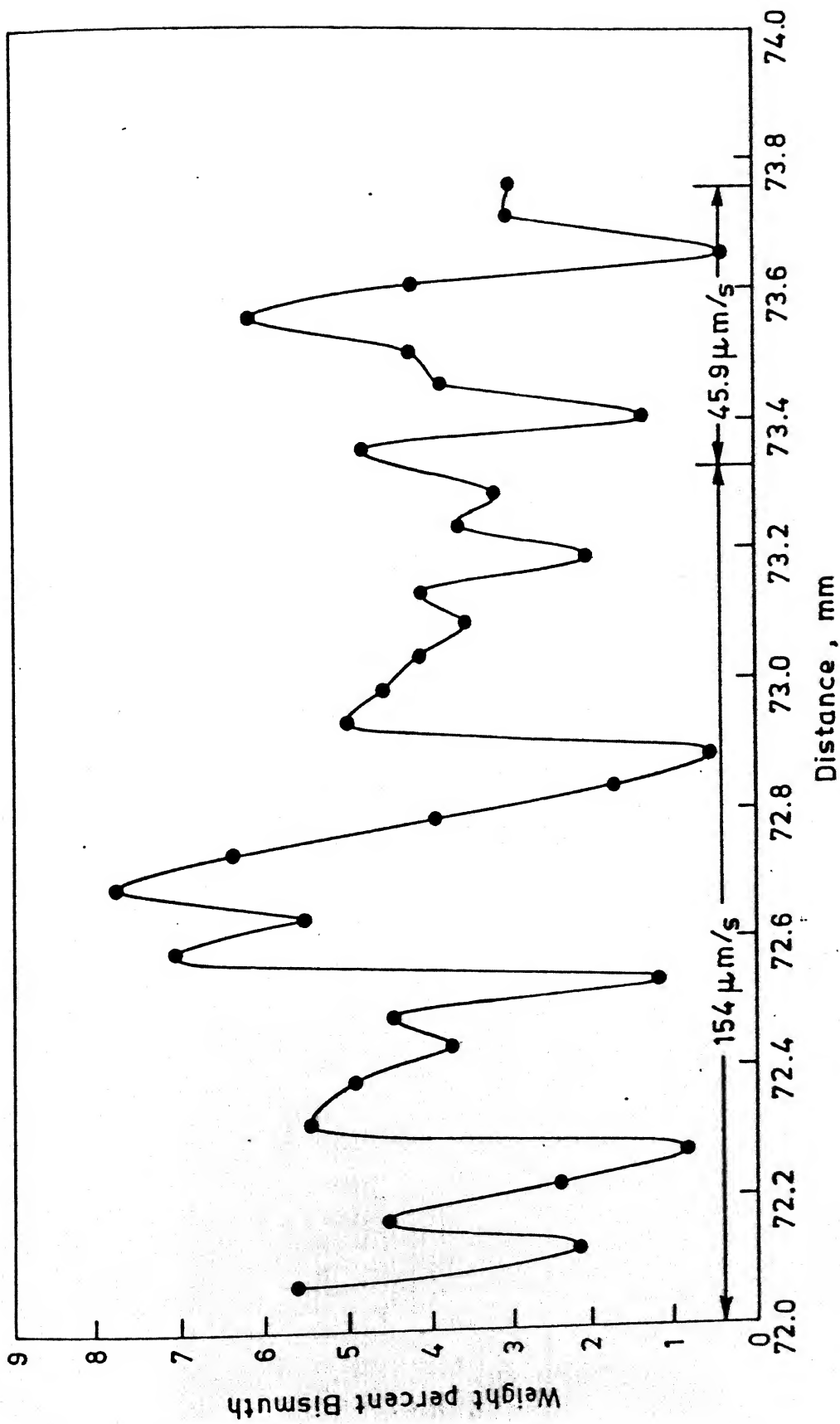


Figure 4.14: Bi concentration variation with distance near the interdendritic region.

It is difficult to say from the plot in Figure 4.14 whether a solute enriched 'band' is there or not. If it is there, it appears to have been marked by the fluctuations in the Bi concentration, owing to other reasons. Further, the theoretical calculations of the solute enriched 'band' are based on the plane front solidification and not for dendritic solidification. At present, an analysis similar to that by Smith et.al. [27] is not available for dendritic solidification. It is possible that the solute redistributes itself very differently than in the case of plane front solidification when an abrupt change in freezing rate is imposed. Figures 4.15a and b show the dendrite over which point analysis was made. The electron beam has left marks at the points of analysis and they are visible in Figures 4.15 a and b.



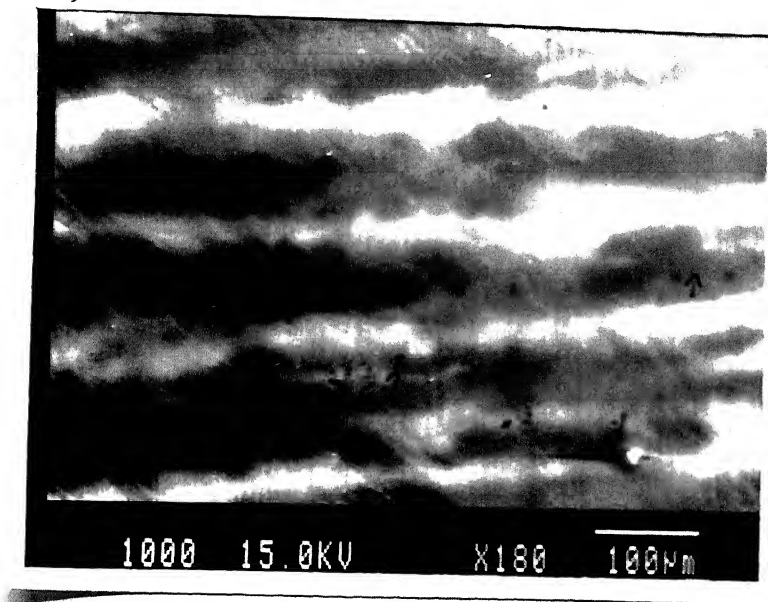


Figure 4.15: Point analysis near the interdendritic region for sample a4 (2 wt% Bi alloy).

4.5 Calculation of Heat Transfer Coefficient

The temperatures determined at point below solid/liquid interface in the solid region was used for determination of heat transfer coefficient. The rate at which heat was removed by spray water was calculated from the rise in temperature of spray coming out of the chill spray. The temperature of the spray water rises is a result of the heat transfer from the outside surface of the glass crucible where the water spray is hitting it and also the portion below it over which the spray water flows down. The details of the calculations are given in Appendix H. The average heat transfer coefficient for the vycor crucible is found to be $0.0314 \text{ cal/cm}^2/^{\circ}\text{C/sec}$. Several empirical relations are available in the literature for the calculation of heat transfer coefficient one such relation by Kern [21] has been used to calculate the heat transfer

coefficient as given in Appendix H. The value calculated from this empirical relation comes out to be $0.012 \text{ cal/cm}^2/^{\circ}\text{C/sec}$. The above two values of heat transfer coefficient are comparable but obviously different.

Chapter 5

Conclusions

Directional solidification has been successfully accomplished in Sn-Bi alloy system over a wide range of growth rates (approximately 30-300 $\mu\text{m/s}$) at a constant temperature gradient in the liquid at the solid/liquid interface. Investigation has been carried out for 2 wt% and 4 wt% Bi alloys in Sn.

1. The solid/liquid interface movement responds to the rate of furnace movement with some time lag. Experimentally it is seen that the distance travelled by the solid/liquid interface during a slower speed (when reduced from a faster speed) is larger than that travelled by the furnace. Conversely, if the furnace speed is increased from a slower speed, the distance travelled by the solid/liquid interface is smaller than that travelled by the furnace.
2. The primary dendrite spacing seems to have the following correlation with the freezing rate (R),

$$\lambda \propto R^m$$

$$\text{or } \lambda = K R^m$$

where, K is a constant.

The value of ' m ' is found to be -0.314 for 2 wt% Bi alloy and -0.33 for 4 wt% Bi alloy.

3. It was observed that when there is an increase in freezing rate, the decrease in primary dendrite spacing occurs by new primary dendrites growing from the tertiary arms of the existing primary dendrites.

4. Bismuth concentration was measured from the center of a dendrite to the interdendritic region (normal to the direction of growth of the dendrite). The Bismuth concentration using EPMA and theoretically calculated Bismuth concentration were found to match reasonably well.
5. The heat transfer coefficient calculated from the experimental data is found to be 0.1314×10^4 watts/m²/K for the portion of the crucible over which spray water is flowing.

References

- [1] T.W. Clyne in "Heat Flow in Controlled Directional Solidification of Metals-I. Experimental Investigation", *Journal of Crystal Growth* 50 (1980), 684-690.
- [2] Ta-Wei Fu and William R. Wilcox in "Rate Change Transients in Bridgman-Stockberger Growth of Mn Bi-Bi eutectic", *Journal of Crystal Growth* 57 (1982) 189-193.
- [3] C.A. Wang and A.F. Witt in "Analysis of Crystal Growth Characteristics in a Conventional Vertical Bridgman Configuration", *Journal of Crystal Growth* 66 (1984) 299-308.
- [4] Sanghamitra Sen and William R. Wilcox "Influence of Crucible on Interface Shape, Position and Sensitivity in the Vertical Bridgman-Stockbarger Technique", *Journal of Crystal Growth* 28 (1975), 36-40.
- [5] Ta-Wei Fu and William R. Wilcox in "Influence of Insulation on Stability of Interface Shape and Position in the Vertical Bridgman-Stockbarger Technique", *Journal of Crystal Growth* 48 (1980), 416-424.
- [6] T.W. Clyne in "Heat Flow in Controlled Directional Solidification of Metals II. Mathematical Model", *Journal of Crystal Growth* 50 (1980), 684-690.
- [7] T. Jasinski and R.J. Naumann in "One-Dimensional Thermal Modelling of Vertical Bridgman-Type Crystal Growth", *Journal of Crystal Growth* 66 (1984), 469-471.
- [8] R.J. Naumann in "An Analytical Approach to Thermal Modelling of Bridgman-Type of Crystal Growth-I. One - Dimensional Analysis", *Journal of Crystal Growth* 58 (1982), 554-568.
- [9] T. Jasinski, W.M. Rohsenow, A.F. Witt in "Heat Transfer Analysis of the Bridgman-Stockbarger Configuration for Crystal Growth-I. Analytical Treatment of the Axial Temperature Profile", *Journal of Crystal Growth* 61 (1983) 339-354.
- [10] R.J. Naumann in "An Analytical Approach to Thermal Modelling of Bridgman-Type Crystal Growth-II. Two Dimensional Analysis", *Journal of Crystal Growth* 58 (1982), 569-584.
- [11] Ta-wei Fu and William R. Wilcox in "Programmed and Oscillatory Motion in Bridgman-Stockbarger Growth", *Journal of Crystal Growth* 57 (1982), 91-93.

- [12] R. Trivedi, J.A. Sekhar, J. Majumdar, "Principles of Solidification and Materials Processing", Vol.I, 1985, pg.38.
- [13] Bruce Chalmers, "Principles of Solidification", 1964, Pub. John Willey and Sons, pp.94.
- [14] M.C. Flemmings, "Solidification Processing", 1974, Pub. McGraw-Hill Series, pp.148.
- [15] V. Laxmanan in "Dendritic Solidification-II. A Model for Dendritic Growth under an Imposed Thermal Gradient", Actametall., Vol.33, No.6, pp.1037-1049, 1985.
- [16] J.D. Hunt in "Proceedings of an International Conference on Solidification, University of Sheffield on 18-21, July 1977, Pub.Metal Society, London (1979), pp.3-9.
- [17] Dominique Bouchard and John S. Kirkaldy in "Prediction of Dendrite Arm Spacings in Unsteady and Steady State Heat Flow of Unidirectionally Solidified Binary Alloys", Metallurgical and Materials Transactions B, Vol.28B, August 1997, pp.651.
- [18] M.A. Chopra and S.N. Tewari in "Growth Speed Dependence of Primary arm Spacing in Directionally Solidified Pb-10Wt% Sn", Metallurgical Transactions A, Vol.22A, October 1991, pp.2467.
- [19] S. Ganesan and D.R. Poirier in "Solute Redistribution in Dendritic Solidification with Diffusion in the Solid", Journal of Crystal Growth 97 (1989), pp. 851-859.
- [20] J.A. Sarreal and G.J. Abbaschian in "The Effect of Solidification Rate on Microsegregation", Metallurgical Transactions A, Volume 17A, November 1986, pp.2063.
- [21] Kern D.Q., "Process Heat Transfer", 1st Edition, Pub. McGraw-Hill Series, 1950.
- [22] Alloy Phase Diagrams, ASM Handbook, 1992.
- [23] Ravikumar, M.Tech. Thesis (1991), IIT Kanpur.
- [24] V. Bansal in "A Procedure to Determine True Lamellar Dendrite Spacing", Journal of Materials Science Letters 8 (1989), 451-452.
- [25] Das Niranjana, M.Tech.Thesis (1990), I.I.T. Kanpur.

- [26] Kurz, W.; Fisher, D.J., "Fundamentals of Solidification", 3rd ed. Transtech Publications, 1992.
- [27] V.G. Smith, W.A. Tiller and J.W. Rutter in "A Mathematical Analysis of Solute Redistribution During Solidification", Canadian Journal of Physics, Vol.33, pp.723-745.

Appendix A

Steady state temperature profile along the length of the furnace at different variac settings.

Table : A.1
Variac Setting 92V

S.No.	Distance of t.c. tip from top of fce tube (cm)	EMF (mv)	Temperature (with R.T. correction °C)
1	40.5	11.0	310
2	39.8	11.2	315
3	38.8	11.45	320
4	38.3	11.5	322
5	37.8	11.65	325
6	37.3	11.7	327
7	36.8	11.75	328
8	36.3	11.8	329
9	35.8	11.9	332
10	35.3	11.9	332
11	34.8	12.02	335
12	34.3	12.10	336
13	33.8	12.15	337
14	33.3	12.2	339
15	32.8	12.25	340
16	32.3	12.3	341
17	31.8	12.3	341
18	31.3	12.3	341
19	30.8	12.35	342
20	30.3	12.40	344
21	29.8	12.42	345
22	29.4	12.42	345
23	28.8	12.45	345
24	28.3	12.55	347
25	27.8	12.65	348
26	27.3	12.65	349
27	27.1	12.65	349
28	26.9	12.65	349
29	26.4	12.65	349
30	25.9	12.70	351
31	25.4	12.75	352
32	24.9	12.75	352
33	24.4	12.70	351
34	23.9	12.65	349
35	23.4	12.60	348
36	22.9	12.60	348

37	22.4	12.50	346
38	21.9	12.45	345
39	21.4	12.35	342
40	20.9	12.2	339
41	20.4	12.05	335
42	19.9	11.9	332
43	19.4	11.8	329
44	18.9	11.7	327
45	18.4	11.5	322
46	17.9	11.4	319

Table : A.2
Variac Setting 100V

S.No.	Distance of t.c. tip from top of fce tube (cm)	EMF (mv)	Temperature (with R.T. correction °C)
1	40.5	13.7	374
2	39.8	13.9	379
3	38.8	14.1	383
4	38.3	14.15	384
5	37.8	14.15	384
6	37.3	14.2	386
7	36.8	14.3	388
8	36.3	14.3	388
9	35.8	14.4	391
10	35.3	14.45	392
11	34.8	14.5	393
12	34.3	14.52	393
13	33.8	14.6	395
14	33.3	14.6	395
15	32.8	14.62	395
16	32.3	14.65	396
17	31.8	14.65	396
18	31.3	14.67	396
19	30.8	14.67	396
20	30.3	14.7	398
21	29.8	14.7	398
22	29.4	14.75	399
23	28.8	14.8	400
24	28.3	14.8	400
25	27.8	14.85	401
26	27.3	14.9	403
27	27.1	14.9	403
28	26.9	14.95	403.5
29	26.2	14.95	403.5
30	25.9	15.00	405
31	25.4	14.85	401
32	24.9	14.80	400
33	24.4	14.80	400
34	23.9	14.80	400
35	23.4	14.80	400
36	22.9	14.8	400
37	22.4	14.8	400
38	21.9	14.7	398
39	21.4	14.6	395
40	20.9	14.4	391
41	20.4	14.2	386

42	19.9	13.75	375
43	19.4	13.69	374
44	18.9	13.52	369
45	18.4	13.3	364
46	17.9	13.2	357

Table : A.3
Variac Setting 110V

S.No.	Distance of t.c. tip from top of fce tube (cm)	EMF (mv)	Temperature (with R.T. correction °C)
1	40.5	15.65	420
2	39.8	15.8	424
3	38.8	16.05	430
4	38.3	16.20	434
5	37.8	16.20	434
6	37.3	16.3	436
7	36.8	16.35	436
8	36.3	16.35	436
9	35.8	16.5	442
10	35.3	16.6	444
11	34.8	16.65	444
12	34.3	16.7	446
13	33.8	16.7	446
14	33.3	16.75	446
15	32.8	16.75	446
16	32.8	16.75	446
17	31.8	16.85	448
18	31.3	16.90	450
19	30.8	16.90	450
20	30.3	16.97	452
21	29.8	16.97	452
22	29.4	17.0	452
23	28.8	17.0	452
24	28.3	17.0	452
25	27.8	17.0	452
26	27.3	17.05	454
27	27.1	17.05	454
28	26.9	17.05	454
29	26.4	17.1	454
30	25.9	17.1	454
31	25.4	17.1	454
32	24.9	17.15	456
33	24.4	17.1	454
34	23.9	17.1	454
35	23.4	17.1	454
36	22.9	17.0	452
37	22.4	16.9	450
38	21.9	16.8	448
39	21.4	16.5	442
40	20.9	16.4	438
41	20.4	16.1	430

42	19.9	15.9	426
43	19.4	15.7	422
44	18.9	15.5	416
45	18.4	15.25	410
46	17.9	14.9	384

**Temperature Profile Measurement Inside and Outside the Crucible for 2 wt%
and 4 wt% Bi alloys.**

Table A.4
Temperature distribution inside the crucible for 2 wt% Bi alloy

S.No.	Dist. of t.c. sheath tip from fce top	Dist. of t.c. jn from interface	Millivolt output of t.c. (in mv)	Fce temperature in °C after R.T. correction
1	26.57	0.2	8.7	245
2	25.67	0.7	9.9	274
3	25.21	1.16	10.85	297
4	24.81	1.56	11.61	316
5	23.91	2.46	12.95	348
6	23.65	2.72	13.25	354
7	23.17	3.2	13.82	368
8	22.73	3.64	14.3	380
9	22.3	4.07	14.68	389
10	21.88	4.49	15.05	397
11	21.58	4.79	15.3	404
12	21.13	5.24	15.58	410
13	20.35	6.02	16.00	420
14	19.6	6.77	16.38	429
15	18.77	7.60	16.7	437
16	17.91	8.46	16.95	443
17	17.08	9.29	17.15	447
18	16.16	10.21	17.33	452
19	15.41	10.96	17.45	454
20	14.48	11.89	17.55	457
21	12.63	13.74	17.63	459
22	11.79	14.58	17.68	460
23	10.83	15.54	17.60	458
24	9.93	16.44	17.4	453
25	9.11	17.26	17.22	448
26	8.06	18.31	16.95	442
27	7.16	19.21	16.45	431
28	6.23	20.14	16.0	420
29	4.83	21.54	14.86	393
30	4.31	22.06	14.08	374
31	3.63	22.74	13.05	350
32	2.90	23.47	12.05	326

Table A.5
Temperature distribution outside the crucible for 2 wt% Bi alloy

S.No.	Dist. of t.c. sheath tip from fce top	Millivolt output of t.c.	Temp in °C after R.T. correction
1	26.79	12.13	328
2	26.52	12.54	338
3	26.93	13.14	352
4	25.57	13.63	364
5	25.04	14.2	377
6	24.58	14.6	387
7	24.08	14.75	391
8	23.57	15.23	402
9	23.09	15.52	409
10	22.58	15.75	414
11	22.09	15.95	419
12	21.58	16.17	424
13	20.56	16.56	433
14	19.52	16.85	440
15	18.58	17.13	447
16	17.51	17.4	454
17	16.48	17.62	458
18	15.51	17.69	460
19	14.45	17.85	464
20	13.81	18.0	467
21	12.71	17.52	456
22	11.66	17.45	455
23	10.56	17.25	450
24	9.63	17.22	449
25	8.64	17.0	444
26	7.11	16.48	431
27	6.12	15.9	418
28	5.14	15.22	402
29	4.14	14.2	377
30	3.66	13.55	362
31	1.93	11.00	301
32	0.99	8.25	234

Table A.6
Temperature distribution inside the crucible for 4 wt% Bi alloy

S.No.	Dist. of t.c. sheath tip from fce top	Dist. of t.c. jn from interface	Millivolt output of t.c.	Temp in °C after R.T. correction
1	26.16	0.2	8.67	242.5
2	25.86	0.5	9.25	257.0
3	25.65	0.71	9.77	270
4	25.26	1.1	10.46	287
5	24.79	1.57	11.15	303.5
6	24.47	1.89	11.55	313
7	24.17	2.19	12.05	325
8	23.9	2.46	12.3	331
9	23.55	2.81	12.7	341
10	23.16	3.2	13.1	350.5
11	22.84	3.52	13.45	359
12	22.0	4.36	14.14	376
13	21.4	4.96	14.56	386
14	20.72	5.64	14.98	395.3
15	20.1	6.26	15.29	403
16	19.77	6.59	15.46	401
17	18.92	7.44	15.78	414.5
18	18.05	8.31	16.04	421.0
19	17.05	9.31	16.27	426
20	16.09	10.27	16.43	430.0
21	14.94	11.42	17.35	450
22	14.63	11.73	17.43	452
23	14.08	12.04	17.57	456
24	13.72	12.4	17.55	455
25	13.34	12.79	17.55	455
26	13.0	13.12	17.55	455
27	12.24	13.88	17.47	453
28	11.57	14.55	17.33	450
29	11.09	15.03	17.2	446
30	10.4	15.72	16.8	437
31	9.75	16.37	16.65	433
32	9.23	16.89	16.35	426
33	8.71	17.41	16.07	420
34	7.55	18.57	14.4	380
35	4.31	21.81	12.45	334

Table A.7
Temperature distribution outside the crucible for 4 wt% Bi alloy

S.No.	Dist. of t.c. sheath tip from fce top	Millivolt output of t.c.	Temp in °C after R.T. correction
1	3.67	13.15	350.5
2	4.68	14.36	379
3	5.69	15.28	400
4	6.72	15.9	416
5	7.64	16.22	423.5
6	8.68	16.60	432.5
7	9.6	16.98	441.5
8	10.17	17.22	447.0
9	10.7	17.35	450
10	11.2	17.38	451
11	11.7	27.68	452
12	12.2	17.52	454.5
13	12.7	17.53	455
14	13.2	17.55	455
15	13.35	16.9	439.5
16	14.01	17.2	447.0
17	14.92	17.15	445.5
18	15.83	17.02	442.5
19	16.77	16.9	439.5
20	17.75	16.79	437
21	18.7	16.55	431.0
22	19.69	16.31	425.5
23	20.37	16.13	421
24	20.98	15.88	415
25	21.68	15.77	413
26	22.45	15.48	406
27	22.93	15.25	400.5
28	24.19	14.72	388
29	24.64	14.7	387.5
30	25.31	14.4	380
31	25.63	13.9	368
32	26.01	13.6	361
33	26.45	12.8	342

**Temperature measurements at different points below the equilibrium
solid/liquid interface for 4wt% Bi alloy**

Table A.8
Temperature distribution inside the solid

S.No.	Cathetometer reading of top end of t.c.	Dist. of t.c. jn from solid/liquid interface	Millivolt output	Temp in °C after R.T. correction
1	30.98	-0.2	7.51	213.5
2	30.78	-0.4	7.39	210.5
3	30.52	-0.66	6.95	199.5
4	30.32	-0.86	6.83	196.5
5	30.29	-1.17	6.40	186
6	30.01	-0.89	6.31	183.5
7	29.61	-1.57	5.85	172
8	28.97	-2.21	4.84	147
9	28.33	-2.85	3.57	116.5

Table A.9
Cooling Curve 1

Thermocouple tip positioned such that the top of t.c. is 28.33 cms in cathetometer

S.No.	Time (in sec)	Millivolt output	Temperature (°C) after R.T. correction
1	0	8.40	236
2	70	5.0	151
3	100	4.57	140.5
4	140	4.2	131.5
5	155	4.13	130
6	170	4.04	128
7	200	3.95	126
8	215	3.9	124.5
9	240	3.83	123
10	255	3.80	122
11	275	3.78	121.5
12	300	3.75	121
13	330	3.71	120
14	360	3.68	119
15	390	3.64	118
16	425	3.62	117.5
17	480	3.6	117.0
18	540	3.58	116.5
19	600	3.57	116.5

Table A.10
Cooling Curve 2

Thermocouple tip positioned such that the top of t.c. is 30.29 cms in cathetometer

S.No.	Time (in sec)	Millivolt output	Temperature (°C) after R.T. correction
1	0	11.55	313
2	30	10.38	285
3	82	8.5	238
4	107	7.88	223
5	150	7.33	209
6	180	7.10	203
7	210	6.92	199
8	248	6.80	196
9	310	6.62	191
10	360	6.55	189.5
11	390	6.48	187.5
12	450	6.44	187.0
13	510	6.39	185.5
14	570	6.36	185.0
15	630	6.33	184.0
16	690	6.31	183.5

Appendix B

Determination of Position of solid/liquid interface for 2 wt% and 4 wt% alloy using cathetometer measurements of thermocouple.

The following the position of solid/liquid interface with respect to the chill cap, chill and the bottom of the crucible containing the ingot.

Fixed distances for a run:

- B = height of the cork arrangement above the furnace top
= 8.4 cm
- C = total furnace length = 38.9 cm
- E = total length of the chill assembly tube
= 30.25 cm
- M = total length of the chill assembly tube with chill cap on
= 30.92 cm
- F = total length of the crucible stand
= 42.47 cm
- I = height of the cooling ring
= 1.62 cm
- J = depth of the blindhole at the top of the crucible stand
= 1.4 cm
- K = distance from lower surface of annular ring to furnace bottom
= 13.8 cm

After thermocouple is inserted such that it exactly touches the solid-liquid interface the following variable distances are measured after equilibrium is attained in the system.

For Sn-2 wt% Bi alloy

- D = total length of the glass thermocouple sheath
= 39.3 cm
- G = the length of the cooling assembly tube that is projecting below the lower surface of the annular ring
= 5.2 cm

H = the initial length of the crucible stand from the lower surface of annular ring to the base of the stand
= 19.3 cm

A = length of the thermocouple sheath that is visible above the cork arrangement
= 4.73 cm

X = thickness of crucible at the bottom
= 0.2 cm

Let the solid-liquid interface be at any position after equilibrium is attained.

Exact height of the solid/liquid interface w.r.t. the bottom of the crucible

$$\delta_i = \{(C-(D-(A+B))) - (F-(K+H+J))\}$$

$$= (38.9 - 26.17) - 7.97$$

$$= 4.76 \text{ cm}$$

Exact height of the solid/liquid interface w.r.t. the bottom of the ingot ' δ ' = $\delta_i - x = 4.76 - 0.2 = 4.56 \text{ cm}$.

For Sn-4 wt% Bi alloy:

D = total length of the glass thermocouple sheath
= 38.9 cm

G = the length of the cooling assembly tube that is projecting below the lower surface of the annular ring
= 5.12 cm

H = the initial length of the crucible stand from the lower surface of annular ring to the base of the stand
= 19.3 cm

A = length of the thermocouple sheath that is visible above the cork arrangement
= 4.34 cm

Total length of the thermocouple sheath above the furnace top = A + B
= 4.73 + 8.4
= 13.13 cm

Length of the thermocouple from the top end of the furnace

$$= D - (A+B)$$
$$= 39.3 - (13.13)$$

$$= 26.17 \text{ cm}$$

Position of the top end of the chill ring from the bottom end of furnace

$$= E - (K+G) = 30.25 - (13.8+5.2) \\ = 11.25 \text{ cm}$$

Position of chill ring from top end of furnace tube

$$= (C - CE - (K+G)) \\ = 38.9 - 11.25 = 27.65 \text{ cm.}$$

δ_c - interface position w.r.t. chill ring is

$$\delta_c = (C - (E - (K+G))) - (D - (A+B)) \\ = 27.65 - 26.17 \\ = 1.48 \text{ cm.}$$

δ_f - interface position w.r.t. top of the fee tube

$$= D(A+B) = 26.17 \text{ cm.}$$

Let the solid/liquid interface be at any position after equilibrium is attained.

Total length of the thermocouple sheath above the fee top = $A + B = 4.34 + 8.4 = 12.74$ cm

Length of the thermocouple from the top end of the furnace

$$= D - (A+B) \\ = 38.9 - 12.74 \\ = 26.16 \text{ cm}$$

Position of top end of chill ring from the bottom end of furnace

$$= E - (K+G) \\ = 30.25 - (5.12 + 13.8) = 11.33 \text{ cm.}$$

Position of top end of chill ring from top end of furnace tube

$$= C - [E - (K+G)] = 38.9 - 11.33 = 27.57 \text{ cm.}$$

New $\delta_i = (C - (E - (K+G))) - (D - (A+B))$

$$= 27.57 - 26.16 = 1.41 \text{ cm}$$

δ_i = interface position w.r.t. top of the furnace tube

$$\begin{aligned} &= (D - (A + B)) \\ &= 26.16 \text{ cm} \end{aligned}$$

Exact height of the solid-liquid interface position w.r.t. the bottom of the crucible

$$\begin{aligned} \delta_i &= [(C - (D - (A + B))) - [F - (K + H + J)]] \\ &= (38.9 - 26.16) - (42.47 - (13.80 + 1.4 + 19.3)) \\ &= 12.74 - 7.97 = 4.77 \text{ cm.} \end{aligned}$$

Exact height of the solid-liquid interface position w.r.t. the bottom of the ingot

$$\delta = \delta_i - x = 4.77 - 0.2 = 4.57 \text{ cm.}$$

Appendix C

Procedure to determine true lamellar dendrite spacing

Figure C.1 shows two mutually perpendicular sections of a directionally solidified specimen with the direction of heat extraction along the z axis. PM and PL are the traces of a plate like dendrite in the sectioning surfaces A and B. PC denotes a direction in the surface A and normal to PM along which the apparent P.D.S. λ is measured.

If λ_o = is the true spacing then

$$\lambda_o = \lambda K$$

$$\text{where } K = \frac{\sin \theta_b}{(1 - \cos^2 \theta_a \cos^2 \theta_b)^{1/2}}$$

θ_b = angle which the platelike dendrites make with the longitudinal edge.

θ_a = angle which the platelike dendrites make with the transverse edge.

This formula proposed by V. Bansal [24] is applicable to the PDS measurements on transverse section. The present work involves measurements on longitudinal sections. Considering the geometry of the figure the reverse is true for determining K factor in case of longitudinal sections. Now θ_b instead of the angle made by the dendrites with the edge of longitudinal section becomes the angle made by the platelike dendrites with the edge of the transverse section. This is true for θ_a also.

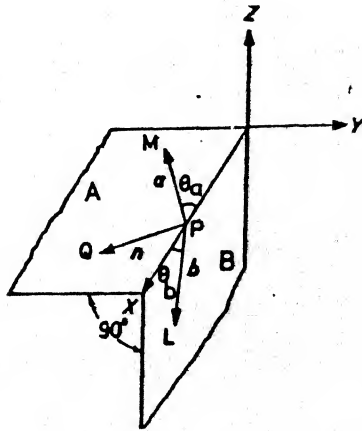


Figure C.1: The transverse (A) and longitudinal (B) sections in a right-handed Cartesian co-ordinate system.

Table C.1
Angle Measurement Data

Nominal Bi. Composition	Sample identification	Angle made by dendrites with longitudinal edge θ_l in degrees	Angle made by dendrites with transverse edge θ_t in degrees	$K = \frac{\sin \theta_b}{(1 - \cos^2 \theta_a \cos^2 \theta_b)}$
2	a2	93	77	0.9986
2	a3	91.16	69.5	0.9996
2	a4	92.0	77.33	0.9998
2	a5	91.5	167.5	0.999
4	b1	90.6	119	0.9999
4	b2	85.33	122	0.9976
4	b3	88.5	168.5	0.9998
4	b4	87.33	41	0.9993
4	b5	90.5	39.5	0.999

Appendix D

Table D.1
PDS measurement data on 2 wt% Bi alloy

Compositi on wt% Bi	Sample Identification	Freezing rate in $\mu\text{m/s}$	Distance from Starting interface (mm)	Micrometric reading -----			Dendrite count n	App. PDS in μm $\times(1.083)/n$	K	Real PDS in μm
				Initial	final	Diff.				
2	a1	34.87	1	160	786	626	5	135.6	0.9999	136.29
	a1	34.87	3	138	1032	894	7	138.3		138.3
	a1	34.87	5	26	875	849	7	131.35		131.35
	a1	34.87	7	120	712	592	5	128.23		128.23
	a1	34.87	9	38.3	842	804	7	124.4		129.4
	a1	34.87	11	25	825	800	7	123		123
	a1	34.87	13	105	793	688	7	106.45		106.45
2	a2	34.87	16.6	49.5	966	916.5	9	109.3		109.3
	a2	34.87	18.4	30	780.25	750.25	8	101.56	0.9986	101.56
	a2	34.87	20.4	50	967	917	9	110.34		110.34
	a2	34.87	22.4	45	736	691	7	109.0		107.
	a2	34.87	24.4	50	911	861	8	116.5		116.5
	a2	34.87	26.4	20	660	640	6	115.52		115.5
	a2	34.87	28.5	40	845	805	8	108.98		108.98
	a2	34.87	28.7	80	800	720	8	97.5		97.5
	a2	34.87	30.7	70	668	598	7	92.45		92.5

Compositi on wt% Bi	Sample Identification	Freezing rate in $\mu\text{m/s}$	Distance from Starting interface (mm)	Micrometric reading -----			Dendrite count n	App. PDS in μm $\times(1.083)/n$	K	Real PDS in μm
				Initial	final	Diff.				
2	a2	284	32.7	47	710	663	7	102.57		102.57
	a2	284	34.7	53	748	695	11	69.5		68.5
	a2	284	36.7	0	682	682	8	98.33		92.31
	a2	284	38.7	50	651	601	6	108.5		108.5
	a2	284	40.7	112	582	470	5	101.8		101.8
	a2		41.9	0	718	718	8	97.19		97.19
2	a3	284	47.0	98	600	502	6	90.61	0.9999	0.61
	a3	284	49	137	702	565	6	101.9		101.9
	a3	284	51.05	97	686	589	6	106.5		106.5
	a3	284	53.0	41	706	665	6	110.83		110.83
	a3	284	55	5	606	601	6	108.5		108.5
	a3	45.9	57	124	777	653	6	117.867		117.867
	a3	45.9	59	53	776	723	6	130.5		130.5
	a3	45.9	61	52	703	751	5	141.007		1410.07
	a3	45.9	63	50	668	618	5	133.8		133.8
	a3	45.9	65	100	790	690	5	149.4		149.4
	a3	45.9	67	179	865	686	5	148.5		148.5
	a3	45.9	69	184	720	536	4	145		145
	a4	45.9	74.08	22.5	795	772.5	7	119.5		119.5
	a4	45.9	76.08	17	583	566	10	61.3		61.3

Compositi on wt% Bi	Sample Identification	Freezing rate in $\mu\text{m/s}$	Distance from Starting interface (mm)	Micrometric reading ----- Initial final Diff.			Dendrite count	App. PDS in μm $\times(1.083)/n$	K	Real PDS in μm
		45.9	78.08	-20	597	577	10	62.5		62.5
		45.9	80.08	0	690	690	10	74.72		74.72
		45.9	82.08	62	851	789	10	85		85
		45.9	84.08	77	844	767	10	83		83
		45.9	86.08	70	803	733	10	79.4		79.4
		154	88.08	38	818.5	780.5	10	84.5		84.5
		154	90.08	97	741	644	8	87.2		87.2
		154	92.08	0	702	702	9	84		84
		154	94.08	37	817	780	10	84.47		84.47
		154	96.08	18.5	685.5	667	9	90.26		80.26
		154	97.08	60	515	455	6	82.13		82.13
		154	98.08	11	735	724	10	78.4		78.4
2	a5	154	102.68	65	676	611	7	94.5	0.999	94.5
		154	104.68	70	803	733	10	79.4		79.4
		154	106.68	35	646	611	8	82.74		82.74
		154	107.68	61	460	399	5	86.4		86.4
		154	108.58	143	629	486	6	87.0		87.0
		154	109.68	60	525	465	5	100.7		100.7
		154	111.68	35	493	458	5	101.4		101.4
2		154	113.68	225	515	290	3	104.6		104.6

		261.4	43.6	235	930	695	9	83.6	83.6
		261.4	45.6	50	842	792	10	86	86
		261.4	47.6	130	810	680	8	92.05	92.05
		261.4	48.6	35	870	835	9	100	100
		261.4	49.6	95	845	750	10	81	81
		261.4	51.6	41.6	838	796.4	9	95.8	95.8
		261.4	53.6	60	538	478	6	86.4	86.4
		114.98	55.6	95	403	308	4	83.4	83.4
4		114.98	57.85	257	714	457	5	99	99
		114.98	58.7	52.5	566	513.5	5	111.2	111.2
		114.98	63.3	105	403	298	4	80	80
		114.98	65.3	61	400	339	4	92	92
		114.98	67.3	161	475	314	4	85.02	85.02
		114.98	69.3	35	417	382	4	103	103
		114.98	71.3	10	496	486	5	105	105
		114.98	73.3	179	179	537	4	97	97
		114.98	75.3	75	583.6	508.6	5	110.16	110.16
		114.98	77.3	136.3	587.6	451.3	5	97.75	97.75
4	b4	114.98	79.3	139	585	446	5	96.6	96.6
	b4	114.98	81.3	65	455	390	4	105.59	105.59
	b4	114.98	83.3	125.67	531	405.3	4	109.74	109.74
	b5	64.61	88.3	254	728	474	4	128.3	128.3
		64.61	90.3	363	813	450	4	121.84	121.8
		64.61	92.3	410	874	464	4	125.6	125.6
		64.61	94.3	189	696	507	4	137.2	137.2
		64.61	96.3	245	729	484	4	134	134.8

Appendix E
Measurement on Electron Probe Micro Analyzer

Table: E.1
Bi concentration data taken along the length of a dendrite for
sample a3 (2 wt% Bi alloy)

S.No.	X	Y	Wt% Bi
1	17.952	60.548	2.249
2	17.850	60.548	2.467
3	17.75	60.548	1.127
4	17.65	60.548	2.898
5	17.55	60.548	4.343
6	17.47	60.554	1.517
7	17.404	60.550	0.000
8	17.304	60.550	3.238
9	17.204	60.526	1.404
10	17.104	60.526	1.063
11	18.05	60.544	4.403
12	18.15	60.544	12.592
13	18.25	60.551	1.872
14	18.394	60.451	0
15	18.481	60.558	3.614
16	18.581	60.558	5.805
17	18.681	60.558	3.632
18	18.637	60.582	1.738
19	18.863	60.572	3.532
20	18.963	60.572	1.931

Table: E.2
Bi concentration data taken along the length of an interdendrite for
sample a2 (2 wt% Bi alloy)

S.No.	X	Y	Wt% Bi
1	53.532	58.778	6.797
2	53.632	58.769	7.032
3	53.762	58.752	8.065
4	53.862	58.741	9.211
5	53.962	58.737	8.866
6	54.062	58.719	10.181
7	54.162	58.713	9.089
8	54.278	58.698	7.764
9	54.344	58.69	16.633
10	54.444	58.691	9.211
11	53.432	58.763	7.492
12	53.332	58.790	7.979
13	53.232	58.804	4.827
14	53.132	58.807	4.887
15	53.032	58.823	6.120
16	52.932	58.830	8.557
17	52.832	58.843	8.142
18	52.732	58.839	6.281
19	52.632	58.85	7.29
20	52.505	58.861	6.586

Table: E.3
Bi concentration data taken across two dendrites for
sample a2 (2 wt% Bi alloy)

S.No.	X	Y	Wt% Bi
1	52.499	59.914	1.211
2	52.499	59.924	3.668
3	52.499	59.934	3.524
4	52.499	59.944	4.212
5	52.499	59.954	5.878
6	52.499	59.964	6.859
7	52.499	59.974	7.321
8	52.499	59.954	7.867
9	52.499	59.994	3.328
10	52.499	60.004	0.028
11	52.499	60.014	3.026
12	52.475	60.024	2.849
13	52.475	60.034	2.028
14	52.475	60.044	5.166
15	52.475	60.054	3.906
16	52.475	60.070	4.659
17	52.475	60.085	11.098
18	52.475	60.100	7.803
19	52.475	60.515	4.597

Table: E.4
Bi Concentration Data taken across two dendrites for
sample b2 (4 wt% Bi alloy)

S.No.	X	Y	Wt% Bi
1	66.262	71.370	8.461
2	66.262	71.385	5.760
3	66.262	71.400	7.273
4	66.262	71.415	5.588
5	66.262	71.430	5.559
6	66.262	71.445	3.748
7	66.262	71.460	4.931
8	66.262	71.475	5.761
9	66.262	71.490	8.165
10	66.262	71.505	9.146
11	66.262	71.520	6.808
12	66.262	71.535	4.807
13	66.262	71.550	2.197
14	66.262	71.565	4.780
15	66.262	71.580	9.010
16	66.262	71.595	5.908

Table: E.5
Bi concentration data taken near the interdendritic region for
sample a4 (2 wt% Bi alloy)

S.No.	X	Y	Wt% Bi
1	73.356	59.038	4.817
2	73.406	59.038	1.329
3	73.456	59.038	3.874
4	73.506	59.038	4.267
5	73.556	59.038	6.157
6	73.606	59.038	4.249
7	73.656	59.038	0.367
8	73.710	59.038	3.058
9	73.760	59.044	3.033
10	73.287	59.038	3.218
11	73.237	59.038	3.656
12	73.187	59.038	2.037
13	73.137	59.044	4.122
14	73.087	59.044	3.574
15	73.037	59.044	4.143
16	72.987	59.044	4.589
17	72.937	59.047	4.996
18	72.887	59.038	0.501
19	72.837	59.038	1.699
20	72.787	59.038	3.945
21	72.737	59.038	6.367
22	72.687	59.038	7.743
23	72.637	59.038	5.520
24	72.587	59.035	7.051
25	72.537	59.035	1.150
26	72.487	59.032	4.449
27	72.437	59.032	3.749
28	72.387	59.029	4.907
29	72.324	58.023	5.438
30	72.274	59.028	0.809
31	72.224	59.010	2.380
32	72.174	59.010	4.525
33	72.124	59.998	2.144
34	72.074	59.004	5.595

Appendix F

Theoretical Expression for Solute Redistribution for Dendritic Solidification.

The equation given by Sarreal et.al. [20] for solute redistribution is

$$C_s^* = KC_t \left\{ \frac{a}{K-1} + \left(1 - \frac{aK}{K-1} \right) \left(\frac{1-f_s}{1-f_{s0}} \right)^{K-1} \right\} \quad (F.1)$$

where C_s^* = concentration of solute in the solid,

f_s = solid weight fraction,

f_s = 0 at the centre of the dendrite,

f_s = 1 at the centre of the interdendritic region,

K = equilibrium partition ratio,

C_t = composition of the liquid ahead of the dendrite tip,

f_{s0} = fraction solid with a constant concentration of KC_t ,

$$a = \frac{-D_L G}{m_L \cdot R \cdot C_o} \quad (2.8)$$

where D_L = diffusion coefficient of solute in the liquid,

G = temperature gradient in the liquid,

R = growth rate,

C_o = initial average composition,

m_L = slope of the liquidus,

C_t = composition of the liquid ahead of the dendrite tip given as

$C_t = (1-a) C_o$.

Calculations for Sn-2 wt% Bi alloy:

$K = 0.37$, $m_L = 1.33 \text{ } ^\circ\text{C/wt\%}$

$G = 8.4 \text{ } ^\circ\text{C/mm}$, $R = 34.87 \text{ } \mu\text{m/s}$,

$$D_L = 3.5 \times 10^{-3} \text{ mm/s}, C_o = 2 \text{ wt\% Bi}$$

$$a = \frac{-D_L G}{m_L \cdot R \cdot C_o} = \frac{-3.5 \times 10^{-3} \times 8.4}{1.33 \times 34.87 \times 10^{-3} \times 2} = -0.316$$

$$a = -0.316$$

$$C_i = (1-a) C_o = (1.316)2 = 2.634 \text{ wt\%}$$

$$C_i = 2.634 \text{ wt\%}$$

C_o , composition of the liquid ahead of the dendrite tip is 2.634 wt%.

$$f_s^o = \frac{C_o - C_i}{C_i(K-1)} = \frac{2 - 2.634}{2.634(0.37 - 1)} = 0.382$$

Substituting the values in equation F.1,

$$a = \frac{-D_L G}{m_L \cdot R \cdot C_o}$$

$$= \frac{-3.5 \times 10^{-3} \times 7.8}{1.24 \times 31.05 \times 10^{-3} \times 4}$$

$$a = -0.177$$

$$C_i = C_o (1-a) = 1.177 \times 4 = 4.709 \text{ wt\%}$$

C_o composition of the liquid ahead of the dendrite tip is 4.709 wt%.

$$f_s^* = \frac{C_o - C_i}{C_i(K-1)}$$

$$= \frac{4 - 4.709}{4.709(0.37 - 1)}$$

$$= f_s^o = 0.239$$

Substituting the values in equation F.1, C_s^* is obtained as a function f_s - fraction of solid. ' f_s ' is taken from the center of the dendrite to the center of interdendritic region.

$$C_s^* = 1.742 \left\{ 0.281 + 0.896 \left(\frac{1-f_s}{0.761} \right)^{-0.63} \right\}$$

$$C_s^* = 0.975 \left\{ 0.501 + 0.8144 \left(\frac{1-f_s}{0.618} \right)^{-0.63} \right\}$$

' f_s ' is taken from the center of the dendrite to the centre of interdendritic region.

$f_s = 0$ at the centre of the dendrite.

The C_s^* calculated from the equation is concentration of Bi across the dendrites for 2wt% Bi.

Table F.1
Concentration of Bi across the dendrite for
sample a2 (2 wt% Bi alloy)

Sr.no	C_s^*	f_s
1	1.2825	0
2	1.2825	0.382
3	1.3959	0.5
4	1.533	0.6
5	1.7404	0.7
6	2.104	0.8
7	2.989	0.9
8	4.36	0.95
9	4.944	0.96
10	5.83	0.97
11	7.383	0.98
12	11.16	0.99

The Bi concentration obtained is plotted with f_s .

Calculations of Sn-4 wt% Bi alloys:

$$K = 0.37 \quad m_L = 1.24 \text{ } ^\circ\text{C/wt}\%$$

$$G = 7.8 \text{ } ^\circ\text{C/mm} \quad R = 31.05 \text{ } \mu\text{m/s}$$

$$G = 7.8 \text{ } ^\circ\text{C/mm} \quad R = 1.05 \text{ } \mu\text{m/s}$$

$$D_L = 3.5 \times 10^{-3} \text{ mm/s} \quad C_o = 4 \text{ wt}\%$$

Table F.2
Concentration of Bi across the dendrite for
sample b2 (4 wt% Bi alloy)

S.No.	C_s^*	f_s
1	2.05	0
2	2.05	0.239
3	2.135	0.30
4	2.302	0.40
5	2.523	0.50
6	2.83	0.60
7	3.295	0.70
8	4.111	0.80
9	6.095	0.90
10	9.16	0.96

Appendix G

Determination of excess solute in the enriched layer when the freezing rate increased from R to R_1 .

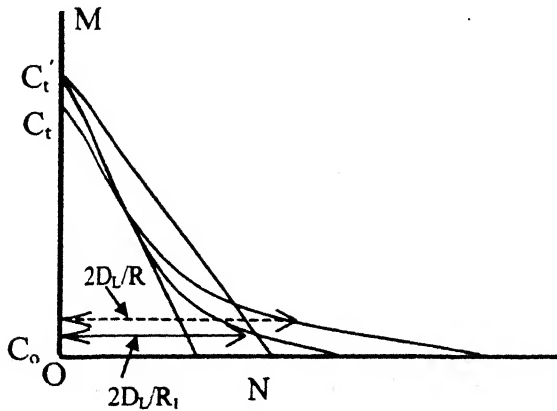


Figure G.1

C_t = composition of the liquid ahead of the dendrite tip

$$= C_o(1-a), \text{ where } a = (-D_L G / M_L R C_o)$$

C_o = initial average composition = 2wt%

D_L = diffusion coefficient of solute in the liquid = 3.5×10^{-3} mm/s

M_L = slope of the liquidus = $1.33^\circ\text{C}/\text{wt}\%$

R = freezing rate in $\mu\text{m}/\text{s}$.

G = temperature gradient in the melt ahead of the S/L interface = $7.4^\circ\text{C}/\text{mm}$

$$C_t = C_o(1-a)$$

The freezing rate ' R ' = $45.9 \mu\text{m}/\text{s}$

$$C_t = C_o(1-a)$$

$$C_o = 2 \text{ wt}\% ; a = \frac{-D_L G}{M_L R C_o} = \frac{-3.5 \times 10^{-3} \times 8.4}{1.33 \times 45.9 \times 2} = -0.239$$

$$a = -0.239$$

$$C_t = C_o(1-a)$$

$$= 1.239 \times 2 = 2.478 \text{ wt}\%$$

Excess amount of solute in the boundary layer is given by area of the triangle for 'R' as seen from the Figure G.1 $= 1/2 \cdot C_i \cdot 2D_L/R = 0.188 \text{ wt\%mm}$

Now, if the freezing rate has been increased from 'R' to 'R₁', i.e. from 45.9 to 154 $\mu\text{m/s}$.

$$R_1 = 154 \mu\text{m/s}$$

$$a = \frac{-D_L G}{m_L \cdot R \cdot C_o} = \frac{-3.5 \times 10^3 \times 8.4}{1.33 \times 154 \times 10^{-3} \times 2} = -0.0717$$

$$C'_i = (1-a) C_o$$

$$= (1.0717)2 = 2.143 \text{ wt\%}$$

Thus 'C_i' is decreased when there is an abrupt increase in freezing rate.

Excess amount of solute in the boundary layer is given by area of the triangle for new R₁ as seen from the Figure G.1

$$= 1/2 \cdot C'_i \cdot (2 D_L/R_1) = C'_i \cdot (D_L/R_1)$$

$$= 2.143 \frac{(3.5 \times 10^{-3})}{(154 \times 10^{-3})} = 0.048 \text{ wt\% mm}$$

Excess amount of solute in the boundary layer when the freezing rate is increased is 0.048 wt%.mm.

Appendix H

Determination of Heat Transfer Coefficient

The heat transfer coefficient was calculated with the experimental results.

The overall heat transfer coefficient is given by

$$U = \text{overall heat transfer coefficient}$$
$$= \frac{Q}{2\pi r(h_1\Delta T_1 + h_2\Delta T_2 + h_3\Delta T_4 + h_5\Delta T_5)}$$

where Q = Rate of heat removal by water

h_1, h_2, h_3, h_4, h_5 are the points below the equilibrium solid/liquid interface. The total length taken over which the heat transfer is taking place is

$$h_1 + h_2 + h_3 + h_4 + h_5 = 1.96 \text{ cm}$$

$\Delta T_1, \Delta T_2, \Delta T_3, \Delta T_4$ and ΔT_5 are the difference between the average temperature in the solid at that point and the outlet water temperature.

Q = Rate of heat removal by water

$$= m C_p \Delta T$$

where m = mass flow rate of water

C_p = specific heat of water

ΔT = difference between outlet and inlet water temperatures.

Inlet water temperature = 27.5 °C

Outlet water temperature = 33°C

q = chill water flow rate

$$= 280 \text{ cc/min}$$

ρ_1 = density of water.

$$C_p = 1.007 \text{ kcal/kg}^\circ\text{C}$$

$$m = q \cdot \rho_1 = 280 \text{ g/min}$$

Q = Rate of heat removal by water

$$= m C_p \Delta T = 280 \times 1 \times 1.007 \times (33-27.5)$$

$$= 25.83 \text{ cal/s}$$

Figure H.1 shows the temperature at different points below the solid/liquid interface. The total length over which heat transfer is taking place is shown in the Figure H.1. figure H.1 shows the position of chill ring and the crucible stand. The difference between these two positions is the total length taken for the heat transfer take place.

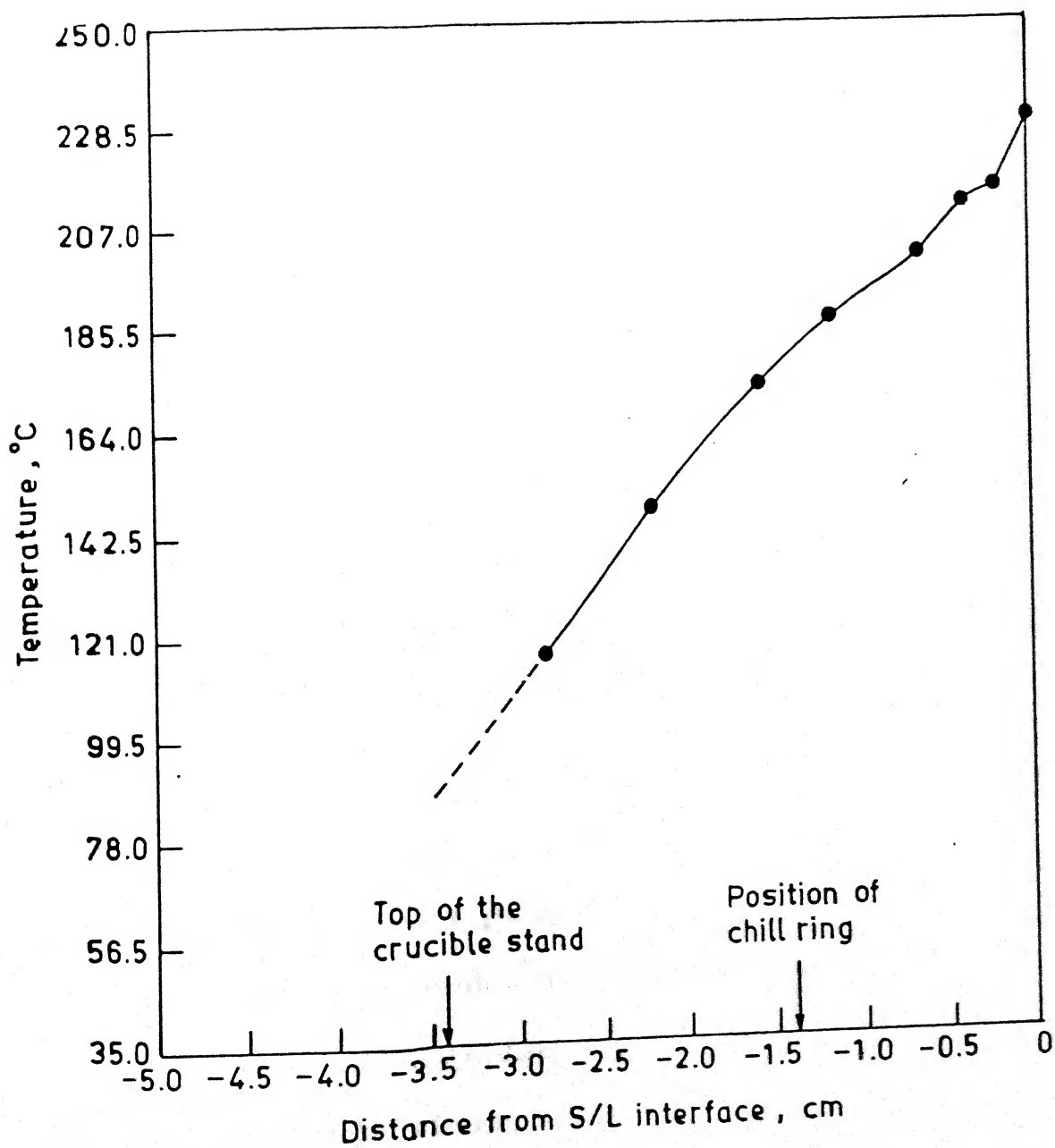


Figure H.1: Temperature at different points below the equilibrium solid/liquid interface.

$$U = \frac{Q}{2\pi r (\Delta h_1 \cdot \Delta T_1 + h_2 \cdot \Delta T_2 + h_3 \Delta T_3 + h_4 \Delta T_4 + h_5 \Delta T_5)}$$

'r' is the radius of the Vycor crucible = 0.64 cm

ΔT_1 = Difference in temperature at 0.49 cm from top end of chill ring and outlet water temperature.

ΔT_2 = Difference in temperature at 1.09 cm from top end of chill ring and outlet water temperature.

ΔT_3 = Difference in temperature at 1.44 cm from top end of chill ring and outlet water temperature.

ΔT_4 = Difference in temperature at 1.84 cm from top end of chill ring and outlet water temperature

ΔT_5 = Difference in temperature at 1.96 cm from top end of chill ring and outlet water temperature.

Substituting the above values,

$$U \text{ (overall heat transfer coefficient)} = 0.0314 \text{ cal/cm}^2\text{/}^\circ\text{C/sec} = 0.1314 \times 10^4 \text{ watts/m}^2\text{/K}$$

Heat transfer coefficient is also calculated from the empirical relation [21]

$$h_i = 0.67 \left[\frac{K^3 \rho^2 g}{\mu_f^2} \left(\frac{C \mu_f^{5/3}}{KL \rho^{2/3} g^{1/3}} \right) \right]^{1/3} \left(\frac{4G'}{\mu_f} \right)^{1/9}$$

where K = thermal conductivity of water,

ρ = density of water,

g = acceleration due to gravity,

L = total length over which the heat transfer is taking place,

μ_f = average film temperature,

C = specific heat of water,

$4G'/\mu_f$ = Reynolds number.

Velocity of chill water falling $V = q/(NXA)$

q = chill water flow rate = 280 cc/min
= 4.67 cc/sec

A = Area of the holes

Total no. of holes = 14

Diameter of holes = 1mm = 0.1 cm

Radius = 0.05 cm

Velocity of chill water falling is

$$V = \frac{1}{N \times A} = \frac{4.67}{14\pi(0.05)^2}$$

$$V = 42.49 \text{ cm/s}$$

$$\text{Reynolds no.} = \frac{VD_e \rho}{\mu}$$

where μ - is viscosity of water at 20°C

$$= 1.006 \times 10^{-6} \text{ m}^2/\text{s}$$

Substituting in the equation,

The heat transfer coefficient, $h_i = 0.012 \text{ cal/cm}^2/\text{s}^\circ\text{C} = 0.05 \times 10^4 \text{ Watts/m}^2/\text{K}$.

127799

127799

date last stamped.

This image shows a blank sheet of white paper with horizontal ruling lines. A single vertical line runs down the center of the page, creating two equal-width columns. The horizontal lines are evenly spaced and extend across the entire width of the paper. There are no markings, text, or illustrations on the page.